Ultrabroadband coherent anti-Stokes Raman scattering for gas temperature and concentration measurements

DISSERTATION

zur Erlangung des akademischen Grades

doctor rerum naturalium (Dr. rer. nat)

vorgelegt dem Rat der Physikalisch-Astronomischen Fakultät

der Friedrich-Schiller-Universität Jena

von M.Sc. Yang Ran

geboren am 19. Februar 1991 in Guizhou, China

1. Gutachter: Prof. Dr. Stefan Nolte, Friedrich-Schiller-Universität Jena
2. Gutachter: Prof. Dr. Michael Schmitt, Friedrich-Schiller-Universität Jena
3. Gutachter: Prof. Dr. Robert P. Lucht, Purdue University, USA

Datum der Disputation: 25. Oktober 2021

Contents

1 Introduction

One of the biggest challenges for our society is the rising demand for energy, while overall gas emissions have to be reduced. Towards sustainability, the underlying energy conversion processes, such as combustion or gasification, must be made as efficient as possible. In this regard, the capability of measuring the local temperature, species concentration and potential intermediate species is crucial for a better understanding and optimization of these processes [Eckbreth1996].

In-situ laser diagnostics has significant advantages for measurements in gasification or combustion. Over the past few decades, a variety of laser-based techniques have been developed, including methods based on scattering processes [Laurendeau1988], absorption processes [Mellqvist1996], and nonlinear optical processes [Yip1992, Brackmann2002]. Among them, spontaneous Raman scattering is a well established method and widely used to measure species concentrations due to the straightforward linear relation of the Raman signal intensity with species number density, and due to the ability of detecting multiple species at the same time. However, spontaneous Raman scattering is strongly limited by low signal strengths. This may be compensated by short excitation wavelengths and high pulse energies, imposing however additional challenges on the design of the optical components.

Coherent anti-Stokes Raman scattering (CARS) overcomes these drawbacks, and has therefore been proven to be a valuable tool for gas-phase temperature and species concentration measurements [Roy2010a]. It emits a laserlike signal, which makes capturing the entire signal much easier. At atmospheric pressure, CARS is in general orders of magnitude stronger than spontaneous Raman scattering [Eckbreth1996]. The recent progress in the development of ultrashort pulse lasers, i.e., picosecond (ps) or femtosecond (fs) lasers, promotes the capability of CARS measurements to a further extend. The high-repetition-rate radiation delivered from ultrashort pulse lasers enables investigations of highly dynamic energy conversion processes. The ultrashort pulse duration allows

neglecting collisional and pressure effects [Lucht2006, Wrzesinski2013], which further extends the feasibility of CARS measurements in harsh environments. For ultrashort pulse lasers with sub-10 fs pulse duration, its intrinsic ultrabroadband feature of the spectrum provides both the pump and Stokes photons from the same beam, which simplifies the CARS setup and makes simultaneous excitation of multiple species possible [Bohlin2014b]. Despite of these advantages, the performance of temperature and concentration determination under harsh environments varies a lot for different setup configurations and the laser properties used. Gas-filled hollow-core fibers are typically used to generate the ultrabroadband fs-pulses at μJ or mJ level [Nisoli1996]. The induced self-phase-modulation (SPM) during the pulse propagation through the fiber leads to complex spectral characteristics and relatively large shot-to-shot spectral fluctuations [Gallmann2006]. Therefore, the actual Raman excitation efficiency is hard to predict. In addition, previous works on ultrabroadband CARS mainly investigated flames at atmospheric pressure [Bohlin2014a, Bohlin2017], whereas its performance under elevated pressures in closed reaction chambers have not been explored yet.

This work focuses on high temperature, high pressure measurements for multiple species, as well as in-situ coal gasification. The experimental work is based on ultrabroadband sub-10 fs laser-based CARS using optical parametric chirped pulse amplification (OPCPA).

Structure of this thesis

After this introduction, the structure of this thesis is outlined as follows:

In Chapter 2, a brief explanation of molecular spectroscopy with regard to the molecular motions is given at first. Afterwards the CARS process is briefly presented. The relation between molecular populations with temperature is introduced and the Raman cross sections of the gaseous species of interest are summarized. Then an overview of current CARS techniques and more specifically fs-laser-based CARS is presented. The potential of ultrabroadband CARS for practical applications is pointed out afterwards, especially with regard to coal gasification. In Chapter 3, CARS theory and the signal strength are explained. The Raman excitation efficiency with regard to the spectrum of the excitation beams is discussed. Based on this, the simulation model for fitting the experimental ultrabroadband CARS spectra to obtain temperature and concentration information is discussed. Moreover, the theory for minor concentration determination from the modulation dips of the

nonresonant background is introduced. Chapter 4 shows the ultrabroadband CARS setup including the characterization of the laser and introduces the gas oven for temperature, pressure and gas flow control. The sample holder as well as the beam arrangement for the coal gasification investigation are also introduced. Chapter 5 investigates the thermometry based on ultrabroadband CARS. Depending on the different molecular spectroscopic properties, the thermometry performance from a single CARS spectrum (e.g. for CO_2, H_2) or the time-resolved CARS signals (e.g. for N_2) is examined and compared. The temperature measurements are also extended to the high-pressure regime (up to 20 bar). In Chapter 6, concentration measurements are studied in different gas mixtures. The detection limit of CO in CO_2/N_2 atmosphere is explored. For gas mixtures including molecules with large Raman shifts, for instance, H_2 and CH_4, the spectral referencing influence for concentration determination is investigated. In addition, high-pressure concentration measurements (up to 10 bar) are studied. Chapter 7 applies the ultrabroadband CARS to study in-situ coal gasification processes. Minor CO determination from the modulation dips of the nonresonant background is investigated and calibrated for our system. Based on this, the detection or concentration determination limit is further explored. The coal gasification processes using coal powder or a single coal particle are successfully monitored from the ultrabroadband CARS. The temperature evolution as well as the evolution of the generated CO during the carbon conversion process are investigated. The final chapter summarizes and concludes the entire work with a brief outlook.

2 Current state of knowledge

This chapter gives a brief introduction to CARS. The details of the CARS theory are discussed in Chapter 3. In the beginning, the fundamentals of molecular spectroscopy are introduced, including the molecular motions and the transition frequencies. Based on this, the CARS basics are discussed. In addition, the molecular populations with regard to temperature measurements and the Raman cross section related to the concentration determination are discussed. Afterwards, a short overview of the existing CARS techniques for gas-phase diagnostics is presented. The advantages and limitations of ns- and ps-laser-based CARS methods are summarized. The current developments for fs-laser-based CARS are discussed. The motivation for our approach of using ultrabroadband CARS is then presented. In addition, an introduction of coal gasification is presented at the end of this chapter.

2.1 Fundamentals of molecular spectroscopy

Molecular spectroscopy, originating from the absorption, emission or scattering of photons in combination with molecular energy change, is useful for studying the molecular properties and sensing of the environments. The total energy of a molecule depends on its electronic, vibrational and rotational states. Therefore, transitions between these energy levels may occur depending on the energy that is absorbed. A generalized energy diagram for a molecule [DeKock1989] is shown in Fig. 2.1. Obviously, the energy separations between the electronic levels are much larger than those between the vibrational levels. In turn, the vibrational level separations are larger than those of the rotational ones. Energies required to drive an electronic transition are typically in the order of several eV (1 eV ≈ 8065 cm^{-1}), thus the wavelength of the corresponding photons lies in the ultraviolet or visible region [Atkins2006]. Vibrational transitions require less energies (~100-4000 cm^{-1}), which correspond to photons in the near-infrared and infrared region. Rotational transitions

are the least energetic (~0.1-10 cm^{-1}) and correspond to the far-infrared and microwave region photons [DeKock1989]. The electronic transitions will not be further discussed since the main transitions of interest for the CARS process are the vibrational and rotational ones in this thesis.

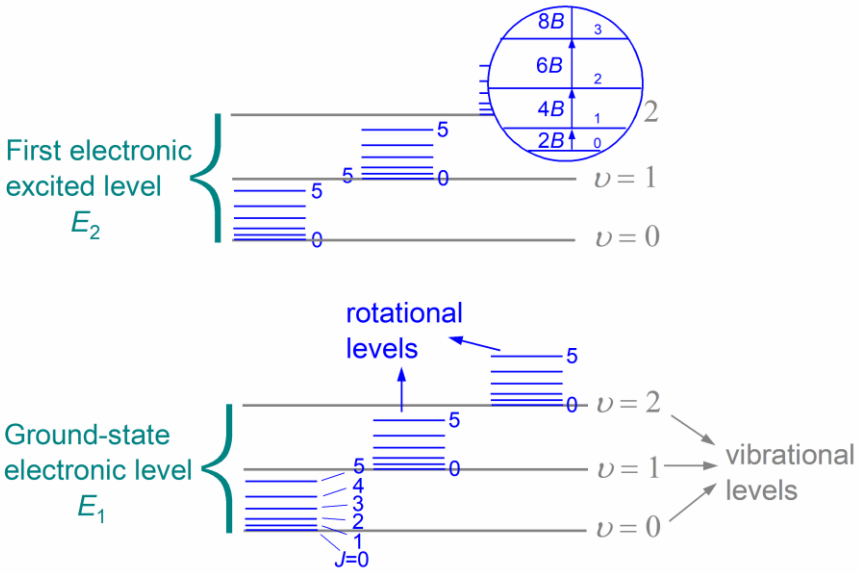

Fig. 2.1 A general energy diagram for a molecule. J and υ denote the rotational and vibrational quantum number, respectively. An enlarged inset at the top-right corner shows the energy separation between the adjacent rotational levels. B is the rotational constant.

The origin of the rotational and vibrational transitions comes from the rotational and vibrational motions of a molecule. If we consider a diatomic molecule as an example, to solve the Schrödinger equation, its molecular motions are approximated as a harmonic oscillator and a rigid rotor, as sketched in Fig. 2.2. The molecule can rotate around any axis through the center of mass (C) as a rigid rotor. In addition, it can also vibrate like a harmonic oscillator by assuming a spring connection with an equilibrium length of R_e.

By solving the time-independent Schrödinger Equation, the energy states concerning the rigid rotor or the harmonic oscillator approximations for a diatomic molecule can be extracted. Here we follow the established derivation found in the literature [Herzberg1950, Demtröder2006, Hertel2015]. For pure harmonic oscillator vibrations, the vibrational energy can be simply quantified in a first approximation assuming a parabolic potential as

$$E_\upsilon = h\nu_e\left(\upsilon + \frac{1}{2}\right) \quad \text{for } \upsilon = 0, 1, \ldots, \tag{2.1}$$

where υ is the vibrational quantum number and ν_e is the vibrational frequency

$$\nu_e = \frac{1}{2\pi}\sqrt{\frac{k}{M_c}} \tag{2.2}$$

with $M_c = M_A M_B / (M_A + M_B)$ to be the effective mass and k to be the force constant. The vibrational term $T_\upsilon = E_\upsilon / hc$ (in cm^{-1}) is often used instead of the energies in spectroscopy.

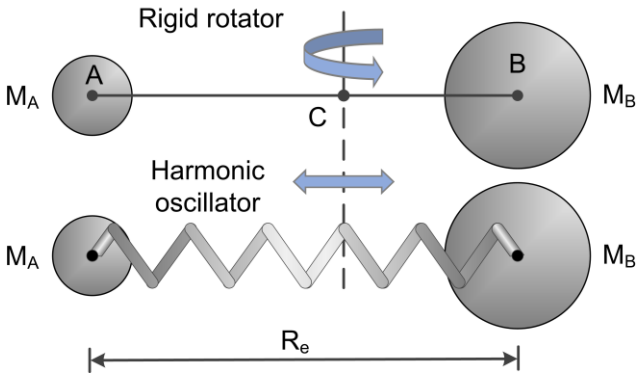

Fig. 2.2 Illustration of the diatomic molecule motions. M_A and M_B are the atomic masses for atom A and B. C represents the center of the mass of the molecule. R_e is the internuclear distance.

For a more precise description, anharmonic contributions must be considered. Then the vibrational term is expressed with higher order terms [Laher1991]

$$T_\upsilon = \omega_e\left(\upsilon+\frac{1}{2}\right) - \omega_e\chi_e\left(\upsilon+\frac{1}{2}\right)^2 + \omega_e y_e\left(\upsilon+\frac{1}{2}\right)^3 - \ldots, \tag{2.3}$$

where $\omega_e = \nu_e / c$ is the molecular vibrational constant and represents the wavenumber, χ_e and γ_e are the higher order anharmonicity factors.

Considering the rigid rotator, the rotational term at the equilibrium position is quantified using the rotational quantum number J [Struve1989, Hertel2015]

$$F_J = B_e J(J+1) \quad \text{for } J = 0, 1, \ldots, \tag{2.4}$$

where $B_e = h/(8\pi^2 Ic)$ is the molecular rotational constant (in cm^{-1}) and is inversely proportional to the moment of inertia $I = M_c R_e^2$.

The separation between the adjacent rotational levels is therefore

$$F_J - F_{J-1} = 2B_e J. \tag{2.5}$$

This energy separation increases linearly with J. A graphical representation is displayed in the inset of Fig. 2.1. As a result, the rotational absorption lines are predicted to be uniformly separated by a spacing of $2B_e$.

Nevertheless, a real molecule is not rigid. When it is rotating, the centrifugal force and the

restoring force work together to hold the atoms together, resulting in a widening of the internuclear distance R_e [Demtröder2006]. Therefore, correction terms are introduced to improve the rigid model [Atkins2006, Demtröder2006], yielding an expression for the rotational term as:

$$F_J = B_e J\left(J+1\right) - D_e J^2 \left(J+1\right)^2 + \ldots, \tag{2.6}$$

where D_e is the centrifugal constant.

Furthermore, interactions between molecular vibrations and rotations may occur, which leads to a modification of the rotational and centrifugal constants [Demtröder2006]

$$B_v = B_e - \alpha_e \left(\upsilon + \frac{1}{2}\right), \tag{2.7}$$

$$D_v = D_e + \beta_e \left(\upsilon + \frac{1}{2}\right), \tag{2.8}$$

where α_e and β_e are the vibration-rotation interaction constants, while B_e and D_e are the rotational and centrifugal constants at equilibrium.

Combining Equations (2.3) and (2.6), the energy (in cm^{-1}) at a particular vibrational level υ and a rotational level J can be expressed as

$$E_{v,J} = T_e + \omega_e \left(\upsilon + \frac{1}{2}\right) - \omega_e \chi_e \left(\upsilon + \frac{1}{2}\right)^2 + B_v J\left(J+1\right) - D_v J^2 \left(J+1\right)^2 + \ldots, \tag{2.9}$$

T_e corresponds to the minimum potential energy of the electronic state.

Based on Equation (2.9), the transition frequencies with regard to a photon absorption, emission or scattering process can be determined by calculating the energy differences between the corresponding vibrational and rotational levels. This is important for both the selection of the excitation sources and simulating of the generated signal.

Some typical rotational (B_e), centrifugal (D_e) and vibrational constants (ω_e) for the most relevant species within this thesis are summarized in Table. 2.1. Clearly the vibrational frequencies are much higher than the rotational ones. From their values, it is evident that there are in general thousands of vibrations for a molecule in a single rotation. In addition, the values of B_e provide a direct view of how closely the rotational spectral lines may be located (Equation (2.5)). Thus, the separation between rotational lines for H_2 is much larger than for CO_2.

Table. 2.1 Rotational, centrifugal and vibrational constants for molecules relevant in this thesis. Those constants are from [a]Laher and Gimore [Laher1991], [b,c,e]Richet et al. [Richet1977], [c]Krupenie [Krupenie1966], [d]Rothman et al. [Rothman1992], [d]Bekerom et al. [Bekerom2018]. Only one representative vibrational constant for the polyatomic molecules is shown here.

Molecule	B_e/cm^{-1}	D_e/cm^{-1}	ω_e/cm^{-1}
N_2[a]	1.9982	5.76×10^{-6}	2358.6
H_2[b]	59.325	-4.66×10^{-2}	4401.1
CO[c]	1.9313	6.12×10^{-6}	2169.8
CO_2[d]	0.3902	1.33×10^{-7}	1341.5
CH_4[e]	5.2406	1.11×10^{-4}	3143.0

Note that there is only one vibrational mode for a diatomic molecule (bond stretch), however, polyatomic molecules have several vibrational modes due to the changes of all bond lengths and angles [Atkins2006]. In the following, we discuss the vibrational energies for CO_2 in more detail as it is the molecule of particular interest in this thesis. As a linear triatomic molecule, CO_2 is symmetric along its nuclei axis and has a symmetry plane perpendicular to the axis. This structure leads to four vibrational modes: the symmetric stretching mode (v_1), the doubly degenerate (in the two dimensions perpendicular to the internuclear axis) bending modes (v_2) and the asymmetric stretching mode (v_3), as shown in Fig. 2.3.

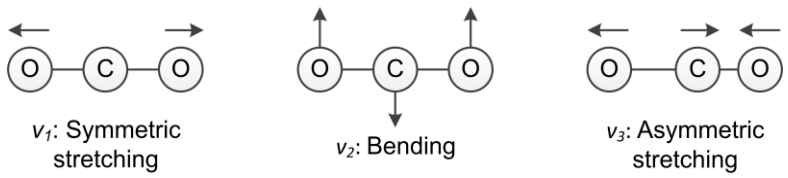

Fig. 2.3 Vibrational modes of CO_2. v_1, v_2 and v_3 are the quantum numbers for the symmetric stretching, doubly degenerate bending and asymmetric stretching mode, respectively.

The different angular momenta projection of the bending vibrations onto the molecular axis are characterized by quantum number l_2. This takes into accounts the fact that the two degenerate bending vibrations can lead to effective rotations around the molecular axis and

thus to different energies if they have appropriate relative phase [Hertel2015]. This angular momentum quantum number can take values $|l_2| = v_2, v_2\text{-}2, v_2\text{-}4, \ldots 1$ or 0 [Hertel2015]. In this regard, a CO_2 vibrational state can be specified as $\left(v_1 v_2^{l_2} v_3\right)$ [Chedin1979, Joly1999].

Another important aspect to consider is that CO_2 has almost the same energy between the symmetric stretching mode v_1 and the overtone of the bending mode $2v_2$ [Fermi1931, Tejeda1995]. Therefore, a coupling, which is called Fermi resonance, occurs. This leads to the generation of the perturbed levels, having slightly shifted energies compared to the unperturbed states. The perturbed levels are generally termed Fermi polyads [Chedin1979]. A typical example of the Fermi resonance is found to happen between the symmetric stretch level of (10^00) and the bending level of (02^00) [Allan2001]. The corresponding perturbed levels are labeled as $(10^00)_1$ and $(10^00)_2$ (the first Fermi polyad) [Chedin1979] and have an energy of ~1388 cm^{-1} and ~1285 cm^{-1}, respectively (Fig. 2.4). Similarly, the Fermi resonance also occurs between the levels of (11^10) and (03^10) [Joly1999, Yagi2008], yielding perturbed levels of $(11^10)_{1,2}$ (the second Fermi polyad). A simplified CO_2 vibrational energy level scheme according to [Chedin1979] is shown in Fig. 2.4, displaying the most common transitions for the first (blue) and the second (red) Fermi polyads. The vibrational transitions corresponding to 1388 cm^{-1} and 1409 cm^{-1} are mainly considered for thermometry in this work.

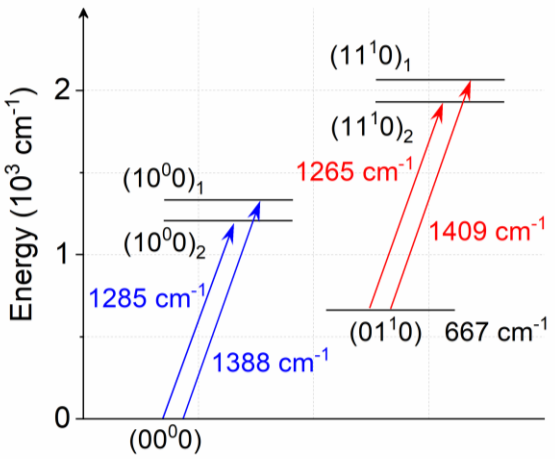

Fig. 2.4 Simplified vibrational energy level diagram of CO_2.

To drive or resolve these transitions in molecular systems (Fig. 2.1 and Fig. 2.4), infrared spectroscopic and Raman spectroscopic techniques are both powerful tools. However, homonuclear diatomic molecules are infrared inactive [Atkins2006]. This limits the use of

the infrared spectroscopy in this study because homonuclear diatomic molecules like N_2, H_2 are the species of the most interest in combustion due to their dominance in the environments. Nevertheless, the selection rule for rotational Raman transitions is that the molecule must be anisotropically polarizable while the one for vibrational Raman transitions is that the polarizability should change as the molecule vibrates [Atkins2006]. In this regard, all linear and diatomic molecules are rotationally Raman active, and diatomic molecules are also vibrationally Raman active. Therefore, Raman spectroscopy has great potential for combustion and gasification investigations. The selection rule for pure rotational Raman transitions is $\Delta J = \pm 2$. For vibrational Raman transitions, the selection rule yields $\Delta \upsilon = \pm 1$. Accompanying the vibrational transition, there are a branch of transitions involving the various rotational states, often termed rovibrational transitions. The selection rules for the rotational transitions are $\Delta J = 0, \pm 2$, corresponding to the so-called Q-branch ($\Delta J = 0$), O-branch ($\Delta J = -2$) and S-branch ($\Delta J = +2$) [Long2002]. Fig. 2.5 shows a brief illustration of the Q-branch Raman transitions and the pure rotational Raman transitions in the ground electronic state. As will be explained in Section 2.3, the Q-branch transitions are stronger than that of the O- and S-branch. They are therefore widely used for a better signal strength.

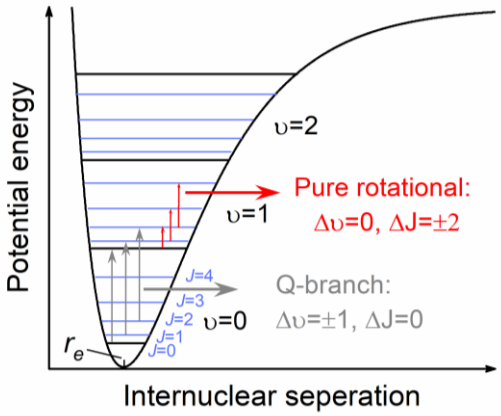

Fig. 2.5 Schematic energy level diagram for molecular Q-branch Raman transitions and the pure rotational Raman transitions. r_e is the bond length of a particular molecule.

2.2 Fundamentals of CARS

Based on the knowledge of the molecular energies and the Raman transitions, this section introduces the CARS process, which is a coherent Raman process, and therefore increased signal levels are expected. It is typically a three-color process, evolving from a third-order

nonlinear interaction between light and matter. Three laser beams known as pump (ω_p), Stokes (ω_{St}) and probe (ω_{pr}) beam are typically focused into a common probe volume and interact with the medium. Then an oscillating polarization is generated as the source of the CARS radiation, which occurs through the third-order nonlinear susceptibility ($\chi^{(3)}\left(\omega_{CARS},\omega_p,\omega_{St},\omega_{pr}\right)$) of the molecule. Moreover, to generate CARS radiation, the incident beams must be aligned such that the phase-matching condition is fulfilled, i.e., $\overrightarrow{k_{CARS}}=\overrightarrow{k_p}-\overrightarrow{k_{St}}+\overrightarrow{k_{pr}}$ [Eckbreth1978], where $\overrightarrow{k_i}$ is the wave vector at the frequency of ω_i. The general condition for CARS phase-matching is shown in Fig. 2.6 (a). The generated radiation includes a resonant CARS contribution (Fig. 2.6 (b)) as well as a nonresonant four-wave mixing (FWM, see Fig. 2.7) one. When the pump and Stokes frequency difference coincides with a Raman-active vibrational or rotational resonance of a molecule, the resonant CARS signal at $\omega_{CARS} = \omega_p - \omega_{St} + \omega_{pr}$ is significantly enhanced.

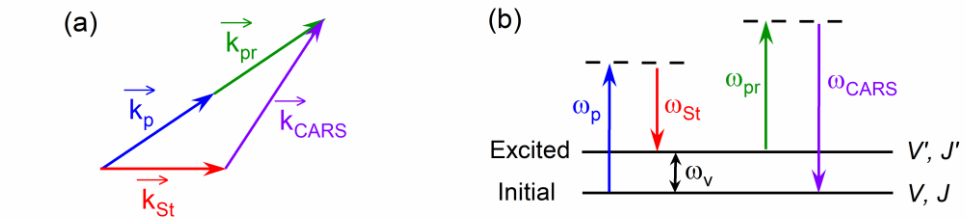

Fig. 2.6 (a) General CARS phase-matching approach. (b) Scheme of the resonant vibrational CARS process energy diagram. ω_p, ω_{St}, ω_{pr} and ω_{CARS} represent the angular frequency of the pump, Stokes, probe and CARS signal, respectively. ω_v shows the Raman transition frequency for a particular molecule. *V* and *J* denote the vibrational and rotational quantum numbers. Virtual and real states are indicated by dashed and solid lines, respectively.

Let us consider a resonant vibrational CARS process as an example, as shown in Fig. 2.6 (b). The target molecule is at first in an initial state and excited to a virtual state by a pump beam. If a simultaneous Stokes beam is present, this virtual state may act as an instantaneous gateway to address a vibrational eigenstate of the molecule. The pump and Stokes beams lead to a coupling between the initial and the excited state and a coherent superposition of the states is generated, namely the Raman coherence [Nibler1979, Lucht2007, Pestov2007]. This coherent superposition is probed by an additional beam, which brings the molecule to a virtual state, from which it instantaneously falls back to the initial state, leading to the emission of a photon at the frequency ω_{CARS}. When broadband fs pump/Stokes beams are applied, a large fraction of rovibrational manifolds contributes to the excitation of the

Raman coherence and oscillate in phase [Lucht2006]. However, after the presence of the pump and Stokes pulses, the rovibrational transitions start to oscillate out of phase at their slightly different natural frequencies. This frequency-spread dephasing results in a Raman coherence decay. The rate of this decay depends on the frequency differences, i.e. the spectral spacings between the simultaneously excited rovibrational transitions, and the probing environments. The details of the CARS theory as well as the simulation model for temperature and concentration determination will be discussed in Chapter 3. Molecules in general have unique Raman transitions ω_v determined from the molecular energies explained in Section 2.1. A summary of the typical vibrational Raman shifts (Raman transition frequencies ω_v in cm^{-1}) for the most relevant molecules in this thesis is shown in Table. 2.2. Note that these values slightly differ from the molecular vibrational constants given in Table. 2.1, where only a harmonic oscillation is assumed for simplicity.

Table. 2.2 Vibrational Raman shifts of the most relevant gaseous molecules. Raman shifts are from [a]Tejeda et al. [Tejeda1995], [b]Krupenie [Krupenie1966], [c]Laher and Gimore [Laher1991], [d]Yu et al. [Yu2007], [e]Richet et al. [Richet1977].

Molecule	Raman shift/cm^{-1}
CO_2[a]	1388, 1285
CO[b]	2143
N_2[c]	2330
CH_4[d]	2917
H_2[e]	4161

The resonant Raman signal arises from the nuclear response of the molecule while the FWM process arises mainly from the distortion of the electronic orbits induced by the incident laser fields [Eckbreth1981]. As shown in Fig. 2.7, the FWM process involves three virtual states. Therefore, FWM occurs instantaneously when pump, Stokes and probe pulses are present and temporally overlap. In addition, it does not depend on molecular Raman resonances, but leads to a nonresonant background.

The electronic origin of the nonresonant contribution gives rise to different symmetric properties compared to the resonant CARS, thus it shows a different polarization dependence on the input laser fields. In this regard, polarization discrimination [Rahn1979]

or a properly delayed probe pulse [Zinth1980] has been applied to suppress the nonresonant contribution for a higher contrast of the resonant CARS signal. Nevertheless, the nonresonant contribution is also utilized deliberately to generate inference with the resonant contribution, for instance, in chirped-probe-pulse (CPP) femtosecond CARS technique [Richardson2013]. It is also reported that the presence of the nonresonant signal may enhance the overall signal level [Richardson2017].

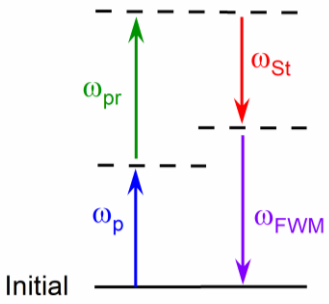

Fig. 2.7 Scheme of the nonresonant FWM process energy diagram. Virtual and real states are indicated by dashed and solid lines respectively.

In practical applications, as shown in Fig. 2.5, pure rotational CARS or rovibrational CARS can both be used for diagnostics. Conventionally, when N_2 is used as the probing molecule, thermometry based on rovibrational CARS is mainly derived from the relative ratio of the fundamental ($\upsilon=1\rightarrow\upsilon=0$) and the first hot band ($\upsilon=2\rightarrow\upsilon=1$) vibrational transitions [Miller2010]. Since the first hot band typically starts to appear at $\gtrsim$1000 K, this limits its sensitivity to high temperature levels. For pure rotational CARS, its temperature sensitivity primarily depends on the distribution of the rotational states in the ground vibrational level, therefore, it can be sensitive even at ambient temperatures (e.g. 300 K).

2.3 Molecular populations and Raman cross section

In CARS diagnostics, molecular population distributions and Raman cross section are of primary importance. Because how the molecules are distributed or partitioned over the allowable internal energy modes is temperature dependent. In addition, the strength of Raman scattering is sensitive to the molecular concentration and it is characterized by the Raman cross section. In this regard, this section introduces these two aspects.

The molecular population distribution obeys the Boltzmann distributions and can be

described by [Eckbreth1996]

$$N_j = N\frac{g_j e^{-E_j/kT}}{\sum_j g_j e^{-E_j/kT}}, \tag{2.10}$$

where N_j is the number density of molecules in the j_{th} molecular level with energy E_j, N is the total number density, k is the Boltzmann's constant, T is the temperature of the probe volume, and g_j is the degeneracy of the state. The denominator in Equation (2.10) is the partition function:

$$Q = \sum_j g_j e^{-E_j/kT}, \tag{2.11}$$

which is the sum of all the internal energy modes for a molecule. By electronic, vibrational, and rotational excitation, a molecule can attain many energy states. The internal molecular energy distribution can be assumed to be additive and expressed as [Gamache2017]

$$E = E_{ele} + E_{vib} + E_{rot} + \ldots. \tag{2.12}$$

Combining Equations (2.11) and (2.12), we see that the total partition function for a molecule may be expressed as the product of partition functions for each internal energy mode

$$Q = Q_{ele} \cdot Q_{vib} \cdot Q_{rot} \cdot \ldots. \tag{2.13}$$

Similarly, the total degeneracy can be written as the product of the degeneracies of the individual internal energy modes.

For the ambient conditions investigated in this thesis, the CARS process occurs in the electronic ground state, and the main internal energy modes of interest are from the vibrational and rotational motions. Therefore, the product of vibrational and rotational partition functions ($Q_{vib} \cdot Q_{rot}$) is used to approximate the total internal partition function of the molecules [Fischer2003].

The vibrational partition function can be expressed as [Eckbreth1996]

$$Q_{vib} = \sum_{\upsilon=0}^{\infty} e^{-\upsilon hc\omega_e/kT} \xrightarrow[simplified]{convergent} \frac{1}{1-e^{-hc\omega_e/kT}}, \tag{2.14}$$

similarly with what is shown in Section 2.1, υ is the vibrational quantum number and $\omega_e = \nu_e/c$ is the vibrational constant.

Based on Equations (2.10), (2.11) and (2.14), the vibrational population can be written as [Eckbreth1996]

$$N_{vib} = N\frac{e^{-\upsilon hc\omega_e/kT}}{Q_{vib}} = Ne^{-\upsilon A\omega_e/T}\left(1-e^{-A\omega_e/T}\right), \tag{2.15}$$

where $A=hc/k$=1.44 K/cm^{-1} is used to simplify the expression.

The rotational partition function is expressed with a (2J+1) degeneracy as [Eckbreth1996]

$$Q_{rot} = \sum_{J=0}^{\infty}(2J+1)\exp[-A\cdot\ B_vJ\left(J+1\right)/T], \tag{2.16}$$

where J is the rotational quantum number and B_v is the rotational constant.

Similar to Equation (2.15), the corresponding rotational population distribution is then written as [Eckbreth1996]

$$N_J = \frac{N}{Q_{rot}}g_I\left(2J+1\right)\exp[-\frac{A\cdot\ B_vJ(J+1)}{T}], \tag{2.17}$$

where g_I is the nuclear spin statistical weight and it is dependent on J for nonzero nuclear spin, which is caused by the spins of the nuclei that are not interchanged in symmetry operations of a molecule [Herzberg1945]. For the diatomic molecules relevant in this thesis (N_2, H_2 and CO), the values of g_I are listed in Table. 2.3. Concerning triatomic molecule CO_2, for the $(00^00)\rightarrow(10^00)_{1,2}$ transitions, g_I = 1 for odd J and g_I = 0 for even J. For the $(01^10)\rightarrow(11^10)_{1,2}$ transitions, g_I = 1 for all $J \geq l_2$ (l_2 is the quantum number for quantifying the angular momenta of the bending modes as introduced in Section 2.1) [Finsterhölzl1982]. For CH_4, as a tetrahedral molecule, its rotational levels with definite J split into a number of sublevels of A, E and F types, with g_A = 5, g_E = 2, g_F = 3, respectively [Wilson1935, Kozlov1979, Jourdanneau2005]. The statistical weights associated with each rovibrational level are calculated according to Wilson et al. [Wilson1935].

Table. 2.3 Nuclear spin statistical weights for the relevant diatomic molecules in this thesis. The data are from [a,b]Long [Long2002] and [c]Gamache [Gamache1990].

	N_2[a]	H_2[b]	CO[c]
J odd	3	3	1
J even	6	1	1

Combining Equations (2.15) and (2.17) to consider both vibrational and rotational levels, the temperature dependent molecular population distribution can be deduced from (2.10) to be

$$N_{vib,J} = \frac{Ne^{-\upsilon A\omega_e/T}}{Q_{vib}Q_{rot}} g_I (2J+1)\exp[-\frac{A\cdot B_v J(J+1)}{T}]. \quad (2.18)$$

For a given temperature, the population distributions can be determined based on Equation (2.18). Reversely, when the population distributions are recorded from the measured CARS spectrum, the temperature at the probe volume may be retrieved. In the CARS modeling implemented in this thesis (Section 3.2), the values of Q_{vib} and Q_{rot} are taken from Gamache et al. [Gamache2017].

An intuitive understanding, how molecular populations are transferred into CARS spectra, is shown in Fig. 2.8. The calculated rotational population distributions for N_2 according to Equation (2.17) at three different temperatures are displayed. The variation of the population distribution with temperature is displayed. In general, the most populated J level is shifting to a higher level as temperature goes up. These distributions can be mapped to the measured CARS spectra when sufficient probe spectral resolution is provided.

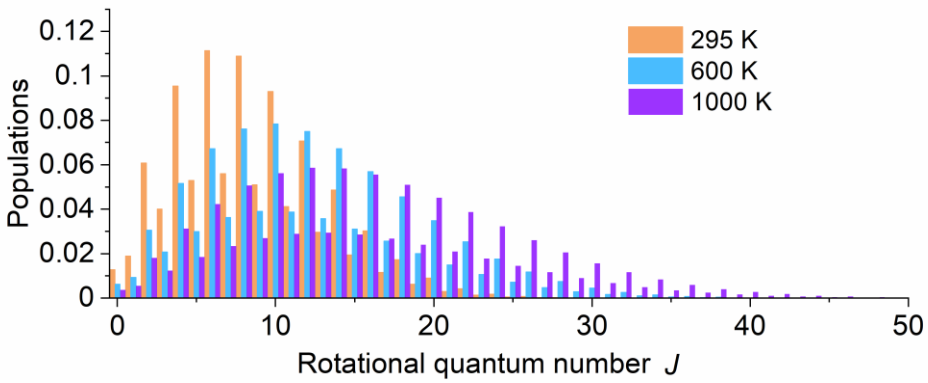

Fig. 2.8 Calculated N_2 rotational population distribution at 295 K, 600 K and 1000 K. The results are normalized to the total number density.

The vibrational distribution calculated from Equation (2.15) is shown in Fig. 2.9, where one can observe that only when the temperature is beyond 1000 K, the N_2 population starts to distribute on the second vibrational state. Up to 2500 K, mainly the first three vibrational states are populated. Still, the first vibrational state dominates for the entire temperature range shown in Fig. 2.9.

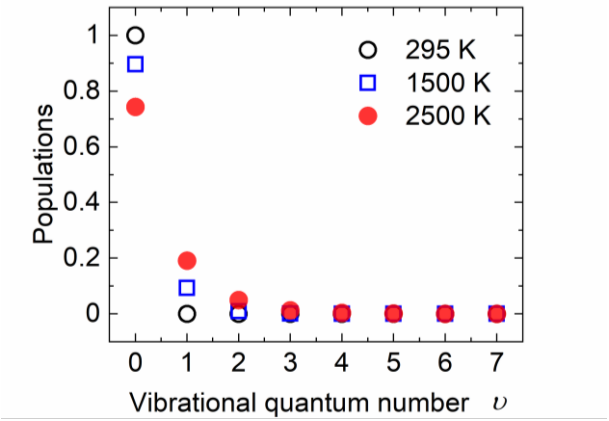

Fig. 2.9 Population distribution of N_2 for vibrational states from $\upsilon = 0$ to $\upsilon = 7$ at 295 K, 1500 K and 2500 K. The results are normalized to the total number density.

The Raman cross section with regard to the strength of the Raman scattering can be expressed as [Tejeda1995, Long2002, Marrocco2009b, Richardson2011]:

$$\left(\frac{d\sigma}{d\Omega}\right)_{i,n} = \frac{\pi^2}{\varepsilon_0^2}\left(\tilde{\nu}_{pr}+\tilde{\nu}_n\right)^4 \frac{\hbar\upsilon}{2m_i\omega_n}\left(\left(a'\right)_i^2 F_a\left(J\right)+\frac{4}{45}b_{J,J}\left(\gamma'\right)_i^2 F_\gamma\left(J\right)\right) = \frac{\pi^2}{\varepsilon_0^2}\left(\tilde{\nu}_{pr}+\tilde{\nu}_n\right)^4 M_n^2 \quad (2.19)$$

Where i denotes the gas species and m_i is its molecular mass. ω_n ($\omega_n = 2\pi\tilde{\nu}_n$) is the angular transition frequency for the transition n. $\tilde{\nu}_{pr}$ is the wavenumber of the probe pulse. $\left(a'\right)_i^2$ and $\left(\gamma'\right)_i^2$ are the mean and anisotropy invariants of the polarizability tensor for species i. M_n represents the transition dipole moments, following the expression given by Tejeda et al. [Tejeda1995]. $F_{a,\gamma}\left(J\right)$ are the Herman-Wallis factors reflecting the influence of the centrifugal force on the spectral line intensities [Marrocco2009b]:

$$F_{a,\gamma}\left(J\right) = 1-\left(3\left(a_1+1\right)/2-4\left(p_2/p_1\right)_{a,\gamma}\right)\gamma^2 J\left(J+1\right), \quad (2.20)$$

where a_1 is Dunham anharmonic force constants, $p_{1,2}$ is the coefficient of the isotropic/anisotropic polarizability expansion. $\gamma = 2B_e/\omega_e$ is the rovibrational coupling. The subscripts a and γ denote the isotropic and anisotropic components, having different values for p_2/p_1.

In addition, $b_{J,J}$ is the Placzek-Teller coefficient, which has different expressions depending on the transitions [Eckbreth1996]:

$$b_{J,J} = \frac{J(J+1)}{(2J-1)(2J+3)}, \quad J \rightarrow J, \text{ Q-branch} \tag{2.21}$$

$$b_{J+2,J} = \frac{3(J+1)(J+2)}{2(2J+1)(2J+3)}, \quad J \rightarrow J+2, \text{ S-branch} \tag{2.22}$$

$$b_{J-2,J} = \frac{3J(J-1)}{2(2J+1)(2J-1)}, \quad J \rightarrow J-2, \text{ O-branch} \tag{2.23}$$

In this thesis, we focus on the Q-branch transitions. Indeed, for S- and O-branch transitions, the Raman cross section expressions have only the anisotropic term ($(\gamma')_i^2$) but not the mean polarizability term ($(a')_i^2$) shown in Equation (2.19) [Herman1996]. This makes the Q-branch transitions stronger than the S- and O-branch ones.

The following parts show the parameters used to calculate M_n or the sources where the transition dipole moments are taken from. For N_2 and H_2, the Herman-Wallis factors are calculated according to Equation (2.20) using the parameters shown in Table. 2.4. Based on this, their transition dipole moments can be calculated.

Table. 2.4 Molecular parameters for Herman-Wallis factor determination [Marrocco2009a].

Molecule	a_1	$(p_2/p_1)_a$	$(p_2/p_1)_\gamma$
N_2	-2.7	0.31	0.57
H_2	-1.6	0.27	0.79

The Herman-Wallis factor originates from the centrifugal force. Therefore, its influence is more pronounced for very light molecules (e.g. H_2) where the coupling between the vibrational and rotational motions is large [Marrocco2009b]. Indeed, the Herman-Wallis factor for N_2 deviates less than 2% from unity for temperatures up to ~1000 K [Marrocco2009a]. Therefore, for other relevant molecules in this thesis, the Herman-Wallis factors are omitted.

The transition dipole moments for the main vibrational Raman transitions of CO_2 are listed in Table. 2.5. For CO and CH_4, the transition dipole moments are calculated according to Richardson et al. [Richardson2013] and Penney et al. [Penney1972] to be ~6.23×10^{-42} $CV^{-1}m^2$ and ~17.35×10^{-42} $CV^{-1}m^2$, respectively.

Table. 2.5 Raman shift $\tilde{\nu}_{jf}$ and the transition dipole moments M_n [Tejeda1995] for the first two Fermi polyads (Fig. 2.4) of CO_2.

$\tilde{\nu}_{jf}$ /cm^{-1}	M_n / 10^{-42} CV^{-1}m^2
1265.1	5.40
1285.4	5.58
1388.2	6.79
1409.5	7.20

2.4 Nanosecond and picosecond CARS

2.4.1 Nanosecond CARS

Before introducing our approach of CARS measurements, we present briefly an overview of the existing CARS techniques. The first investigations using CARS in gas phase were implemented with nanosecond lasers. Regnier et al. [Regnier1974] focused 40 ns pulses delivered from a Q-switched ruby laser to a stimulated Raman scattering (SRS) cell filled with H_2 and He at a pressure of 30 atm. The generated SRS signal corresponding to the Q(1) vibrational transition of H_2 was utilized as the Stokes beam. This beam combined with the residual seed laser were focused into H_2 gas samples for generating CARS signals in a collinear phase-matching condition. Using this configuration, the authors showed that the H_2 CARS intensity is proportional to the square of its number density. Based on a similar ruby seed laser with 20 ns pulse duration at 694.3 nm, Moya et al. used 70% of the amplified ruby laser pulses to pump a dye laser [Moya1975]. The generated pulses emitted at ~950-1000 nm served as the Stokes signal, which was appropriate for the Raman excitation of the vibrational H_2 transitions. In this regard, temperature measurements from H_2 CARS were reported. Although only one probing species or a single vibrational transition was excited due to the limited available wavelengths of the lasers, these pioneering works demonstrated the advantages and capabilities of the CARS techniques in aerodynamic flows. Since then CARS measurements have been widely demonstrated in various practical combustion devices [Eckbreth1996].

In the past decades, numerous ns-laser-based CARS experiments were performed based on

a broadband multiplex CARS system, where a narrowband pump beam and a relatively broadband Stokes beam are used to excite a large fraction of the rovibrational transition spectrum of a particular molecule. A probe beam identical to the pump is applied and scattered off by the excited molecule to generate the CARS signal [Roh1976, Hahn1997]. In contrast to systems with only narrowband beams, this avoids the necessity of scanning the wavelength and enables single-shot instantaneous (~10 ns) diagnostics for practical applications with turbulent flows [Greenhalgh1985]. Based on this, temperature measurements were demonstrated in hydrogen/air flames respectively from N_2 and H_2 CARS using a Stokes beam provided from a dye laser with different dyes in a methanol solvent [Hancock1997]. The precision of this method is usually limited by the mode competition effects in the broadband laser source and the detector noise [Greenhalgh1985, Pealat1985]. Employing an amplified spontaneous emission (ASE) laser with no spectral modulation from discrete modes [Ewart1985] as the broadband Stokes beam, an improvement in precision of single-shot temperature measurements was presented [Snowdon1991]. Besides, additional laser-induced-perturbations may need to be considered. Spectral line broadening for the Q-branch N_2 CARS transitions due to the Stark effect was reported when the pump laser intensity was larger than 185 GW/cm^2 [Woodmansee2002]. By increasing the pump and Stokes laser intensities simultaneously, the authors reported on a stimulated Raman pumping effect, where the laser started to populate the first vibrational transition that is not Boltzmann population related.

For high-pressure environments, Hall et al. [Hall1980] reported the pressure-induced narrowing of the rovibrational N_2 CARS spectrum. This phenomenon comes from the rapid collisional energy transfer in the rotational states under high enough pressures, namely the so-called collisional narrowing [Hall1980]. The resulting N_2 Q-branch CARS spectrum tends to radiate at an average frequency while the contrast of the isolated rovibrational lines decreases and some even vanishes. This may complicate the temperature determination at higher pressures, but to some extent, helps for pressure measurements. Kuehner et al. presented pressure measurements at 0.1-4.0 atm using an ASE laser [Ewart1985] as the Stokes source [Kuehner2003]. The temperatures were also determined but at a relatively low range of 100-300 K.

The above-mentioned broadband multiplex CARS typically enables probing of only one species. To overcome this limitation, dual-broadband CARS was introduced. Eckbreth et al. [Eckbreth1985] proposed the use of two broadband laser sources (150-200 cm^{-1} FWHM) in

combination with one narrowband laser for CARS measurements. The proper center wavelength shifting between the two broadband lasers enables rovibrational Raman excitation of multiple molecules with Raman shift differences within their bandwidth (e.g. N_2, CO). The narrowband laser together with either of the broadband lasers may excite additional rovibrational transitions (e.g. CO_2, O_2). The simultaneous excitation of multiple species was therefore obtained. Using a similar setup, simultaneous excitation of rotational transitions with the vibrational ones were demonstrated [Aldén1986]. In addition, for multi-species excitation, dual-pump or triple-pump CARS techniques were introduced. Lucht et al. [Lucht1987] presented simultaneous N_2 and O_2 CARS measurements using one broadband Stokes beam (100 cm^{-1} FWHM) and two narrowband pumps with one pump beam tunable. Employing four laser beams, Roy et al. [Roy2003] showed the simultaneous measurement of two pairs of combustion molecules in an atmospheric pressure flame. Combining the dual-broadband CARS with the dual-pump CARS, the authors presented the simultaneous excitation of vibrational N_2/CO_2 pairs with the rotational N_2/O_2 pairs [Roy2004].

Despite ns-laser-based CARS has been well-developed, an intrinsic obstacle is the presence of the pronounced nonresonant background. Its interference with the resonant CARS disturbs the measured CARS spectrum for temperature and concentration extraction [Roy2010a]. Although the nonresonant background may be suppressed by polarization-sensitive techniques [Rahn1979], a significant reduction of the CARS signal was reported [Eckbreth1981]. In addition, combustion devices require glass windows for optical access. It was reported that polarization-sensitive technique may fail due to the pressure-induced birefringence in the cell window at a sub-atmospheric pressure [Roy2002, Roy2010a]. Besides, the unavoidable molecular collisions in ns time scale usually require complicate models. To overcome the above-mentioned obstacles, CARS techniques based on ps or fs lasers were explored.

2.4.2 Picosecond CARS

Ps-laser-based CARS permits the nonresonant signal suppression by a properly delayed probe pulse. Kamga et al. [Kamga1980] reported a nonresonant background reduction by a factor of 100 using a probe at ~20 ps delay for vibrational CARS of CS_2 in toluene. Using a combination of a 135 ps pump, a 106 ps Stokes and a 135 ps probe pulse delayed at 165 ps, a three order of magnitude reduction of the nonresonant contribution of rovibrational N_2

CARS was demonstrated in a hydrocarbon-air flame while the CARS signal preserved 60% to 80% of its original intensity [Meyer2007]. This nonresonant reduction is larger than what can be achieved via polarization-sensitive approaches, besides, is not subject to the birefringence of the cell window or density gradients. Based on the ps delay regime, Seeger et al. [Seeger2009] investigated the pure-rotational CARS using a ~100 ps probe. The authors reported that collisions occur in the time interval of the pump and probe pulses (at ~150-500 ps probe delays), which cause a significant change of the CARS spectrum. Thus, although the nonresonant contribution can be largely reduced in ps CARS, the molecular collisions remain to be an obstacle. Accurate time-dependent collisional models for different molecules were required to extend the feasibility of the temperature and concentration determination [Seeger2010, Kliewer2011]. Apart from that, based on the time-resolved ps rotational CARS with sufficient spectral resolution, Kliewer et al. [Kliewer2011, Kliewer2012] reported J-dependent Raman linewidth measurements from the exponential decay of individual rotational transitions. By combining two ps lasers for Raman excitation with a ns laser for probing, Nordström et al. [Nordström2015] reported Raman linewidth measurements from rotational CARS coherence decay. These accurate Raman linewidth measurements would in turn help to improve the measurement accuracies in ns-CARS or ps-CARS where collisional effects must be considered.

2.5 Femtosecond-laser-based CARS

The development of fs laser systems in the past two decades has extended the range of applications for CARS measurements significantly. Fs-laser-based CARS generally shows several advantages: (1) Numerous pump-Stokes pairs underneath the broadband frequency envelope of the pump and Stokes beams may contribute to a significant Raman coherence in the medium [Lucht2007]. Based on fs-lasers, a schematic illustration for highly efficient excitations of the Raman coherence is shown in Fig. 2.10. Multiple pump-Stokes pairs are shown to contribute for the N_2 Q-branch vibrational excitations around 2330 cm^{-1}. (2) High repetition rate fs-lasers enable much faster detection rates (e.g. kHz) compared to ns-lasers [Roy2010a]. (3) If the pump, Stokes, and probe beams are at a fs level, the dynamic study of the molecular collisions or dephasing on fs temporal scale may be possible [Lucht2006]. (4) Pump and Stokes contributions provided from the same pulse can simplify the CARS setup with two-beams or even single-beam configurations [Dudovich2002, Bohlin2013]. (5)

The possibility of probing within a few ps range enables collision-free measurements, which may greatly simplify the collisional modeling and reduce the cost of computation [Lucht2006]. This holds advantages for practical high-pressure investigations, which are unachievable using ns- or ps-CARS.

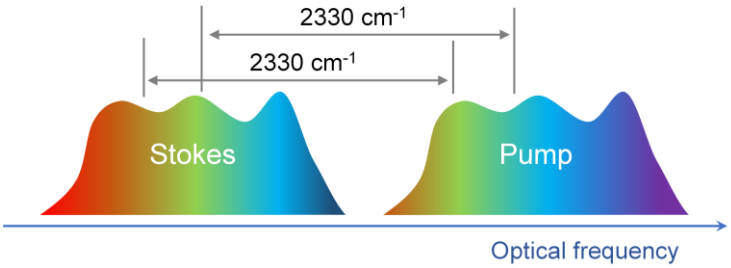

Fig. 2.10 Illustration of using the fs-lasers to provide multiple pump and Stokes pairs for the excitation of Q-branch vibrational N_2 around 2330 cm^{-1}.

2.5.1 Time-resolved femtosecond CARS

The first temperature measurement employing fs-laser-based CARS was carried out by Lang et al. [Lang1999], who used three 100 fs beams to measure the H_2 CARS signal intensities at probe delays of 0-600 ps. They then extracted the temperature from the CARS transients. Using a similar configuration, Knopp et al. [Knopp2002] reported that the time-resolved N_2 CARS signals are sensitive to pressure. The influence of collisions on the time-resolved CARS signal was shown to appear after ~20 ps at pressures up to 5 bar. Furthermore, Lucht et al. [Lucht2006] performed time-resolved fs CARS measurements using a 1 kHz, 45 fs Ti:Sapphire laser. The authors determined the temperature and concentration of N_2 in Ar from the dephasing of the Raman coherence in the first few picoseconds that is much less than the characteristic dephasing collision time of the Q-branch N_2 (~106 ps at atmospheric pressure and temperature) [Lucht2006]. Afterwards, Roy et al. [Roy2008] performed temperature measurements in an H_2-air diffusion flame using time-resolved fs CARS at the first few ps after the initial impulsive excitation. It was concluded that the systematic errors in fs-CARS are reduced compared to ns-CARS, because no collisions affect fs-CARS in the first few ps, therefore, no knowledge of collisional relaxation or Raman linewidths is required [Roy2008]. In further investigations by Wrzesinski et al. [Wrzesinski2013], it was shown that fs-CARS measurements, which are free from collisions, can be implemented up to 50 bar for signals at 1-3 ps probe delay range. These investigations provided an instructive guide of choosing proper probe delays

for diagnostics.

2.5.2 Chirped-probe-pulse (CPP) femtosecond CARS

The above-mentioned time-resolved fs CARS measurements usually require to scan the probe pulse after the impulsive Raman excitation. In this regard, the obtained diagnostic results may be an average over the time interval of scanning. It is therefore not ideal for dynamic measurements in a reactive flow or other harsh chemical conditions.

Lang et al. [Lang2002] proposed a single-shot fs CARS technique by introducing a chirped-probe-pulse (CPP). They used two 100 fs beams for H_2 Raman excitation, while an additional 100 fs pulse was coupled into a 6 cm SF-10 rod to introduce a linear chirp, stretching the pulse length to ~500 fs. The chirped probe pulse maps the CARS transient to the frequency domain, thus, simultaneous spectral- and time-resolved CARS signal was obtained in one measurement. A schematic illustration of the CPP fs CARS process is sketched in Fig. 2.11.

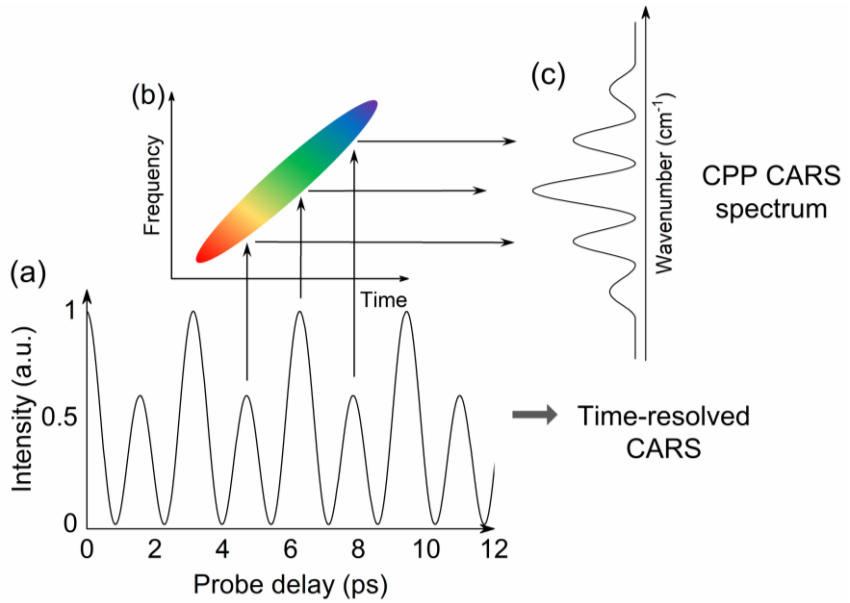

Fig. 2.11 Schematic diagram of the CPP CARS technique. (a) Time-resolved fs CARS signal. (b) Chirped probe pulse. (c) CPP fs CARS spectrum mapped from the chirped probe pulse.

Based on a similar configuration, Roy et al. [Roy2009a] investigated the single-shot thermometry from N_2 CARS using laser pulses generated from a 1 kHz, 85 fs Ti:Sapphire regenerative amplifier. The probe pulse was linearly chirped with a 30 cm SF-10 rod to extend its temporal duration to ~2.5 ps. However, for molecules with close Raman shifts (e.g. N_2 and CO, or CO_2 and O_2), the broad CPP CARS spectrum mapping using the chirped

probe pulse leads to an overlap and interference from different molecules, therefore, complicating the measured CARS spectra and correspondingly increasing the computational cost for temperature and concentration determination.

Up to now, nearly all reported CPP CARS measurements were implemented at a probe delay, where a pronounced nonresonant background was present [Richardson2017]. This results in an enhanced overall signal intensity but does not improve the measurement accuracy or precision [Richardson2013]. Besides, it adds additional complexity to the calibration procedure of this technique. Despite its complexity, thermometry in a swirl-stabilized, atmosphere-pressure, methane-air flame was reported based on CPP fs CARS [Dennis2016, Slabaugh2016]. Recently, Gu et al. [Gu2020] performed the CPP fs CARS thermometry in CO_2-O_2 gas mixtures. CPP CARS spectra at a long probe delay (~7 ps) were used to eliminate the O_2 resonant contribution and extract temperatures from the CO_2 CARS spectra. The authors showed an improvement in numerical efficiency and accuracy for CARS spectral fitting due to the sufficient suppression of the nonresonant signal and the interference pattern from other species. To date, most of the CPP fs CARS based measurements focused on temperature measurements, a few concentration measurements based on this technique were reported for nonreactive binary gas mixtures at atmospheric pressure [Richardson2013, Gu2020].

2.5.3 Hybrid femtosecond/picosecond CARS

The above-mentioned time-resolved fs CARS enables investigations with a good temporal resolution, but compromises the CARS spectral resolution. Although CPP fs CARS spectra display the features in the frequency domain, the spectrum is highly dependent on the chirp features of the probe pulse and not directly related to individual Raman transitions. In this regard, Prince et al. [Prince2006] proposed a novel hybrid fs/ps CARS approach by combining two 50-60 fs pump and Stokes beams to induce Raman excitations in condensed phase R6G, and a properly delayed narrowband ps probe for simultaneous frequency- and time-resolved CARS measurements. Pestov et al. [Pestov2007] combined two ~50 fs transform-limited pulses with a narrowband (several hundred fs) probe and measured the CARS signals of sodium dipicolinate powder. The same group then first implemented this method for the sensing of gas phase molecules [Pestov2008a]. Afterwards, Miller et al. [Miller2010] performed the hybrid fs/ps CARS thermometry from the N_2 vibrational manifold at a flame temperature of ~2013 K using two 100 fs pump and Stokes beams and

a 2.5 ps probe beam. The same group reported on hybrid fs/ps CARS thermometry from N_2 pure rotational signatures at 306-700 K utilizing a ~8.4 ps probe for sufficient spectral resolution [Miller2011b]. They showed that the measured temperatures are collision-free for probe delays below 30 ps at atmospheric pressure. Depending on the measurement purpose and the testing environment, the selection of the probe pulse characteristics was proven to be a key factor, therefore comparisons using a probe with different pulse durations [Kearney2013] and pulse profiles [Miller2011a] were reported. Thermometry from pure rotational CARS spectra showed a better tolerance for the spectral resolution provided from the probe pulse, while a clear decrease of the accuracy was shown for concentration determination if the spectrum was coarsely resolved [Kearney2013]. As thermometry from rovibrational N_2 CARS spectra usually requires high spectral resolution ($\leq$1 cm^{-1}), the major challenge lies in the balance between the probe spectral resolution and its energy. Because of this, hybrid fs/ps CARS techniques using N_2 vibrational spectra were mainly reported at flame temperatures using the first hot band ($\upsilon = 2 \rightarrow \upsilon = 1$) that only starts to appear at ~1000 K. To increase the spectral resolution of the probe, Scherman et al. [Scherman2016] utilized a volume Bragg grating to achieve a narrow probe bandwidth of 0.7 cm^{-1}. In this regard, they resolved the rovibrational structure of the N_2 Q-branch. The same group reported on the amplification of the probe, using a master oscillator power amplifier (MOPA) architecture to generate a 100 µJ, 58 ps probe pulse with a bandwidth of 0.37 cm^{-1} [Santagata2019]. Based on this, N_2 thermometry was reported in ambient air and atmosphere-pressure flames.

2.5.4 Ultrabroadband CARS

The above-mentioned fs CARS techniques mainly focus on temperature measurements from a single molecule. In an impulsive Raman excitation process, the electric field of the pump pulse can efficiently excite the modes having a vibrational period longer than the pulse duration [Polack2005]. Therefore, a sufficient short pump pulse can offer the opportunity to simultaneously excite the Raman transitions of multiple species, which may simplify the concentration determination without interference like in CPP fs CARS or in pure rotational spectra. In this regard, Polack et al. [Polack2005] proposed a single-beam CARS microscopy approach. A fs pulse having a ~95 nm bandwidth was used to simultaneously excite the Raman modes at ~(788-1210) nm in toluene. A spatial light modulator (SLM) was applied to shape the polarization of a small portion of the spectrum to generate the

probe. In a similar manner, single-beam CARS on gaseous N_2 or CO_2 using a shaped 7 fs pulse was reported [Roy2009b, Roy2010b]. However, the damage threshold of the shaping device limits these measurements to qualitative results. Furthermore, Bohlin et al. [Bohlin2014b] suggested a two-beam ultrabroadband CARS configuration. The group used a sub-10 fs ultrashort pump/Stokes pulse generated in a hollow-core fiber (HCF) and a ~90 ps, 30 mJ probe pulse with 20 Hz repetition rate for imaging of the gas molecules. In this way, multi-species detection for Raman shifts up to ~4200 cm^{-1} was illustrated [Bohlin2014a]. However, the use of the probe pulse with long duration made collisional effects unavoidable even at atmospheric pressure. Based on this method, the group reported on measurements of the temperature and the major species distribution in the near-wall region of a methane/air flame [Bohlin2017]. In addition, Kerstan et al. have recently shown a two-beam ultrabroadband CARS configuration based on an ultrabroadband ~7 fs pump/Stokes pulse generated from a HCF filled with neon at ~6.5 bar and using a separate ~1.4 ps probe pulse [Kerstan2017].

2.6 Approach and objectives of this thesis

CARS thermometry and concentration measurements have been extensively investigated over the past few decades. The progress in fs-laser technology, especially in the generation of sub-10 fs pulses allows measurements for more complex probing environments, which may extend CARS techniques to a wider range of applications. The current challenges mainly lie on: (1) Simultaneous temperature and concentration determination from multi-species. Up to now, most of the reported CARS thermometry investigations are performed for N_2 or H_2, while for applications like coal gasification, CO_2 is one of the major species [Irfan2011]. For multi-species detection, ultrabroadband excitation from sub-10 fs laser sources would be highly beneficial, as all species are displayed in a single spectrum. Yet, the bandwidth of the fs pulses and their shot-to-shot fluctuations can significantly influence the measurement capability, accuracy and precision. (2) High-pressure temperature and concentration measurements. Recently reported high-pressure fs-CARS experiments were mainly performed at room temperature [Lucht2006, Miller2012, Wrzesinski2013, Kearney2015, Gu2019]. Although there are some high temperature measurements performed at elevated pressures [Vestin2007b, Stauffer2018], the high-pressure investigations using sub-10 fs laser sources are far from entirely explored. (3) Nonresonant

spectral referencing with a high reliability. The ultrabroadband fs-pulses typically generated from HCFs have complex spectral intensity and shape due to the self-phase modulation (SPM) acquired within the fiber [Gallmann2006]. Therefore, the shot-to-shot fluctuations of the ultrabroadband pulses may reduce the accuracy of the ex-situ spectral referencing measurements while the in-situ referencing is still quite challenging with less sacrifice of the CARS signal intensity.

Therefore, this thesis aims at developing and characterizing ultrabroadband CARS for thermometry and concentration measurements for gasification diagnostics, addressing the above-mentioned challenges. Thereby, we intend to benefit from the collision-free detection of the hybrid fs/ps CARS approach, using a sufficiently short probe pulse. Furthermore, the ultrabroadband approach should allow the simultaneous detection of multiple species. In this regard, our investigations focus on a two-beam ultrabroadband CARS configuration. Based on a 200 kHz dual-output optical parametric chirped pulse amplification (OPCPA) system, a ~7 fs ultrabroadband output is utilized as the pump/Stokes beam for simultaneous multi-species excitation. A second output is adjusted to a pulse duration of ~2 ps acting as probe. The following objectives are investigated in this thesis:

- Objective 1: Temperature determination from different gasification or combustion related molecules (e.g. CO_2, N_2, H_2) using a single CARS setup, with special attention on the use of CO_2.
- Objective 2: Concentration determination for multiple species from a single CARS spectrum. The improvement applying nonresonant spectral referencing will be quantified and analyzed.
- Objective 3: To investigate temperature and concentration determination under high pressures (up to 20 bar) with a special focus on circumventing collisional aspects.
- Objective 4: Applying the ultrabroadband CARS for energy conversion processes. This will be demonstrated as an example for the in-situ investigation of gasification processes (see below).

2.7 Coal gasification

Gasification is an incomplete combustion of coal or another solid feedstock with goals primarily on (1) converting the entire feed fraction to gases, (2) producing gases that preserve the heat of the combustion value at most [Bell2011]. Coal, as one of the important

feedstocks, is the focus of the gasification investigations in this thesis. To develop optimized gasifier designs, a variety of reaction kinetics at high temperatures and pressures are demanded. Established methods for studying the kinetics include drop tube furnace (DTF) and thermogravimetric analysis (TGA) [Küster2017]. In a DTF the coal particle drops from the top of the tube and then the reaction rate is determined from the coal particle/gas composition at the bottom of the tube [Kajitani2002]. TGA monitors the weight of the coal samples as a function of time or temperature using a balance [Zolin1998]. Clearly, both techniques give indirect information about the gasification process. The products of the coal gasification process largely depend on the gas composition and, therefore, its source. With coal as the carbon source, the most important reactions involve the gases of oxygen, hydrogen, water, carbon monoxide, and carbon dioxide. The reactions are summarized below [Higman2014]:

- Partial oxidation:

$$C + \tfrac{1}{2} O_2 \rightarrow CO \tag{2.24}$$

- CO oxidation:

$$CO + \tfrac{1}{2} O_2 \rightarrow CO_2 \tag{2.25}$$

- Water gas reaction:

$$C + H_2O \rightleftarrows CO + H_2 \tag{2.26}$$

- Boudouard reaction:

$$C + CO_2 \rightleftarrows 2CO \tag{2.27}$$

This gas composition (CO, CO_2, H_2, O_2, etc.), as discussed in Section 2.5.4 and 2.6, may all be detectable using an ultrabroadband CARS configuration. As a nonintrusive optical method, this technique has great potential to implement in-situ investigations, which is a powerful tool when combined with DTF and TGA for gasification diagnostics.

Nevertheless, this thesis focuses mainly on coal gasification in pure CO_2 atmosphere. Therefore, only the Boudouard reaction should take place, which is highly endothermic and its equilibrium lies far to the left side of the Equation (2.27) [Bell2011, Hunt2013, Lahijani2015]. Typically, at temperatures $\gtrsim$973 K, the reaction starts to simultaneously proceed towards the CO direction [Hunt2013]. In this regard, the energy conversion process can be investigated by monitoring the temperature and the CO concentration. In industrial applications, gasification processes are typically performed in gasifiers, with coal particles

fed into the reactor when high temperatures are reached. The CO concentration generated from a single coal particle (~3 mm diameter) in the Boudouard reaction was reported to be low ($\lesssim$ 2% at 1123 K) [An2021]. Therefore, high sensitivity is required for the measurements.

3 Theory and simulation model of ultrabroadband CARS

In this chapter, both the theory and model for extracting the temperature and concentration based on ultrabroadband CARS spectroscopy are described in detail. In Section 3.1, starting from the wave equation, the basic CARS theory is introduced and the expression for the CARS signal strength is deduced. Section 3.2 discusses the modeling of ultrabroadband CARS. The intrinsic basics of extracting Raman excitation efficiencies from the ultrabroadband pump/Stokes spectrum for different molecules are discussed. Based on this, the methods of temperature and concentration determination by optimizing several parameters for spectral fitting are explained. In Section 3.3, minor species concentration determination from the modulation dips of the nonresonant background is discussed.

3.1 CARS signal intensity

CARS, as described in Section 2.2, is generated as a result of the polarization induced by the electric field of pump, Stokes and probe beams. Here we start from the wave equation [Boyd2008] and assume that the electric field has a time dependence in the form of $\exp(i\omega t)$. Then the wave equation at the frequency of the CARS signal (ω_{CARS}) can be expressed as

$$\nabla^2 E\left(\omega_{CARS},\vec{r}\right)+\frac{\omega_{CARS}^2}{c^2}E\left(\omega_{CARS},\vec{r}\right)=-\mu_0\omega_{CARS}^2 P\left(\omega_{CARS},\vec{r}\right), \tag{3.1}$$

where μ_0 is the permeability of vacuum and $P\left(\omega_{CARS},\vec{r}\right)$ is the induced polarization for the CARS signal. For an isotropic gas medium, the polarization may be expressed as [Boyd2008]

$$\begin{aligned} P\left(\omega_{CARS},\vec{r}\right) &= P^{(1)}\left(\omega_{CARS},\vec{r}\right)+P^{(3)}\left(\omega_{CARS},\vec{r}\right) \\ &= \varepsilon_0\chi^{(1)}E(\omega_{CARS},\vec{r})+P^{(3)}\left(\omega_{CARS},\vec{r}\right) \end{aligned}, \tag{3.2}$$

with ε_0 to be the permittivity of free space and $\chi^{(1)}$ to be the linear susceptibility.

Substituting Equation (3.2) into Equation (3.1) and considering the relation $\varepsilon/\varepsilon_0 = 1+\chi^{(1)}$, the following expression is obtained

$$\nabla^2 E\left(\omega_{CARS},\vec{r}\right)+\frac{\omega_{CARS}^2}{c^2}\frac{\varepsilon}{\varepsilon_0}E\left(\omega_{CARS},\vec{r}\right)=-\mu_0\omega_{CARS}^2P^{(3)}\left(\omega_{CARS},\vec{r}\right), \tag{3.3}$$

The most general form of $P^{(3)}\left(\omega_{CARS},\vec{r}\right)$ may be expressed as [Eckbreth1996, Boyd2008]

$$P_i^{(3)}\left(\omega_{CARS},\vec{r}\right)=\varepsilon_0\chi_{ijkl}^{(3)}\left(\omega_{CARS},\omega_p,\omega_{St},\omega_{pr}\right)E_j\left(\omega_p,\vec{r}\right)E_k\left(\omega_{St},\vec{r}\right)E_l\left(\omega_{pr},\vec{r}\right). \tag{3.4}$$

Here, $\chi_{ijkl}^{(3)}$ is the third-order susceptibility of the molecule. *i*, *j*, *k* and *l* are the polarization subscripts for CARS, pump, Stokes and the probe fields. ω_p, ω_{St}, and ω_{pr} represent the frequency of the pump, Stokes and the probe signal, respectively.

Assuming the electric fields of the pump, Stokes and the probe pulses to be plane waves, we can substitute the nonlinear polarization shown in Equation (3.4) into Equation (3.3) and obtain the following expression [Eckbreth1996]

$$\begin{aligned} &\nabla^2 E\left(\omega_{CARS},\vec{r}\right)+\frac{\omega_{CARS}^2}{c^2}\frac{\varepsilon}{\varepsilon_0}E\left(\omega_{CARS},\vec{r}\right) \\ &\quad=-\frac{\omega_{CARS}^2}{c^2}\chi_{ijkl}^{(3)}E\left(\omega_p\right)E^*\left(\omega_{St}\right)E\left(\omega_{pr}\right)exp\left[\, i\left(\overrightarrow{k_p}-\overrightarrow{k_{St}}+\overrightarrow{k_{pr}}\right)\cdot\ \vec{r}\,\right] \end{aligned}, \tag{3.5}$$

where $c^2 = 1/\left(\varepsilon_0\mu_0\right)$. From Equation (3.5), it can be seen that the CARS electric field only experiences significant enhancement along the direction of $\overrightarrow{k_{CARS}}=\overrightarrow{k_p}-\overrightarrow{k_{St}}+\overrightarrow{k_{pr}}$ or when the phase mismatch $\Delta\vec{k}=\overrightarrow{k_p}-\overrightarrow{k_{St}}+\overrightarrow{k_{pr}}-\overrightarrow{k_{CARS}}$ is small. As shown in Fig. 2.6 (a), this is termed the phase-matching condition.

Assuming that the CARS electric field $E\left(\omega_{CARS},\vec{r}\right)$ does not vary very quickly (slowly varying wave assumption), the second derivative in Equation (3.5) may be neglected [Eckbreth1996]. Considering the propagation of the electric field along z axis, the integration over z from zero to *l* yields the following expression

$$E\left(\omega_{CARS},l\right)=\frac{\omega_{CARS}}{2nc}\chi_{ijkl}^{(3)}E\left(\omega_p\right)E^*\left(\omega_{St}\right)E\left(\omega_{pr}\right)\frac{\exp(i\Delta kl)-1}{i\Delta k}. \tag{3.6}$$

Based on the relation $I = \frac{nc\varepsilon_0}{2}|E|^2$, the CARS intensity may then be expressed as

$$I_{CARS} = \frac{\omega_{CARS}^2}{n^4 c^4 \varepsilon_0^2} \left|\chi_{ijkl}^{(3)}\right|^2 I_p I_{St} I_{pr} l^2 \mathrm{sinc}^2\left(\frac{\Delta kl}{2}\right). \tag{3.7}$$

From Equation (3.7), it is obvious that the CARS intensity is proportional to the product of the pump, Stokes and the probe intensities. In addition, a longer interaction length (l) also contributes to a larger CARS intensity. The temperature and Raman transitions from different gas species are encoded in $\chi_{ijkl}^{(3)}$, which includes a Raman resonant term $\chi_R^{(3)}$ and a nonresonant contribution $\chi_{NR}^{(3)}$ [Nibler1979, Eckbreth1996]:

$$\chi_{ijkl}^{(3)}(\Omega) = \sum_n \chi_R^{(3)} + \chi_{NR}^{(3)} = \sum_n \frac{K_n}{2(\omega_n - \Omega) - i\Gamma_n} + \chi_{NR}^{(3)}. \tag{3.8}$$

Here, ω_n is the angular transition frequency for the Raman transition n and Γ_n is the Raman linewidth. K_n represents the transition amplitude, which is linearly proportional to the molecular population difference ΔN_n and the Raman cross section $\left(\frac{\partial\sigma}{\partial\Omega}\right)_n$ [Yuratich1977, Eckbreth1996]:

$$K_n \sim \frac{(4\pi)^2 \varepsilon_0 c^4}{\hbar \omega_p \omega_{St}^3} \Delta N_n \left(\frac{\partial\sigma}{\partial\Omega}\right)_n. \tag{3.9}$$

As shown in Equation (3.8), when the frequency difference of the pump and Stokes fields ($\Omega = \omega_p - \omega_{St}$) coincides with a certain Raman resonance ω_n, the CARS susceptibility is significantly enhanced. The nonresonant susceptibility is in general small resulting in an overall background of the entire CARS signal [Eckbreth1996].

3.2 Model of the ultrabroadband CARS

The previous section explained the CARS signal strength and its relation with the transition frequency, molecular population difference and the Raman cross section. As has been demonstrated for ultrabroadband CARS, the CARS signal can be (1) free from collisional effects up to 50 bar [Wrzesinski2013] and (2) the nonresonant contribution, which disturbs the overall signal, can be largely suppressed when the probe pulse has a delay of a few ps [Miller2010]. Both advantages greatly simplify the modeling for temperature and concentration determination from CARS measurements. According to Lucht et al. and

Richardson et al. [Lucht2006, Richardson2011], the CARS signal in time domain may be modeled as the product of the probe pulse with the resonant and nonresonant responses of the medium. Then one may write

$$E_{CARS}(t) = E_{pr}(t)[P_R(t) + P_{NR}(t)]. \tag{3.10}$$

The nonresonant response can be given by

$$P_{NR}(t) = \alpha E_p(t) E_{St}(t), \tag{3.11}$$

and the resonant response is expressed as

$$P_R(t) = \beta\left[\int_{-\infty}^{t} E_p(t') E_{St}(t') dt'\right]\left\{\sum_n \Delta N_n \left(\frac{d\sigma}{d\Omega}\right)_n (\cos\omega_n t) e^{-\Gamma_n t}\right\}. \tag{3.12}$$

Here, α and β are scaling factors. β is related to the number density of the medium and the excitation efficiency determined from the pump/Stokes pulses. ΔN_n is the molecular population difference, ω_n and $(d\sigma/d\Omega)_n$ are the angular frequency and the Raman cross section for Raman transition n. The integration term $\int_{-\infty}^{t} E_p(t') E_{St}(t') dt'$ grows to a constant soon after the ultrashort excitation (~7 fs) from the pump and Stokes fields. This constant relates to the area underneath the intensity envelop of the pump/Stokes pulse.

The exponential term in Equation (3.12) describes the decay due to collisions with a rate constant of Γ_n. If we take N_2 as an example, the collisional linewidth $\Gamma_n/\pi c$ at atmospheric pressure and temperature is ~0.1 cm^{-1} [Lucht2006]. Therefore, the characteristic collisional dephasing time τ_n (=$1/\Gamma_n$) for N_2 is ~106 ps. Under high-pressure environments, stronger collisions are expected. Nevertheless, several previous publications have proven that probe delays within a few ps are free from collisional dephasing effects at pressures up to 50 bar [Lucht2006, Wrzesinski2013]. Therefore, the collisional dephasing effects are neglected for a probe delay within a few ps in this thesis.

Thus, the model for resonant molecular response can be simplified to

$$P_R(t) \propto \beta \cdot \sum_n \Delta N_n \left(\frac{d\sigma}{d\Omega}\right)_n (\cos\omega_n t). \tag{3.13}$$

In addition, the nonresonant contribution expressed from Equations (3.10) and (3.11) can only appear when the pump, Stokes and probe fields are temporally overlapped (Fig. 2.7). It is neglected because the CARS spectra used for diagnostics are at the probe delays where the nonresonant contribution is largely reduced.

In this regard, by substituting the resonant polarization $P_R(t)$ (Equation (3.13)) into Equation (3.10) and neglecting the nonresonant contribution $P_{NR}(t)$, we can then apply the following Fourier transform of the CARS signal in time domain to obtain the CARS spectrum:

$$S_{CARS}(\omega) = \left| \int_{-\infty}^{\infty} E_{CARS}(t) e^{-i\omega t} dt \right|^2 . \tag{3.14}$$

When a CARS spectrum is not sufficient to extract diagnostic information or it is lack of sufficient spectral resolution, the time-resolved analysis of the CARS signal may be used for diagnostics. As discussed in Section 2.2, after the presence of the pump/Stokes pulse, the generated Raman coherence starts to decay. This decay originates from the dephasing of the oscillations of the numerous rovibrational transitions at slightly different frequencies, which are reflected from the sum of the $\cos(\omega_n t)$ in $P_R(t)$ (Equation (3.13)). The initial dephasing rate is temperature sensitive [Lucht2006, Roy2008] and the corresponding time-resolved CARS signal can be described as [Lucht2006]:

$$S_{CARS}(\tau) = \int_{-\infty}^{+\infty} I_{pr}(t-\tau)[P_R(t) + P_{NR}(t)]^2 dt , \tag{3.15}$$

where $I_{pr}(t-\tau)$ is the probe pulse intensity. τ is the temporal delay between the probe and the pump/Stokes pulses. In this thesis, the spectral resolution (~10 cm^{-1}, see Fig. 4.2 (b)) is not sufficient to resolve the fundamental ($\upsilon = 1 \rightarrow \upsilon = 0$) rovibrational structure of N_2 at temperatures <1000 K. Therefore, when extracting temperature from N_2, least square fitting is implemented between the experimental integrated N_2 CARS signals at different delays with the calculated signals from Equation (3.15).

Although the nonresonant signal is undesirable during CARS measurements, it does encode some valuable information in diagnostics. For example, in nanosecond CARS, the nonresonant signal may be measured simultaneously with the resonant one through polarization techniques to correct for pulse-to-pulse temporal and spatial variations of the laser pulses [Farrow1985]. However, due to the significant resonant signal loss from this technique, it was reported to be not feasible for broadband implementation [Farrow1985]. Nevertheless, separate nonresonant measurements have been used to retrieve the excitation efficiencies (included in β) from the ultrabroadband pulses [Bohlin2017]. The following parts explain briefly how the excitation efficiencies may be determined from the nonresonant signal.

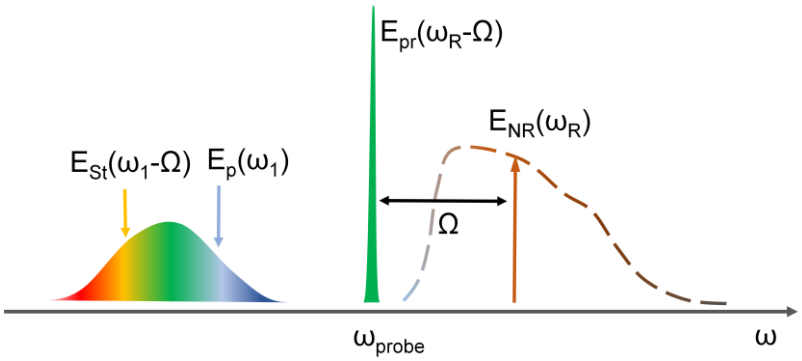

Fig. 3.1 Scheme for the determination of the excitation efficiency for a particular Raman shift. E_p, E_{St}, E_{pr} are the electric fields of the pump, Stokes and probe pulse, respectively. ω_R is the angular frequency at the spectral position of the Raman shift of the molecule. Ω and ω_1 are the integration variables according to Equation (3.16).

The nonresonant contribution in frequency domain is expressed as [Meshulach1999, Oron2002a]

$$E_{NR}(\omega)=\int_0^\infty d\Omega E_{pr}(\omega-\Omega)\int_0^\infty d\omega_1 E_{St}^*(\omega_1-\Omega)E_p(\omega_1). \tag{3.16}$$

The second integration $\int_0^\infty d\omega_1 E_{St}^*(\omega_1-\Omega)E_p(\omega_1)$ is indeed the excitation efficiency from the ultrabroadband pulse. It can be interpreted as the sum of all the pump and Stokes pairs within the excitation bandwidth having a frequency spacing of Ω. According to Equation (3.16), the nonresonant CARS signal is the result of a convolution between the probe electric field and the excitation efficiency. Therefore, as shown in Fig. 3.1, the excitation efficiency may be estimated from the nonresonant signal at ω_R of the corresponding Raman signal ($\propto E_{NR}^2(\omega_R)$). For instance, when the probe spectrum $E_{pr}(\omega_R-\Omega)$ is centered at $\lambda_{pr}\cong$516 nm, the nonresonant contribution $E_{NR}(\omega_R)$ at $\lambda_R\cong$461 nm (λ_R is the wavelength corresponds to the frequency of ω_R) gets the contribution for $\Omega\sim$ 2330 cm^{-1} only, thus, from the pump and Stokes pairs with a spectral distance of $\Omega\sim$ 2330 cm^{-1} (for N_2). This estimation relies on the fact that the spectral width of the probe (~10 cm^{-1}) is much smaller compared to the spectrum of the pump/Stokes pulse (~6000 cm^{-1}).

In this regard, the scaling factor β in Equation (3.13) maybe replaced by the product of the scaling factor β_i for gas species i and the excitation efficiency determined from the nonresonant signal. Then the quantitative concentration measurements can be implemented using the following expression

$$P_R(t) \propto \sum_i \beta_i \sqrt{S_{NR}(\omega_i)_{measured}} \cdot \sum_n \Delta N_{i,n} \left(\frac{d\sigma}{d\Omega} \right)_{i,n} (\cos \omega_{i,n} t), \tag{3.17}$$

where $S_{NR}(\omega_i)_{measured}$ is the measured nonresonant spectrum at zero delay and the spectral position of ω_i (ω_i corresponds to the frequency where the Raman signal for gas species i appears). In this thesis, the $\sqrt{S_{NR}}$ is termed as the nonresonant response and is usually measured in pure argon for spectral referencing.

To implement temperature and concentration measurements, the simulated CARS spectra are compared with the experimental ones. The probe beam is assumed to have no temporal chirp because the pulse duration is much larger compared to the pump/Stokes beam. Its influence is therefore neglected. Then the simulated ultrabroadband CARS spectra are fit with the background corrected experimental ones by optimizing the following four parameters:

1. Probe pulse duration $\Delta\tau_{pr}$
2. Temperature T
3. Spectral shifter S_{shift} for optimizing the overlap between the simulated and experimental CARS spectra
4. The scaling factors β_i for different i species

Despite the fact that the probe pulse duration can be measured using e.g. an autocorrelator, it is implemented here as an optimization parameter. The reason is that the CARS spectral resolution depends on the probe pulse duration. Therefore, even small uncertainties of the probe duration lead to mismatch of the simulated and experimental spectra, thus need to be corrected to be able to retrieve the actual measured CARS spectrum.

The optimization is performed with MATLAB using the in-built genetic algorithm. If only temperature measurements are performed, the first three parameters are optimized. The 4th parameter is added only for concentration measurements. Depending on how many gas species are expected, the parameters that need to be optimized will increase (e.g. β_1, β_2, β_3…).

3.3 Minor species concentration determination

The previous section discussed the temperature and concentration determination provided that the nonresonant contribution is sufficiently reduced using proper probe delays.

However, when the probing species is minor, the CARS signal (e.g. N_2 and CO) can easily disappear due to the Raman coherence dephasing. In this case, the CARS signals at small probe delays with both resonant and nonresonant contributions have to be utilized for diagnostics, which is especially important for monitoring CO during coal gasification (see Section 2.7). Therefore, this section discusses concentration determination for minor species from the modulation dip of the CARS spectrum, which follows several previous publications [Hahn1993, Eckbreth1996].

The CARS susceptibility expression given in Equation (3.8) shows that the resonant susceptibility is complex and can be expressed with a real and an imaginary part:

$$\chi_{ijkl}^{(3)} = \sum_n \left(\chi' + i\chi''\right)_n + \chi_{NR}^{(3)} . \tag{3.18}$$

According to the modulus square dependence of the CARS spectrum on the CARS susceptibility (Equation (3.7)), the CARS signal will follow the expression [Eckbreth1981]

$$\left|\chi_{ijkl}^{(3)}\right|^2 = (\sum_n \chi'_n)^2 + (\sum_n \chi''_n)^2 + 2\chi_{NR}\sum_n \chi'_n + \left(\chi_{NR}^{(3)}\right)^2 . \tag{3.19}$$

If we consider that the species of interest has only a low concentration ($\chi', \chi'' \le \chi_{NR}$), the expression can be simplified as

$$\left|\chi_{ijkl}^{(3)}\right|^2 = \left(\chi_{NR}^{(3)}\right)^2 + 2\chi_{NR}\sum_n \chi'_n , \tag{3.20}$$

where the real part of the resonant susceptibility χ'_n is given by

$$\chi'_n = K_n \frac{2\Delta\omega_n}{4\Delta\omega_n^2 + \Gamma_n^2} , \tag{3.21}$$

with the detuning from the Raman resonance $\Delta\omega_n$ expressed as $\Delta\omega_n = \omega_n - \left(\omega_p - \omega_{St}\right)$ and K_n as the amplitude for the Raman transition n that are introduced in Section 3.1.

According to Equations (3.20) and (3.21), it is evident that far from the Raman resonance the CARS spectrum exhibits no spectral feature and is proportional to $\left(\chi_{NR}^{(3)}\right)^2$. When the detuning $\Delta\omega_n$ is positive, the CARS signal rises above the nonresonant background. For negative detuning $\Delta\omega_n$, the CARS signal subtracts from the nonresonant background because the second term on the right side in Equation (3.20) is negative. Therefore, the CARS spectrum close to the resonance exhibits a modulation on the nonresonant background, showing a dispersive behavior from the real part of the resonant susceptibility χ'_n. This spectral feature can be observed in the CO CARS spectra as shown in Fig. 6.5 and in Chapter 7.

When the concentration measurements are considered, Equation (3.20) can be rewritten as [Eckbreth1996]

$$\left|\chi_{ijkl}^{(3)}\right|^2 = \left(\chi_{NR}^{(3)}\right)^2 \left(1 + \frac{2N}{\chi_{NR}^{(3)}} \sum_n \overline{\chi'_n} \right), \tag{3.22}$$

where $\overline{\chi'_n}$ is the real part of the resonant susceptibility per molecule and N is the number density of the resonant species. Equation (3.22) shows that after the CARS spectrum of the interested minor species is normalized to the nonresonant background, the modulation dip originating from second term in Equation (3.22) is related to the species concentration. However, the accuracy of the concentration measurements based on this is limited to the degree to which the background nonresonant susceptibility is known.

For coal gasification investigations, we focus on the CO concentration determination at ~1.4 bar (see Chapter 7). The Raman linewidth Γ_n of CO is assumed to be 0.09 cm^{-1} based on the work of [Rosasco1989] at atmospheric pressure. As a pure CO_2 atmosphere is chosen (Section 2.7), the nonresonant background close to the frequencies of the CO resonance mainly originates from CO_2. The nonresonant susceptibility $\chi_{NR}^{(3)}$ of CO_2 is taken from Hahn et al. [Hahn1995] to be 12.02×10^{-18} $cm^3/(erg\cdot amagat)$. Note that it has to be multiplied by 1.40×10^{-8} [Boyd2008] to convert it from Gaussian to SI units (m^2/V^2) to fit all parameter units used for the resonant susceptibility calculations. Correspondingly, the CO volume concentration σ in pure CO_2 atmosphere is calculated from

$$\sigma = \frac{V_{CO}}{V_{CO} + V_{CO_2}}, \tag{3.23}$$

where V_{CO} and V_{CO_2} is the volume for CO and CO_2, which can be expressed as

$$V_{CO} = \frac{N_{CO} \cdot V_T}{N_A} \cdot V_m, \qquad V_{CO_2} = \frac{N_{CO_2} \cdot V_T}{N_A} \cdot V_m, \tag{3.24}$$

where N_{CO} and N_{CO_2} are the number density for CO and CO_2, V_T is the total volume. N_A is the Avogadro number and V_m is the molar volume. V_m is temperature (T) and pressure (P) dependent and, assuming an ideal gas condition, can be expressed by

$$V_m = RT/P, \tag{3.25}$$

here $R\cong8.205737\times10^{-5}$ $m^3\cdot atm\cdot K^{-1}\cdot mol^{-1}$ is the gas constant.

Substituting Equation (3.24) into Equation (3.23), the relation between CO concentration and number densities of CO and CO_2 is obtained

$$\sigma = \frac{N_{CO}}{N_{CO} + N_{CO_2}}. \tag{3.26}$$

Combining Equation (3.26) with (3.22), the modulation dip of the CO_2 nonresonant background as a function of the CO concentration can be calculated. The results obtained with this method are discussed in Section 7.1.2.

4 Experimental setup for two-beam ultrabroadband CARS measurements

In this chapter, the experimental approach for the two-beam ultrabroadband CARS measurements is discussed in detail. Section 4.1 presents the experimental setup and characterizes the laser source. Section 4.2 shows the analysis of the shot-to-shot spectral stability of the pump/Stokes beam, which provides the precondition for practical and accurate concentration measurements. In Section 4.3, the high-temperature and high-pressure gas oven is shown and the methods of its temperature and concentration control for the reaction gases are illustrated. In addition, the optical arrangements for gasification measurements are explained.

4.1 200 kHz dual-output OPCPA based optical system

Our two-beam ultrabroadband fs/ps CARS setup is based on a dual-output, 200 kHz optical parametric chirped pulse amplification system (venteon OPCPA, Laser Quantum GmbH, Konstanz, Germany). The OPCPA is seeded by a Ti:Sapphire oscillator amplified in two BBO-based non-collinear parametric amplification (NOPA) stages. This provides an ultrabroadband (~650-1100 nm) output of a ~7 fs pulse acting as both pump and Stokes beam to generate the molecular Raman coherences. In addition, the output of the Ti:Sapphire oscillator at ~1032 nm is directed into a photonic-crystal fiber (PCF) rod-type amplifier and then frequency doubled to ~516 nm to provide an additional narrow band output with ~2 ps pulse duration acting as the probe. The pump/Stokes and the probe pulse energy are typically 10 μJ and 0.8 μJ, respectively. Both beams are spatially overlapped using a longpass dichroic mirror (LPDM1, DMLP550-Ø1, Thorlabs) to achieve collinear phase matching. The experimental diagram is shown in Fig. 4.1. The temporal overlap between the two beams is adjusted using a motorized delay stage in steps of 100 fs in the

probe beam path. Both beams are adjusted to have the same linear polarization for sufficient CARS signal generation [Vestin2007a, Bohlin2014b]. Afterwards, the two beams are focused into a gas oven by a concave mirror (f = 500 mm, CM750-500-P01,Thorlabs). In front of the concave mirror, the diameters of the pump/Stokes beam and the probe beam are measured to be ~5 mm and ~4 mm by means of a beam profile camera (LaserCam-HR, Coherent Inc., USA). Assuming Gaussian beams, the probe volume is then estimated to be ~80 µm in diameter and ~20 mm in length.

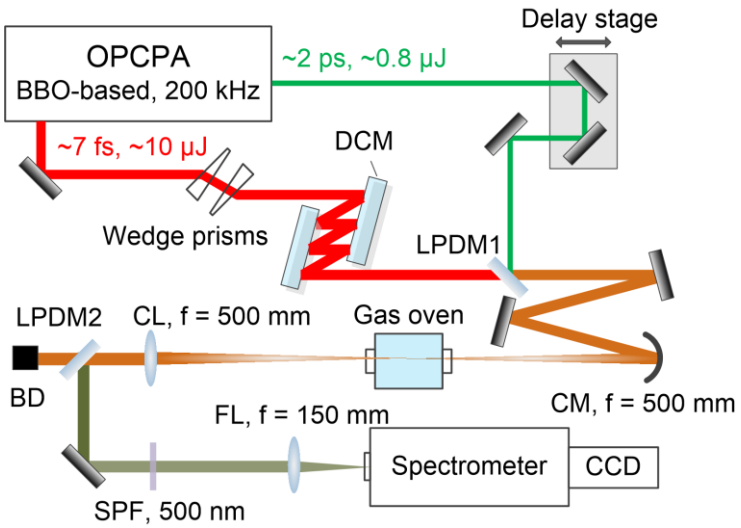

Fig. 4.1 Experimental layout of the two-beam ultrabroadband CARS. DCM: double-chirped mirrors; LPDM: long pass dichroic mirror; CM: concave mirror (f = 500 mm); CL: collimating lens; BD: beam dump; SPF: short pass filter (cutoff wavelength = 500 nm); FL: focusing lens (f = 150 mm).

The gas oven has four optical sapphire windows with a thickness of 14 mm and a clear aperture of 28 mm [Küster2017]. As the sapphire window of the gas oven induces large positive dispersion to the ultrashort pump/Stokes pulses, an additional pair of double-chirped mirrors (DCM11, Laser Quantum GmbH, Germany) is installed at the exit of the ~7 fs beam to pre-compensate the dispersion from the sapphire window. In addition, a pair of wedges made of fused silica is used for fine tuning of the dispersion. The wedges are placed with a Brewster angle towards the beam for the best transmission. After transmission through the oven, the beams are collimated using a lens with 500 mm focal length. They are then passing through another long pass dichroic mirror (LPDM2, DMLP505-Ø1, Thorlabs) and a short pass filter (SPF) to attenuate the residual pump/Stokes and probe pulses and optimize the signal-to-noise ratio of the CARS signals. A 150 mm focal lens is used to focus the filtered CARS signal into a spectrometer (Shamrock 500i, Oxford Instruments,

Abingdon, UK) with 500 mm focal length. The spectrometer is equipped with a 1200 line/mm grating and a 300 line/mm one, having a maximum instrument resolution of 0.06 nm at 500 nm.

The CARS spectra are acquired using a cooled 2048×512 pixel CCD camera (Newton CCD DU940P-BV, Andor Technology Ltd, UK) attached to the spectrometer. The pixel size is 13.5 µm × 13.5 µm with a 100% fill factor and the thermo-electric (TE) cooling to -100 °C is utilized to reduce detector noise. The acquisition time is set to 50 ms. Typically, 20-50 accumulations are acquired during the measurements for better signal to noise ratios (SNRs).

In order to characterize the sub-10 fs beam of the ultrabroadband fs/ps CARS setup, a 2% beam splitter is used to reflect a small portion of the pump/Stokes beam to an autocorrelator (Femtometer, Newport Corporation, Irvine, USA). The same sapphire window is installed in front of the autocorrelator to ensure the same condition as in the oven. Fig. 4.2 (a) shows the measured fringe resolved autocorrelation (FRAC) signal of the pump/Stokes pulse. The pulse duration is calculated by [Femtometer2008]

$$T_p = \frac{N \cdot (\lambda_0 / c_0)}{B}, \tag{4.1}$$

where N is the number of fringes within the full width half maximum (FWHM) range, λ_0 is the spectral center wavelength, c_0 is the speed of light in vacuum, and B is the deconvolution factor. Assuming a sech^2 pulse shape (B = 1.9) and taking the typical center wavelength of ~800 nm into account, the pulse duration is calculated to be ~9 fs.

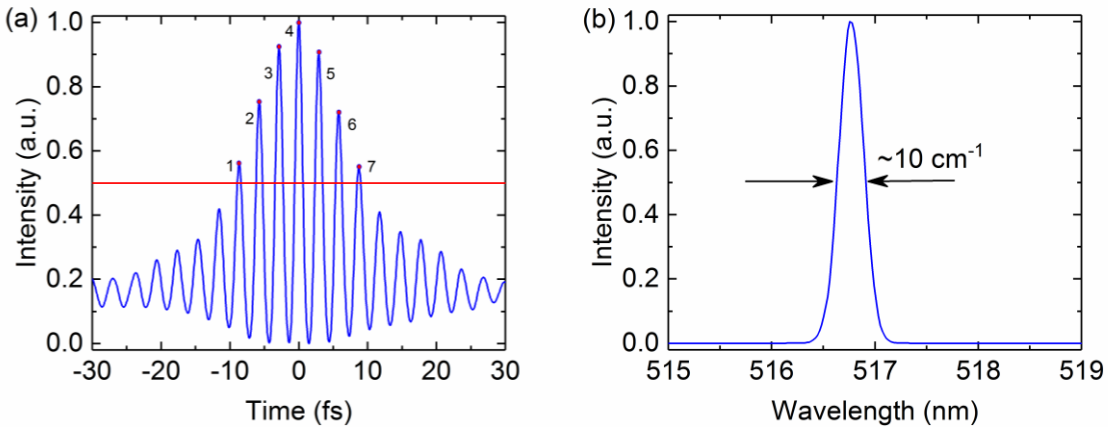

Fig. 4.2 (a) Typical pump/Stokes autocorrelation signal measured by fringe resolved autocorrelation. The pulse duration is then calculated to be ~9 fs. The red line shows the 50% level of the maximum signal intensity. The fringes, which lie within the FWHM range, are marked with red dots at the peak of each fringe. (b) Typical probe spectrum with a spectral width of ~10 cm^{-1}.

The probe pulse duration was measured with another autocorrelator (pulseCheck, APE, Berlin, Germany) to be ~2.2 ps. Its corresponding narrowband spectrum is shown in Fig. 4.2 (b), with the full width at half maximum (FWHM) bandwidth to be ~10 cm^{-1}. This provides sufficient spectral resolution for vibrational CARS measurements. The temporal resolution of the probe pulse delay scan was examined by performing measurements in pure argon. Since argon is not Raman active, only the nonresonant signal appears when the pump/Stokes and the probe pulse have temporal overlap. The argon nonresonant signals integrated over the whole spectral range are shown in Fig. 4.3 for different delays. The temporal resolution of the probe scan is therefore estimated as the FWHM of the signal envelope to be ~1 ps. In addition, the zero delay can be determined at the position where the nonresonant signal is maximal.

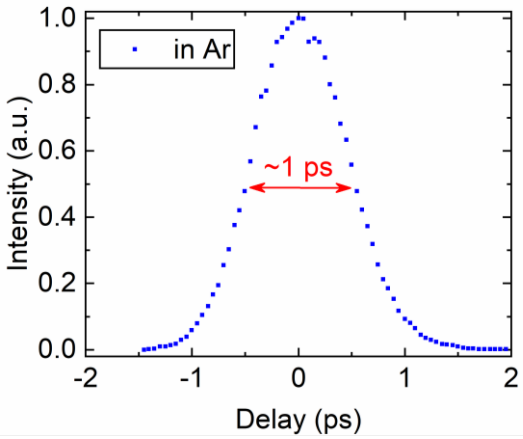

Fig. 4.3 Integrated nonresonant signal as a function of the probe delay in pure argon at 1.7 bar. The probe delay scan is implemented in steps of 100 fs.

The pointing stability of the pump/Stokes beam together with the probe beam was also determined at the position of the spectrometer using a camera. This camera is from a commercial laser beam steering correction system (GuideStar, Newport), which permits the beam position data acquisitions. The deviations of the beam position in horizontal and perpendicular directions were within ~40 µm and ~30 µm respectively from measurements over 5 minutes with a time interval of ~500 ms.

4.2 Shot-to-shot pump/Stokes spectral stability

The stability of the pump/Stokes spectrum is crucial for reliable concentration or temperature measurements. Often, the ultrabroadband spectrum for CARS measurement is

generated from self-phase modulation (SPM) of high-energy laser pulses in a hollow fiber filled with noble gases (Ar, Ne, He, etc.) [Roy2009b, Roy2010b, Bohlin2014b]. The ultrabroadband spectra generated via this method have been studied in detail in the perspective of spectral stability, required pulse energy and waveguide diameter, impaired gas purity influence, etc. Weichert *et al.* investigated the spectral broadening of the 25 fs, 10 Hz laser pulses via SPM in a Neon filled hollow core fiber with 250 µm fiber core diameter [Weichert2016]. The stability of the broadened spectrum shows strong dependence on the input energy and the applied pressure. Using an input energy of 2 mJ and a pressure of 1.2 bar, the group generated sub-10 fs pulses with a spectral range of ~600-950 nm resulting in a rms (definition, see Equation (4.2)) fluctuation of ~20%. Böhle *et al*. carried out the spectral broadening for a 8 mJ, 1 kHz, 23 fs Ti:sapphire chirped pulse amplification (CPA) system in a 2 m, 450 µm hollow fiber filled with 1.8 bar He. The rms fluctuations were found to be 7.8% for linearly polarized laser light [Böhle2014]. However, spectra with this amount of fluctuations may impair the accuracy and precision for CARS measurements. To compare the spectral stability with our pump/Stokes pulses, the ultrabroadband output from the OPCPA system was investigated in detail.

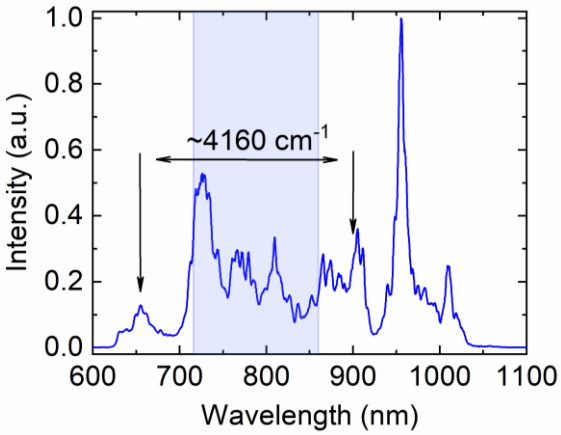

Fig. 4.4 Typical pump/Stokes spectrum integrated over 32 ms. The blue shadow part indicates the spectral region where Fig. 4.5 (b) is recorded.

A typical pump/Stokes spectrum of our laser system is shown in Fig. 4.4. This spectrum was measured using a spectrometer (AvaSpec-ULSi3648, AVANTES, Netherlands) with an integration time of 32 ms, i.e. integrating over 6400 pulses. According to Fig. 4.4, the pump/Stokes spectrum spans from ~650 nm to ~1015 nm at tenth of its maximum height (FWTM ~ 5555 cm^{-1}), which is broad enough to provide the pump and Stokes pairs for the most relevant combustion species, including H_2 (~4160 cm^{-1}). In order to observe the shot-

to-shot stability of the 200 kHz sub-10 fs pump/Stokes spectrum, a camera with sufficiently fast response (e.g. acquisition time < µs scale) has to be utilized. The only available camera in our lab with this feature was a streak camera (OptoScope SC-10 system, Optronis, Kehl, Germany). It was therefore attached to a spectrometer (Acton SP2300i, Roper Industries Inc., Saratosa, USA) for recording the pump/Stokes spectra, as shown in Fig. 4.5 (a).

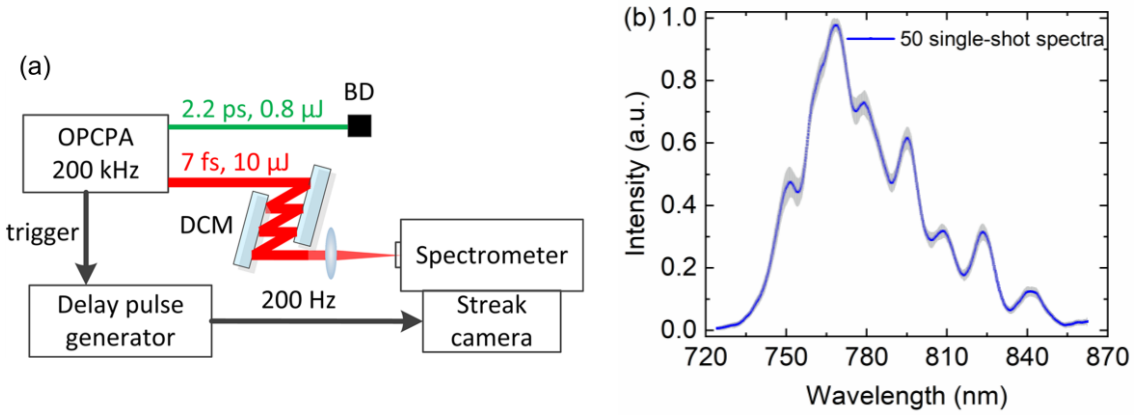

Fig. 4.5 (a) Setup for shot-to-shot pump/Stokes spectrum measurement. (b) Averaged 50 single-shot pump/Stokes spectrum centered at 800 nm. The grey shadow shows the standard deviation of the 50 single-shot spectra. The spectra are normalized to their maximum values in the measured spectral range.

A digital delay pulse generator (Model 9512 pulse generator, Quantum Composers Inc., Bozeman, USA) was used to select 1 out of 1000 trigger pulses from the 200 kHz OPCPA system to generate a trigger signal with a repetition rate of 200 Hz. In addition, the output was delayed by the pulse generator to synchronize the time window of the pump/Stokes pulse event and the streak camera recording. The sweep speed of the camera was set to 1 ns/mm resulting in a time window of 20 ns for a single-shot recording. To record only single events the readout time of the camera was set to 1 ms, i.e. shorter than the time interval between the 200 Hz trigger signals. The 300 line/mm grating of the spectrograph centered at 800 nm was chosen to measure the maximum spectral range for the single shot recordings. A tunable ps-laser system (Ekspla PL2231 with PG401, Ekspla, Vilnius, Lithuania) was used to calibrate the wavelength scale in the range from 740 nm to 860 nm. Fig. 4.5 (b) shows 50 normalized single-shot pump/Stokes spectra. The blue line shows the averaged spectrum from the 50 single-shot measurements, and the grey shadow shows the standard deviation at each wavelength. The remaining part of the pump/Stokes spectra shows a similar behavior. From Fig. 4.5 (b), good shot-to-shot stability of the pump/Stokes

spectra is displayed. The shot-to-shot rms spectral fluctuation is determined by using the spectral width for each shot from [Weichert2016]:

$$\sigma = \sqrt{\frac{\sum_\lambda S(\lambda) \cdot (\lambda - \lambda_c)^2}{\sum_\lambda S(\lambda)}}, \tag{4.2}$$

where S(λ) is the spectral intensity at each wavelength λ, λ_c is the center wavelength, which is determined as

$$\lambda_c = \frac{\sum_\lambda S(\lambda) \cdot \lambda}{\sum_\lambda S(\lambda)}. \tag{4.3}$$

The resulting shot-to-shot rms spectral fluctuations are ≤ 1.6%. Compared with the rms fluctuations (7.8%) from the Ti:Sa CPA seeded hollow core fiber broadened spectra [Böhle2014], the BBO-based ultrabroadband spectra show remarkable stability, as a precondition of reliable and accurate CARS measurements.

4.3 High-temperature/pressure gas oven

The schematic of the gas oven (MaxiCLAVE MP-HTIII with FlexiDOSE, TA Instruments Inc., New Castle, USA) with four sapphire windows having an offset of 90º is shown in Fig. 4.6. The premixed reaction gases flow into the gas oven perpendicular to the plane of the four optical windows. The interior of the reactor is made of ceramics, surrounded by a water-cooled steel pressure shell [Küster2017]. To protect the heating elements of the oven, the space between the ceramic tube and the steel shell is purged with argon at a fixed flow rate of 200 ml/min. The temperature inside the oven is controlled with a thermocouple (Type S) located close to the center of the oven (adjacent to the probe volume at a distance of ~5–10 mm).

The temperature and pressure can be set up to 1400 ºC and 35 bar. The gas flow rates are controlled by mass flow controllers (SLA5850, Brooks Instrument GmbH, Germany) with a maximum flow of 50, 100, 100, 333, and 600 ml/min for CO, H_2, CH_4, CO_2, and N_2, respectively. When the set flow is between 20% and 100% of its full scale, the gas flow accuracy is within 0.9% of the set gas flow and within 0.18% of the full scale when the set flow is below 20%. The gas concentrations are defined by the flow through the calibrated mass flow controllers for each species. Correspondingly, the accuracies of the controlled gas concentrations are determined by the accuracies of the flow rates controlled by the mass flow controllers.

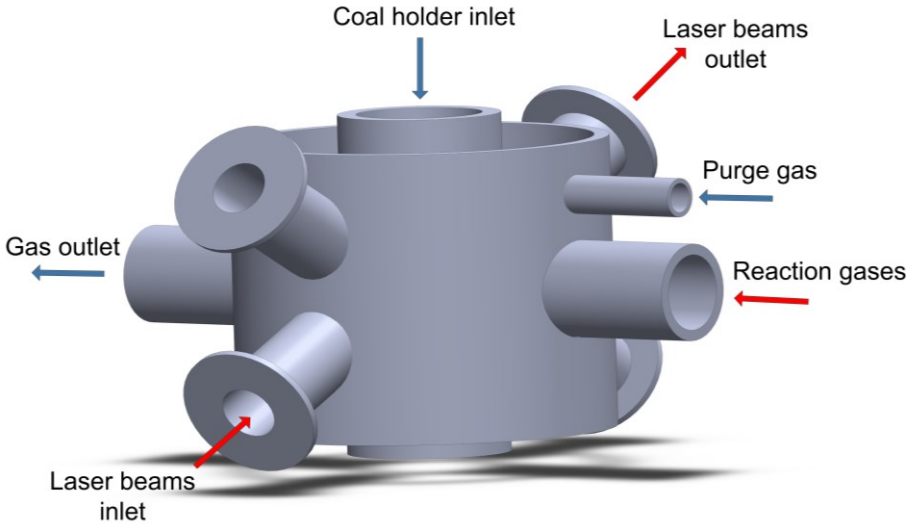

Fig. 4.6 Schematic of the gas oven.

Taken the N_2/CO_2 and CO/CO_2 gas mixtures as examples, Table. 4.1 shows the resulting set concentration accuracies according to the law of error propagation. In addition, the entire volume of the gas oven is determined by recording the time when using pure 200 ml/min argon to fill the oven from vacuum until it reaches 1 bar. The whole procedure takes around 48 minutes, yielding a total volume of ~9.6 L.

Table. 4.1 Examples of the concentration accuracies determined from the accuracies of the mass flow controllers according to the law of error propagation.

N_2 in CO_2 (%)	Reaction gas flow (ml/min)			Concentration accuracy (%)
	N_2	CO_2	Total flow	
30	105	245	350	±0.4
20	70	280		±0.3
10	35	315		±0.2
CO in CO_2 (%)	CO	CO_2	Total flow	
2.0	6.6	323.4	330	±0.2
0.5	1.6	328.4		±0.2

When implementing coal gasification measurements, a high temperature and pressure resistant sample holder is inserted from the top of the oven into its center. The configuration of the coal holder is shown in Fig. 4.7 as viewed from the laser beam output window. The vibration-free property of the coal holder is achieved with a combination of wire-fixation (black wire made of FeCrAl alloy) and a ceramic construction (white rod and the cylindrical coal crucible made of α-Al_2O_3) [Küster2017]. The crucible has an inner diameter of ~8 mm

and an internal depth of ~13 mm. The holder is proven to be temperature resistant up to 1673 K [Küster2017].

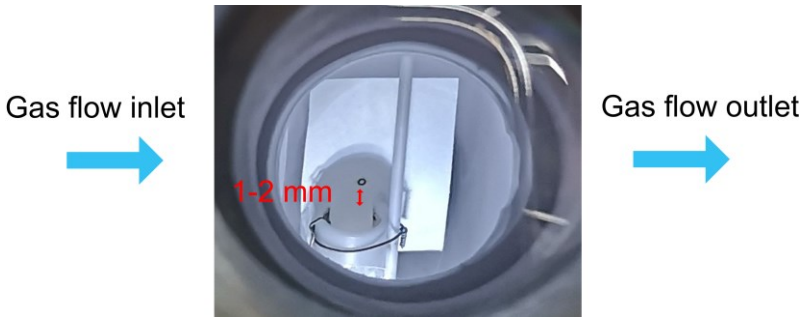

Fig. 4.7 Coal powder or particle holder construction in the gas oven. The view is taken from the laser beam output window. The hole burned into the paper shows the typical probing position.

Before the implementation of the coal gasification, as shown in Fig. 4.7, a piece of paper is attached to the center of the coal holder and then the holder is placed at the measurement position inside the oven. Then the two beams for the CARS measurement going through the oven burn a hole into the paper showing the current focus position. Based on this, the probing position can be adjusted and controlled. The typical probing position during the coal gasification measurements is shown in Fig. 4.7, where both beams focus on a position ~1-2 mm above the holder. In addition, as the controlled gas flow comes from the left side and goes out from the right side (according to the view shown in Fig. 4.7), the probing position is set to ~1 mm on the right side from the holder center. The thermocouple (Type S) is placed next to the coal holder for monitoring the oven temperature. After fixing the beam position, the crucible is filled with coal powder/particles and the oven is sealed. In this thesis, the feedstock of Central German lignite [Küster2017] is used. The lignite was pretreated in a pyrolysis process to generate lignite coke with higher carbon content. It was then dried and crushed to powder or particle (~2-3 mm diameter) form.

As discussed in Section 2.7, the Boudouard reaction typically starts to proceed towards CO formation at temperatures ≳973 K [Hunt2013]. Therefore, the heating ability of the oven is important for the investigation of the gasification process. For this reason, we investigated the heating ability and the heating rate of the oven at several different pressures. Fig. 4.8 (a) shows the temporal evolution of the oven temperatures during the heating process. The oven temperatures were measured using the Type S thermocouple. Fig. 4.8 (b) gives the heating rates at each temperature for different pressures, derived as the differentials of the curves shown in Fig. 4.8 (a).

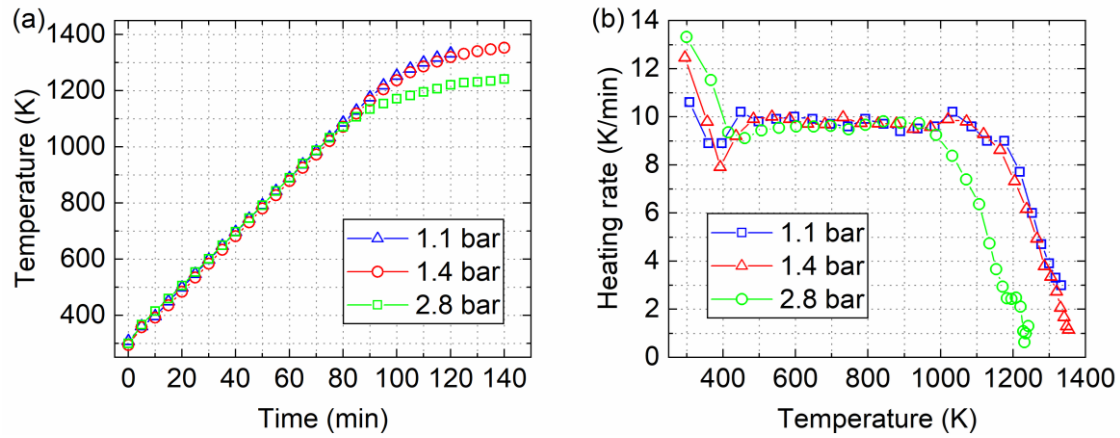

Fig. 4.8 (a) Temperature as a function of time during the oven heating process at 1.1 bar, 1.4 bar and 2.8 bar. The temperature that the oven is expected to achieve is set to ~1373 K. (b) Heating rate calculated from the differential of the temperature evolution with time.

Between 400 K and 500 K, a constant heating rate of 10 K/min is reached, which stays constant up to ~1000 K. Beyond this temperature, the heating rate drops significantly. At 2.8 bar, the maximum temperature that the system can reach is significantly lower than that for 1.4 bar. At ~1230 K, the heating rate has dropped to 1 K/min at 2.8 bar and it takes ~70 minutes to heat the oven from ~1000 K to this level. The heating rates at 1.1 bar and 1.4 bar are comparable. As a compromise, for gasification investigations, 1.4 bar is mainly considered in this thesis to ensure a sufficient molecular density as well as high temperatures (e.g. >1000 K). Correspondingly, the high temperature (e.g. >500 K) calibration measurements (with controlled gas flows) in Chapters 5 and 6 mainly focus on pressures below 2 bar.

5 Ultrabroadband CARS thermometry

This chapter is dedicated to temperature measurements using vibrational ultrabroadband CARS from multiple species, even simultaneously in a single measurement. This is quite challenging for other CARS techniques which usually require setups with two or more pump beams [Roy2003, Roy2004]. In Section 5.1, thermometry from CO_2 and H_2 is studied using single CARS spectra. In Section 5.2, thermometry from time-resolved N_2 CARS signals is investigated. Its measurement accuracy, precision, temporal resolution and suitable applications are discussed and compared to those of CO_2 and H_2. Special attention is drawn to the thermometry from vibrational CO_2 CARS which has not yet been investigated in detail in the literature, but has a particular importance for gasification processes. Temperature measurements are performed at temperatures of ~295-1300 K. In addition, relying on the molecular population differences of CO_2 at different vibrational levels, Section 5.3 investigates high-pressure measurements from vibrational CARS spectroscopy up to 20 bar.

5.1 Thermometry from single Q-branch CARS spectra

5.1.1 CO_2 Q-branch ultrabroadband CARS thermometry

CARS thermometry on N_2 has been extensively investigated, because it is a dominant species in air-fed combustion processes. For other applications like coal gasification [Irfan2011] or reactions in hydrocarbon-based reacting flows [Roy2010b], CO_2 becomes a major species. Compared to N_2 or H_2, CO_2 has the smallest Raman shift, meaning that more pump and Stokes pairs from the ultrabroadband excitation pulse may contribute to the Raman excitation of CO_2, which should provide a pronounced CARS signal intensity. Therefore, it may be a well-suited gaseous molecule for temperature measurements.

The temporal evolution of the ultrabroadband CO_2 CARS signal with regard to the probe

delay at 295 K was investigated at first for choosing proper probe delays and proper spectral peaks for temperature measurements. Fig. 5.1 (a) shows the CARS signals measured in pure CO_2 at 1.7 bar. The displayed CARS signals are the integrated intensities over the spectral range for each separately resolved CO_2 CARS peak.

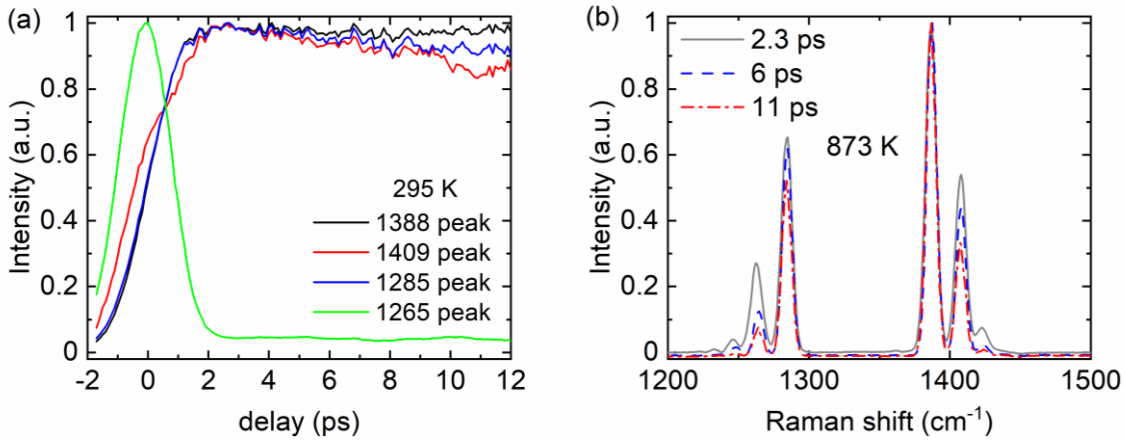

Fig. 5.1 (a) Time-resolved CO_2 CARS signals measured in pure CO_2 at 295 K, 1.7 bar. The curves show the normalized integrated spectral intensities of CO_2 peaks centered at 1388 cm^{-1}, 1409 cm^{-1}, 1285 cm^{-1} and 1265 cm^{-1}, respectively. (b) CO_2 CARS spectra measured at 873 K, 1.7 bar and probe delays of 2.3 ps, 6 ps and 10 ps. The spectra are normalized to their spectral intensity centered at 1388 cm^{-1}.

As discussed in Fig. 2.4, the peaks centered at 1388 cm^{-1} and 1285 cm^{-1} are from the same (00^00) level while peaks centered at 1409 cm^{-1} and 1265 cm^{-1} are from level (01^10). The temperature is determined from populations of the level (00^00) and level (01^10). When the temperature is rising, the higher vibrational level (01^10) is populated (see Section 2.3). This means that the intensities of the 1409 cm^{-1} and 1265 cm^{-1} peaks increase compared to the intensities of the 1388 cm^{-1} and 1285 cm^{-1} peaks. Therefore, we may rely on either 1388 cm^{-1}/1409 cm^{-1} or 1285 cm^{-1}/1265 cm^{-1} peak pairs to extract the temperature. In Fig. 5.1 (a), the peak centered at 1265 cm^{-1} shows a quite different evolution compared to the other three peaks. This is because its peak intensity is too low at this temperature, thus it mainly displays the evolution of the nonresonant background in that spectral range. This means that the 1285 cm^{-1}/1265 cm^{-1} peak pair is less sensitive for low temperature (e.g. 295 K) measurements, whereas the 1388 cm^{-1}/1409 cm^{-1} peak pair is more suitable.

The integrated CO_2 CARS signals (with sufficient resonant contributions) in Fig. 5.1 (a) show almost no Raman coherence dephasing for probe delays of up to ~4 ps. This delay range is also free from molecular collisions at the pressures of our interest ($\leq$20 bar)

[Wrzesinski2013]. Therefore, temperature measurements are mainly implemented at probe delays $\lesssim$ 4 ps in this thesis. At longer delays, different dephasing rates are observed for the three peaks, with the 1409 cm^{-1} peak showing the fastest decay. To clearly display the spectral evolution of these peaks, CO_2 CARS spectra measured at 873 K are shown in Fig. 5.1 (b) for different probe delays. Nevertheless, the CO_2 CARS signal in general decays more slowly than the CARS signal of N_2 [Lucht2006, Kulatilaka2010].

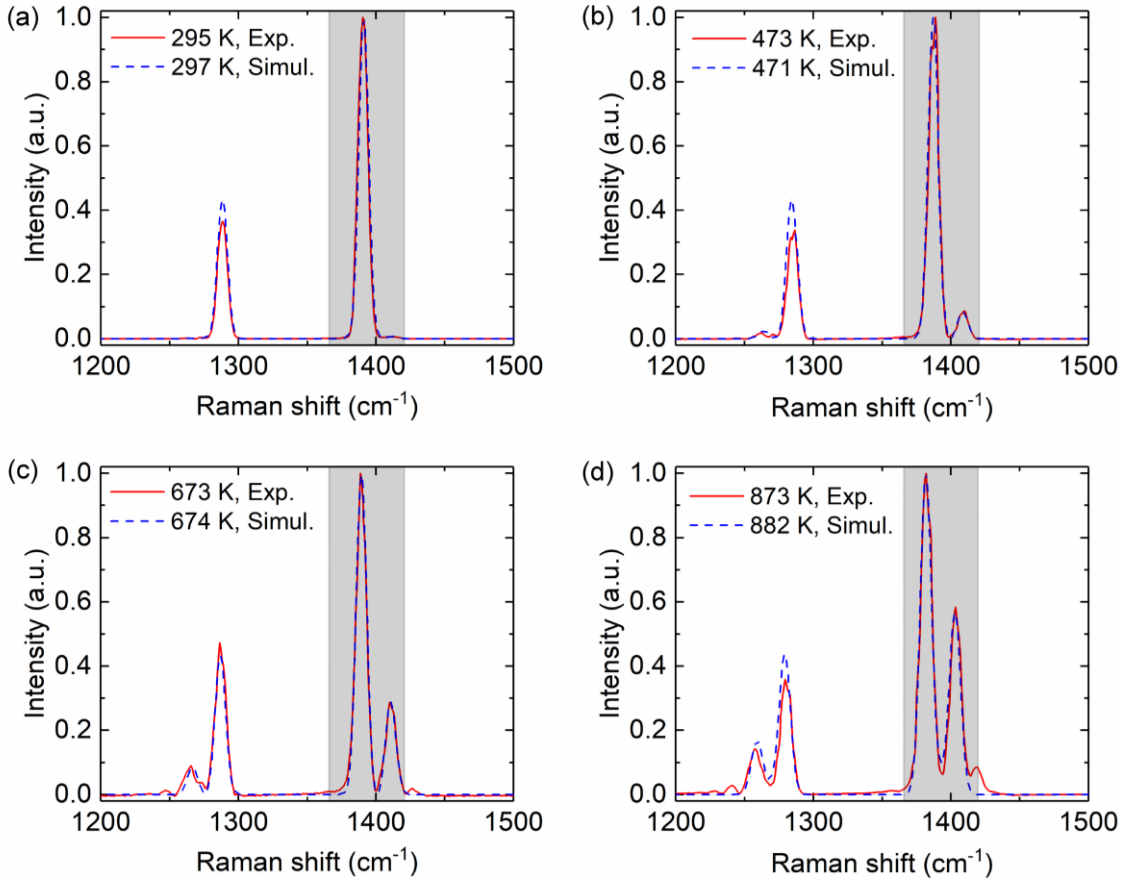

Fig. 5.2 Experimental CO_2 CARS spectra (at 1-3 ps probe delay) at a temperature of (a) 295 K, (b) 473 K, (c) 673 K, (d) 873 K and at a pressure of 1.7 bar with the best-fit simulated spectra. The region where the spectrum is used for fitting is marked with a grey shadow.

To determine the temperature, as discussed in Section 3.2, we fit the simulated CARS spectrum with the background corrected experimental one by optimizing (1) temperature T, (2) probe pulse duration $\Delta\tau_{pr}$, and (3) the spectral shift S_{shift} between the simulated and the background corrected experimental spectrum. Fig. 5.2 shows thermometry results from the measured CO_2 CARS spectra at 295 K, 473 K, 673 K and 873 K. The experimental CARS spectra at different temperatures are shown in red, while the simulated ones obtained from the genetic algorithm fitting are shown with dashed blue curves. When the temperature

reaches ~873 K (see Fig. 5.2 (d)), additional side peaks at ~1425 cm^{-1} and ~1247 cm^{-1} are visible because higher energy levels are populated, which corresponds to transitions between $(0,2^2,0)$ and $(1,2^2,0)_{1,2}$ levels [Chedin1979, Kerstan2017]. However, due to the lack of information in the literature about the corresponding Raman cross sections, they are not considered in the simulation model.

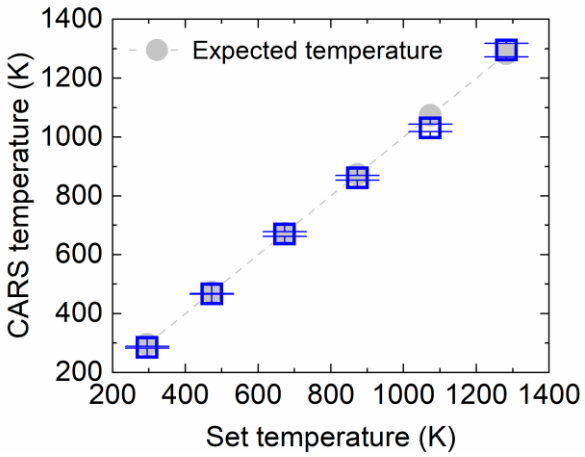

Fig. 5.3 Temperature measurement results from ultrabroadband CO_2 CARS at 295 K, 473 K, 673 K, 873 K, 1073 K and 1283 K in pure CO_2, at 1.7 bar. The grey dashed line and the grey dots indicate the temperatures expected from the temperature controllers. The blue squares show average results from 8 CO_2 CARS spectra at ~1-4 ps and the error bars show the standard deviations.

Based on the ultrabroadband CO_2 CARS spectra, the measurement results from room temperature to ~1300 K in pure CO_2 are shown in Fig. 5.3. High accuracy and precision are achieved over the entire temperature range. In general, the absolute error bar increases with temperature except for room temperature, where the error bar is slightly larger than the one at 473 K. This may come from the relatively low intensity of the 1409 cm^{-1} peak at 295 K (Fig. 5.2(a)). Nevertheless, from 295 K to 1283 K, the measured temperature accuracy is found to be within 4.0% of the set temperature and the precision is thus found to be within 1.3% of the mean temperature. The high measurement accuracies that have been achieved covering 295 K to ~1300 K are difficult for other fs-CARS techniques based on N_2 vibrational spectra. As discussed in Section 2.2, the N_2 vibrational CARS thermometry mainly focuses on high temperatures (>1000 K), because the first hot band starts to appear at this level. Otherwise, quite high spectral resolution ($\lesssim$1 cm^{-1}) is needed for resolving the N_2 rovibrational manifold structure. This requires additional efforts for generating high-

resolution probe pulses with sufficient energies [Scherman2016]. Note that due to the spectrally broad excitation pulse, the excitation efficiencies for the closely lying peaks at 1388 cm^{-1} and 1409 cm^{-1} should be quite similar. In this case, additional spectral referencing is not considered. If the nonresonant spectrum, however, shows clear differences at these Raman shifts, it should be considered. This was the case for the measurement at 1283 K (Fig. 5.3). Nevertheless, the influence of spectral referencing is more crucial for concentration measurements, as the Raman shifts and thus, the excitation efficiencies of the different molecules may differ significantly in the ultrabroadband configuration. The details of the spectral referencing is discussed in Section 6.2, where the concentration measurements are presented.

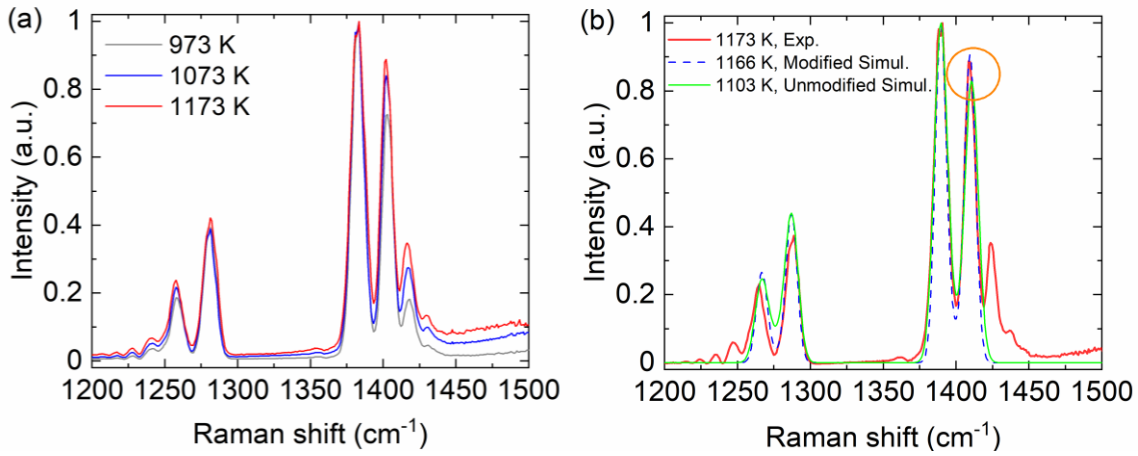

Fig. 5.4 (a) Ultrabroadband CARS spectra measured at 973 K, 1073 K and 1173 K in pure CO_2 atmosphere at a probe delay of ~3.7 ps and a pressure of ~1.5 bar. (b) A comparison of the unmodified simulated CO_2 CARS spectrum and the modified simulated spectrum with the experimental one at ~3.4 ps. The differences are highlighted with an orange circle.

For temperatures ≳1100 K, the population of more rovibrational states (Fig. 2.8) in (00^00) and (01^10) (Fig. 2.4) leads to an overlap of the side wings of the two peaks at 1388 cm^{-1} and 1409 cm^{-1} (Fig. 5.4 (a)). In addition, at higher temperatures, the reduced beam pointing stability at the probe volume leads to random changes of the pump/Stokes spectrum, thus the random variation of the excitation efficiency. This in the end results in randomly distributed shifts of different peaks in the CARS spectra. As shown in Fig. 5.4 (a), at 1173 K, the peaks centered at ~1409 cm^{-1} and ~1265 cm^{-1} seem to show a slight red shift compared to the spectrum at 973 K, while the peak centered at ~1285 cm^{-1} shows a blue shift and the one at ~1388 cm^{-1} remains unchanged. Both small changes in the spectral properties may

influence the temperature measurement when adapting the spectral optimization.

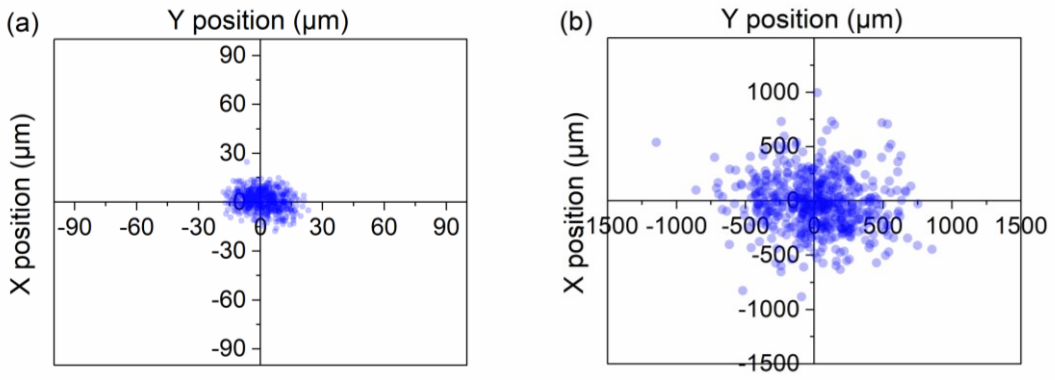

Fig. 5.5 Pointing stabilities of the Pump/Stokes and the probe beams at (a) 295 K and (b) 1073 K measured at the spectrometer position over 5 minutes with a time interval of ~500 ms. The data were acquired using a Newport camera (see Section 4.1).

The decrease of the beam stability can be confirmed by the measured beam positions at the spectrometer position. Fig. 5.5 shows the beam positions measured at 295 K and 1073 K over 5 minutes, where the deviation of the beam positions at 1073 K is orders of magnitude larger than that of 295 K. Fig. 5.4 (b) shows an example of the simulated spectrum (unmodified Simul. in green) in comparison to the experimental one (red) after using the optimization explained in Section 3.2. A clear mismatch for the peak centered at ~1409 cm^{-1} is observed (orange circle), probably because the optimization algorithm (Section 3.2) fails to achieve a best-fit spectrum when all peak positions are fixed. As the relative intensity between the 1388 cm^{-1} and the 1409 cm^{-1} peak pairs is important for temperature determination (see Fig. 5.2), we introduce an additional fitting parameter $\Delta\tilde{\nu}_{1409}$ for adjusting the Raman shift of the ~1409 cm^{-1} peak for temperatures above 1100 K. Furthermore, the probe pulse duration is fixed by using the value that has been optimized from relative lower temperature measurements. The simulated CARS spectrum using the fit parameter $\Delta\tilde{\nu}_{1409}$ and a fixed pulse duration is shown in Fig. 5.4 (b) (dashed blue line). In this case, the peaks at 1388 cm^{-1} and 1409 cm^{-1} agree well with the experimental spectrum, resulting in a temperature of 1166 K, which is significantly closer to the set temperature (1173 K) than without the above mentioned correction (1103 K).

In addition, to check the thermometry performance when additional molecules are present together with CO_2, we investigated the temperature measurements in CO_2-N_2 gas mixtures with 10%, 20% and 30% N_2, respectively. Fig. 5.6 shows the measurement results up to ~900 K. At each temperature, the data points show the average temperature results with the

error bars as the standard deviations from 8 CARS spectra at ~1-3 ps probe delay. Compared to the results in pure CO_2 (Fig. 5.3), a similar precision decreasing trend is observed from 473 K to 873 K. For all the CO_2-N_2 gas mixtures with different N_2 amounts, the measurement accuracies are found to be within 4.3% of the set temperatures and the precisions are found to be within 2.3% of the mean temperatures up to 900 K, which shows similar performance as in pure CO_2.

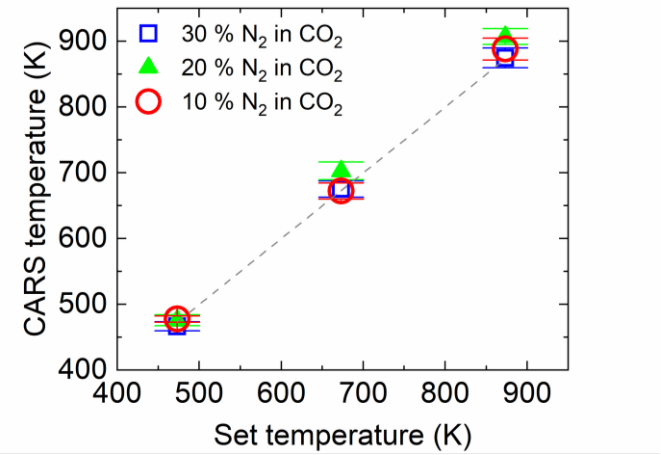

Fig. 5.6 Ultrabroadband CARS temperature measurements based on CO_2 at 473 K, 673 K and 873 K in the gas mixture of CO_2 and N_2 with 10%, 20% and 30% N_2 at 1.7 bar. The grey dashed line indicates the temperatures expected from the temperature controllers.

5.1.2 H_2 Q-branch ultrabroadband CARS thermometry

The ultrabroadband pump/Stokes spectrum enables even the detection of H_2, which has a large Raman shift of ~4161 cm^{-1}. This is important because H_2 is also the product and reactant of combustion reactions (in both N_2-rich and N_2-free environments) [Courtney2017]. Furthermore, H_2 has a large rotational constant B_e (~59.3 cm^{-1}) and a large vibration-rotation interaction constant α_e (~3.0 cm^{-1}) [Richet1977], resulting in only a few Q-branch lines and a wide spacing between these transitions even at a flame temperature (~2000 K) [Eckbreth1996]. Therefore, it is possible to extract the temperature from a single H_2 CARS spectrum. In contrast to CO_2, the thermometry from H_2 is based on the Q-branch manifolds from the same vibrational level, while thermometry from CO_2 uses the populations of two different vibrational states. As with CO_2, the experimental H_2 CARS spectra are fitted with the simulated ones to determine the temperature.

Fig. 5.7 shows the experimental H_2 CARS spectra at 483 K, 673 K, 873 K, and 1078 K with the best-fit simulated spectra. The assignments of the Q(1)-Q(5) lines are marked in

Fig. 5.7 (d). The performance of the H_2-based thermometry in pure H_2 at ~1.7 bar is summarized in Fig. 5.8 (red data points). Up to ~1080 K, the temperatures obtained from the ultrabroadband H_2 CARS have an accuracy within 4.9% of the set temperature and a precision within 2.7% of the mean temperature, showing similar accuracy and precision performance as the thermometry from the ultrabroadband CO_2 CARS spectra, which are 4.3% and 2.3% respectively.

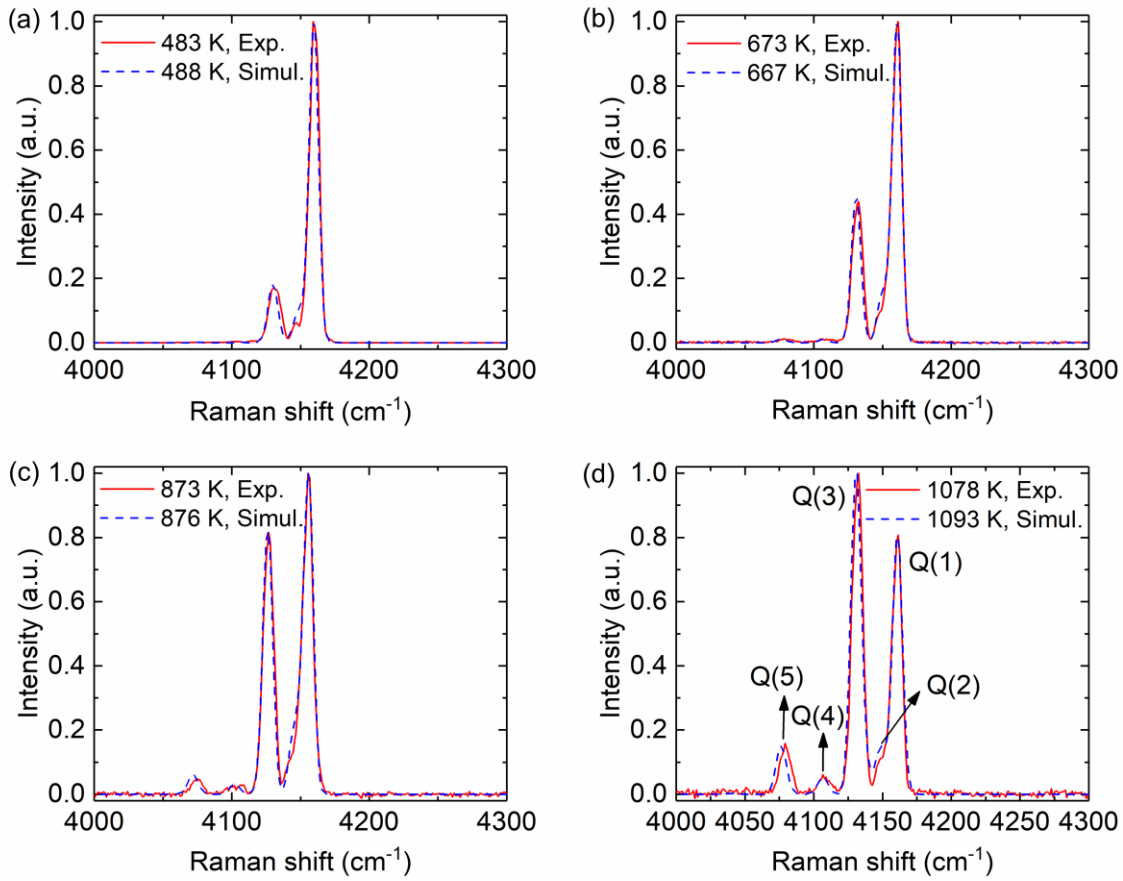

Fig. 5.7 Experimental H_2 CARS spectrum at a temperature of (a) 483 K, (b) 673 K, (c) 873 K, (d) 1078 K and at a pressure of 1.7 bar with the best-fit simulated spectrum.

The spectral line features of H_2 are more easily subject to the vibration-rotation interaction than molecules like N_2, O_2 and CO [Marrocco2011], which is expressed by the Herman-Wallis factors (Equation (2.20)). Therefore, we compare the results with and without considering the Herman-Wallis (HW) factors to check their influence on the accuracies. As shown in Fig. 5.8, the consideration of HW factors in general leads to a slight increase of the determined temperature. This small increase of the measurement result seems to be more obvious at elevated temperatures. However, the overall accuracies and precisions stay quite

similar for both cases (see the values shown in Fig. 5.8 and the table), meaning the deviations between the determined and the set values are mainly caused by systematic factors, for instance, the laser properties, probing environments, the molecular properties, etc. For heavier molecules (e.g. CO_2, CO), the HW factors deviate much less from unity compared to H_2. Therefore, the impact of neglecting the HW factors for these molecules is small.

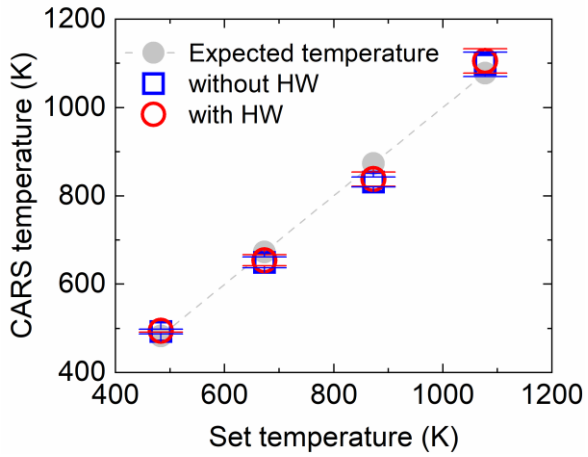

Set Temp./ K	CARS Temp./ K	
	Without HW	With HW
483	493±5.0	494±3.4
673	649±12.3	654±12.7
873	831±11.4	838±16.0
1078	1098±27.7	1106±27.6

Fig. 5.8 Ultrabroadband CARS temperature measurements based on H_2 at 483 K, 673 K, 873 K and 1078 K in pure H_2 at 1.7 bar. Average results from 5 CARS spectra at ~1-3 ps probe delays are displayed with error bars showing the standard deviations. The grey dots with dashed line indicate the temperatures expected from the temperature controllers. The blue and red dots show the results without and with the consideration of the Herman-Wallis (HW) factors. The values for these data points (with uncertainties) are shown in the adjacent table. Temp. is the abbreviation of temperature.

5.2 Thermometry using the decay of the Raman coherence compared to single CARS spectra

Measuring the gas phase temperature by probing N_2 is also interesting because for air-fed combustion it is the dominant constituent throughout the combustion zone [Eckbreth1996]. To resolve the N_2 Q-branch structure, less than 1 cm^{-1} spectral resolution is required [Eckbreth1996, Scherman2016]. Fig. 5.9 shows the experimental N_2 CARS spectra at 500 K, 800 K and 1000 K based on our setup. At ~1000 K, the first hot band ($\upsilon = 2 \rightarrow \upsilon = 1$) centered at ~2300 cm^{-1} starts to appear. For $\upsilon = 1 \rightarrow \upsilon = 0$ Q-branch transitions, a slight

increase of its spectral width is observed with rising temperature. This increase is because more rovibrational manifolds are populated at higher temperatures. However, these distinct spectral lines cannot be resolved from the measured N_2 CARS spectrum which is limited by the spectral resolution provided from the probe pulse. This makes thermometry from a single N_2 CARS spectrum hardly possible for temperatures below ~1000 K. Therefore, for thermometry based on N_2, we focus on the dephasing of the Raman coherence (i.e. using time-resolved CARS signals) which can be calculated according to Equation (3.15). The temperature is extracted by least square fitting the experimental integrated CARS signals over the spectral range of ~2300-2360 cm^{-1} at different delays with the calculated signals.

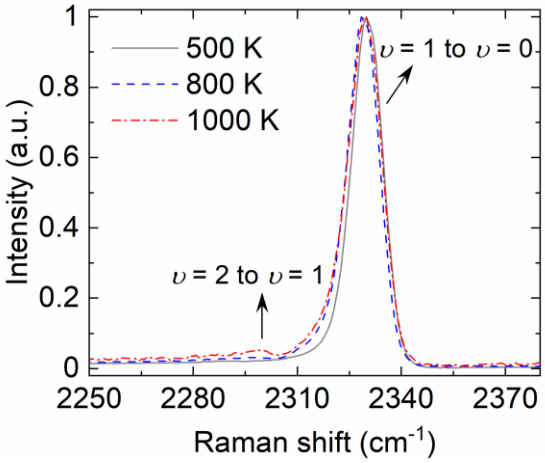

Fig. 5.9 Measured ultrabroadband N_2 CARS spectra at 500 K, 800 K, 1000 K and at a pressure of 1.7 bar.

To compare the ultrabroadband N_2 CARS thermometry performance simultaneously with CO_2 and H_2, we investigated a gas mixture of 40% N_2, 40% CO_2 and 20% H_2 at 1.7 bar. The temperature measurements were implemented at temperatures of 295 K, 500 K, 800 K, and 1000 K. Fig. 5.10 (a) shows a CARS spectrum measured in the N_2-CO_2-H_2 gas mixture at 800 K and 1.7 bar. It is evident that multiple species with Raman shifts up to ~4160 cm^{-1} can be detected simultaneously. However, the H_2 peak intensity seems to be lower than expected even taking into account that its mass flow is half of the other two molecules. This may mainly come from its large Raman shift, resulting in significantly less available Pump-Stokes pairs within the bandwidth of the pump/Stokes pulse compared to the molecules with smaller Raman shifts (i.e. N_2, CO_2). This can be confirmed by the nonresonant spectrum measured in pure argon. As illustrated in Section 3.2, for the ultrabroadband fs/ps CARS,

the excitation efficiency of the pump/Stokes pulse may be estimated from the nonresonant response at the spectral position of the corresponding Raman signal. Fig. 5.10 (b) shows a typical nonresonant response measured in pure argon at 295 K and 2 bar. A significant lower nonresonant response, thus lower excitation efficiency for H_2 is visible compared to that for N_2 or CO_2.

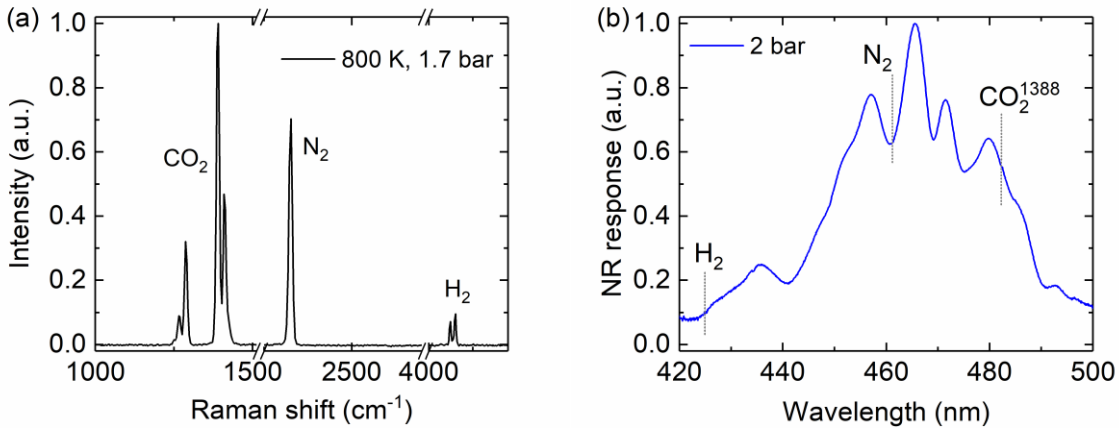

Fig. 5.10 (a) Ultrabroadband CARS spectrum in a gas mixture of 40% N_2, 40% CO_2 and 20% H_2 at 800 K and 1.7 bar. (b) Typical zero-delay nonresonant response measured in pure argon at 295 K and 2 bar. The spectral position of N_2, CO_2 and H_2 are marked with grey dotted lines.

Fig. 5.11 shows the measurement results simultaneously taken from the ultrabroadband N_2, CO_2 and H_2 CARS. For H_2 and CO_2, as discussed in Section 5.1, the optimization between the experimental and simulated CARS spectra is implemented. The data points in Fig. 5.11 (a) show the averaged results based on 10 CARS spectra at probe delays of 1-3 ps. As for N_2, the optimized probe duration fitted from the CO_2/H_2 thermometry is used for the CARS signal calculation at different probe delays based on Equation (3.15). In order to minimize the influence from the nonresonant signal, the least-square fitting of the experimental N_2 CARS decay curves with the calculated CARS signals is performed at delays of ~2-4 ps. Fig. 5.11 (b) displays the dependence of the N_2 CARS signal as a function of the probe delay up to 1000 K. In addition, the best fit simulated curves are shown. Multiple N_2 CARS spectra at different delays are used for a single temperature result. Besides, as shown in Fig. 5.11 (a), the results based on N_2 CARS show relatively large deviations (up to +79 K) from the expected values in the measured temperature range. Error bars are not shown, because the measurement accuracy cannot be addressed from one probe scan and multiple scans would have been required. To increase the measurement accuracy

of the time-resolved N_2 CARS, the beating effects between the first vibrational band with the hot bands may be utilized [Roy2008]. However, as shown in Fig. 5.9, the first hot band ($\upsilon = 2 \rightarrow \upsilon = 1$) begins to appear only above ~1000 K for N_2. Thus in the temperature range of 295-1000 K, it is not feasible to improve the measurement accuracy by considering the beating effects.

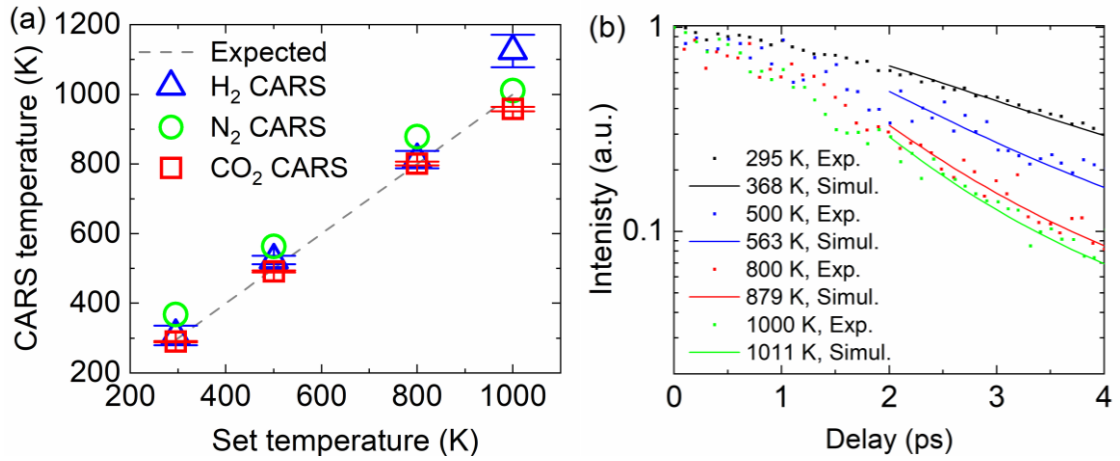

Fig. 5.11 (a) Simultaneous temperature measurements from different molecules using utrabroadband CARS in a gas mixture of 40% N_2, 40% CO_2 and 20% H_2 at 1.7 bar. (b) Experimental and the best-fit time-resolved ultrabroadband N_2 CARS signals at temperatures from 295 K to 1000 K and at a pressure of 1.7 bar.

For the temperature determined from ultrabroadband H_2 CARS spectra, the measurement results in Fig. 5.11 (a) show a good accuracy over the measured temperature range except for 1000 K. The large deviation at 1000 K is mainly due to the too low SNR at such a high temperature. As illustrated in Fig. 5.10, the large Raman shift of H_2 leads to fewer excitation pairs from the pump/Stokes pulse. At a constant pressure, the molecular density decreases during the heating process. The reduced molecular density leads to an even lower SNR of H_2 CARS. In this case, if the H_2 molecular density is too low in the probing environment, another molecule has to be chosen for thermometry.

If the attention is drawn to the ultrabroadband CO_2 CARS, we observe a good agreement for the measured temperatures with the expected ones over the whole temperature range (Fig. 5.11 (a)). This is due to the pronounced CO_2 CARS spectral intensity during the entire heating process and the closely lying Fermi polyads at ~1388 cm^{-1} and ~1409 cm^{-1} for thermometry. For the temperature range from 295 K to 1000 K, the accuracy and precision based on ultrabroadband fs/ps CO_2 CARS is within 4.2% and 0.7%, respectively.

The best performance for thermometry was achieved using ultrabroadband CO_2 CARS in a N_2-CO_2-H_2 gas mixture at 295-1000 K and 1.7 bar. As for the temporal resolution, the acquisition of a H_2/CO_2 CARS spectrum requires ~1 second (50 ms acquisition time × 20 accumulations), while a probe scan for N_2 CARS needs at least a few minutes. Thus, CO_2 is an ideal target molecule for accurate and precise thermometry from a single ultrabroadband CARS spectrum, which is preferable in dynamic processes. Nevertheless, in H_2-rich environments, for instance, in gas turbines, which need to be operated using synthetic gases (H_2, CO and CH_4) or pure H_2 [Taamallah2015], ultrabroadband H_2 CARS holds the potential of reliable temperature measurements (Fig. 5.8).

5.3 Collision-free high-pressure thermometry

The extension of the measurements to the high-pressure regime is of great interest for gasification and combustion systems. In vibrational CARS spectroscopy, elevated pressure was reported to cause the mixing of the individual rovibrational lines. This eventually leads to a narrowing behavior of the CARS spectrum due to the collapse of the rotational structure [Hall1980], which is termed collisional narrowing effect and causes additional difficulties for high-pressure thermometry. However, the collisional energy transfer was reported to mainly happen between the rotational states but hardly in different vibrational states [Eckbreth1996]. Therefore, rovibrational CARS spectra involving the populations of different vibrational levels may hold the potential for high-pressure applications. In this regard, CO_2 is an ideal candidate.

Apart from collisional effects, the high gas pressures may also induce pronounced self-phase-modulation (SPM) and higher order dispersion in the laser beam. Fig. 5.12 (a) shows the nonresonant responses in pure argon from 2 bar to 5 bar and Fig. 5.12 (b) shows the results from a separate measurement between 1.7 bar and 10 bar. As discussed in Section 3.2 and Fig. 3.1, the excitation efficiency of the pump/Stokes pulse can be determined from the nonresonant signal. Therefore, when comparing the nonresonant response at ~2 bar from both Fig. 5.12 (a) and (b), it is clear that the pump/Stokes pulses have different spectral properties, resulting in different nonresonant response profiles. However, at the spectral position of CO_2 CARS, the relative nonresonant response is always increasing as the pressure goes up. For N_2, a similar trend is visible but less pronounced. As H_2 has already a less excitation efficiency compared to N_2/CO_2, it is easily disturbed under high-pressure

environments.

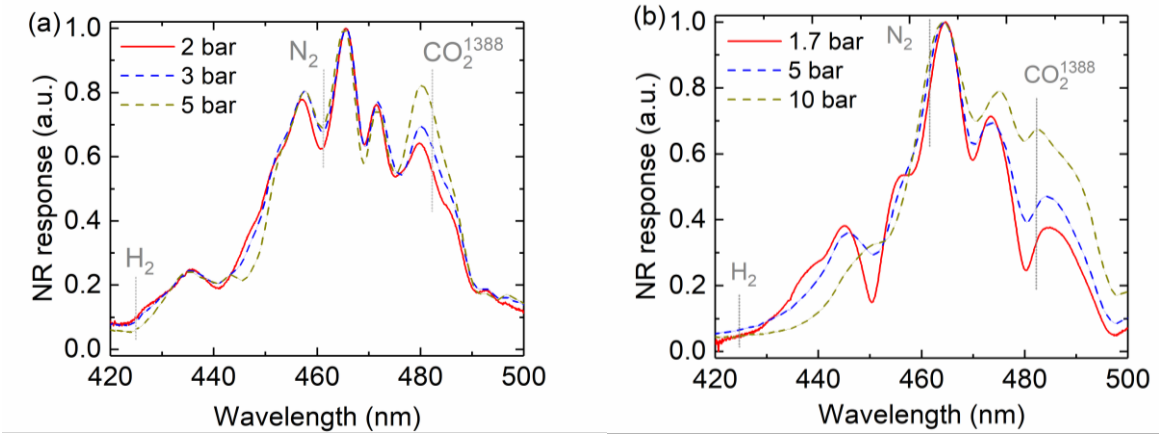

Fig. 5.12 Nonresonant responses measured in pure argon at zero delay and pressures of (a) 2 bar, 3 bar and 5 bar (b) 1.7 bar, 5 bar and 10 bar from two independent measurements. The spectral positions where N_2, CO_2 and H_2 appear are marked with grey dotted lines.

The observed pressure dependence of the nonresonant response measured in pure argon predicts that the ultrabroadband CO_2 CARS may be preferable for thermometry under high pressures. For comparison, considering the advantages of the CO_2 based thermometry discussed in Section 5.2, we performed high-pressure temperature measurements in the same gas mixture (40% N_2, 40% CO_2 and 20% H_2) and determined the temperature from the CO_2 CARS spectra at a few ps probe delays. The measurements were performed at 1.7 bar, 10 bar and 20 bar.

Wrzesinski *et al.* have shown that the pressure-dependent collisional decay occurs at a delay $\tau > 20$ ps at pressures up to ~40 bar using a 85 fs laser system [Wrzesinski2013]. Therefore, it is also advisable to investigate the pressure-dependent behavior of the ultrabroadband CARS. Fig. 5.13 (a) shows the dependence of the experimental ultrabroadband N_2 CARS signal on the probe delay over 0-19 ps range at 295 K and for pressures from 1.7 bar to 20 bar. The N_2 CARS signals exhibit almost no dependence on the gas pressure over the entire region from 0 ps to 12 ps. At ~12 ps, the separation between the N_2 CARS decay curves at different pressures starts to appear. This means the coherent dephasing over ~0-12 ps is independent of the pressure up to 20 bar. In addition, in the measured delay range, we observe no rotational recurrence [Knopp2002, Wrzesinski2013] due to the molecular collisions. Both effects indeed do not disturb the measurements for the delay range (~1-4 ps) we used for temperature determination. In this way, the collision-free thermometry can be performed without considering pressure effects up to 20 bar.

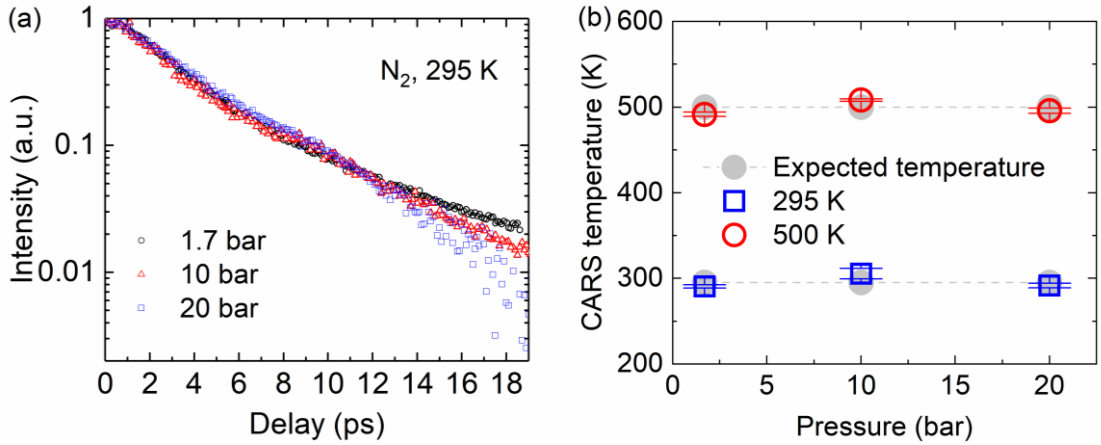

Fig. 5.13 (a) Experimental time-resolved ultrabroadband N_2 CARS signals at pressures of 1.7 bar, 10 bar and 20 bar and a temperature of 295 K in a gas mixture of 40% N_2, 40% CO_2 and 20% H_2. (b) The temperature measurement results from ultrabroadband CO_2 CARS spectra at pressures of 1.7 bar, 10 bar and 20 bar in a gas mixture of 40% N_2, 40% CO_2 and 20% H_2.

Utilizing the CO_2 CARS spectra, Fig. 5.13 (b) displays the temperature results at 1.7 bar, 10 bar and 20 bar. From room temperature to 500 K, the measurements result in an accuracy within 4.2%, and a precision within 2%. These results prove the feasibility of collision-free high-pressure (up to 20 bar) thermometry based on our ultrabroadband two-beam fs/ps CARS setup. Measurements at even higher temperatures were not investigated due to the limit of the heating ability of the oven at high pressures (Section 4.3).

6 Ultrabroadband CARS concentration measurements

This Chapter investigates the capability of concentration measurements using ultrabroadband CARS in different binary or ternary gas mixtures. For this purpose, concentration investigations are performed for species with Raman shifts up to ~4200 cm^{-1}. The accuracy as well as the detection limit achievable using the sub-10 fs excitation beam have not been investigated in detail so far. Therefore, in Section 6.1, concentration measurements of N_2 in CO_2 and of CO in CO_2/N_2 as low as 0.5% are studied. In Section 6.2, concentration measurements are implemented in the ternary gas mixtures CO_2-N_2-CH_4 and CO_2-N_2-H_2. The impact of pump/Stokes spectral referencing from the nonresonant spectrum measured in argon is analyzed in detail and high-pressure concentration measurements up to 10 bar are studied.

6.1 Concentration measurements in CO, N_2 and CO_2 mixtures

Using ns-laser-based CARS, a detection limit of 0.5% CO in cold Ar atmosphere and a limit of 10% CO in a flame (at ~2000 K) were reported [Eckbreth1981]. For fs-laser-based CARS, the sensitivity of concentration measurements has not been investigated in detail so far. Richardson et al. reported concentration measurements mainly focusing on ~10% CO concentration level using CPP fs CARS [Richardson2013]. Using this technique, the CARS spectra of multiple molecules overlap, thus may be not suitable for distinguishing low concentration species. Bohlin et al. presented mole fraction ratios for the major species of a methane/air flame using an ultrabroadband pump/Stokes pulse and a 75 ps probe pulse [Bohlin2017]. Due to the long probe pulse duration, the delays of 60-200 ps were used, for which the CO signal was too low for a quantitative analysis. In this regard, the CO detection limit using our ultrabroadband fs/ps CARS system is of particular interest in this study. In

addition, this is an important concern for coal gasification investigations, which require high sensitivity of monitoring CO (Section 2.7).

As discussed above, a long probe pulse duration is not suitable for the detection of low density species. Using a ~2 ps probe pulse, our setup configuration may have the intrinsic advantage for minor species detection in a gas mixture. Pestov et al. reported that the CARS signal maximizes at some positive probe delay instead of the zero delay where the nonresonant signal gets its maximum in bacterial endospores [Pestov2008b]. To verify this for gas phase measurements, we performed a nonresonant measurement in pure argon which was followed by a CARS measurement in a N_2-CO_2-CH_4 gas mixture at ~2 bar and 295 K. Fig. 6.1 shows the time-resolved N_2 CARS signal with the nonresonant signal of argon. The nonresonant signal evolution in Fig. 6.1 yields its maximum value at zero delay. However, the maximum CARS signal is detected at around 1.5 ps. The experimental result is in good accordance with the simulated results reported by Ariunbold et al. [Ariunbold2016a, Ariunbold2016b], where they showed that a ~10 cm^{-1} probe pulse yields maximum resonant CARS at ~1.5-1.6 ps probe delays. This means that when CARS signals at a few ps probe delays are used for concentration determination, the nonresonant contribution is reduced while simultaneously the CARS signal may be enhanced, yielding a good SNR. On the other hand, too long probe delays are not preferable due to possible collisional effects.

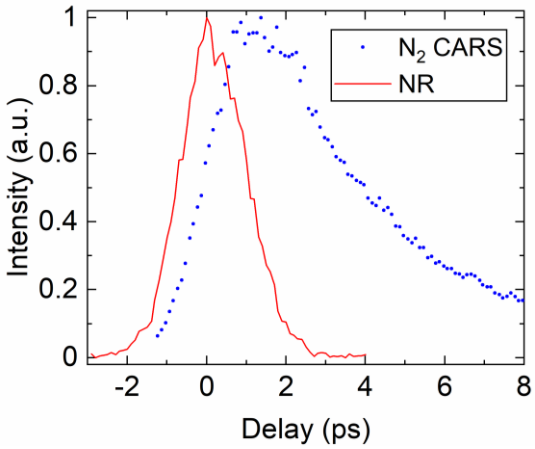

Fig. 6.1 Comparison of the nonresonant (NR) signal and the CARS signal evolution. The NR signals are measured in pure argon and the integrated N_2 CARS signals are measured in the gas mixture of N_2-CO_2-CH_4 at ~2 bar and 295 K under the same laser condition.

Based on this benefit, in this section, we focus on the concentration measurements in gas mixtures involving CO, N_2 and CO_2. At first, we examine the spectral fitting performance.

To extract concentration information, the simulated ultrabroadband CARS spectra are fitted with the background-corrected experimental ones by optimizing the scaling factors β_i for different molecules, the probe pulse duration $\Delta\tau_{pr}$, and the shift S_{shift} between the experimental and the simulated spectra (Section 3.2). Fig. 6.2 shows typical experimental CARS spectra with the best-fit simulated ones at 473 K in a N_2-CO_2 gas mixture with 30% and 10% N_2, respectively. From the N_2 CARS peak intensities in Fig. 6.2, it is observed that the concentration information can be mainly extracted from the relative spectral intensities of the different molecules.

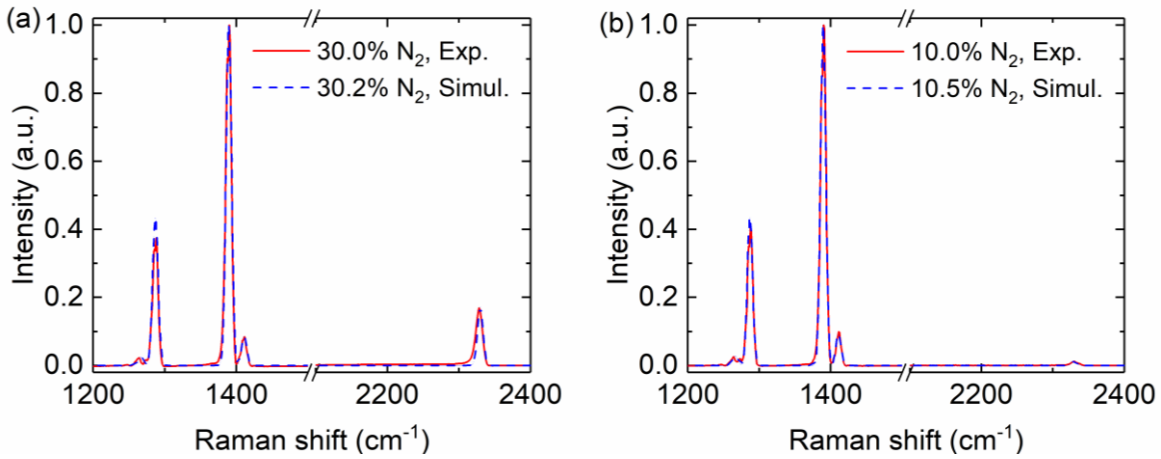

Fig. 6.2 Experimental and the best-fit simulated CARS spectra for (a) 30% N_2 and (b) 10% N_2 in a gas mixture of N_2 and CO_2 at a probe delay of ~2.1 ps and at 473 K, 1.7 bar.

Then the performance of the concentration determination was examined at different temperatures in a N_2-CO_2 gas mixture with 10%, 20% and 30% N_2, respectively. Fig. 6.3 (a) shows the measurement results at temperatures of 473 K, 673 K, 873 K and a pressure of 1.7 bar. 8 CARS spectra at ~1-3 ps delays are used for the concentration determination. At higher temperatures (i.e. 873 K), convection along the beam, especially at the probe volume, causes disturbance on the pump/Stokes pulses. This disturbance may lead to changes of the self-phase-modulation and the excitation efficiencies (Section 3.2) of the ultrabroadband pulses compared to the lower temperature measurements. Thus a decrease of the concentration accuracy is obtained. In addition, the decrease of the beam pointing stabilities at the spectrometer end (Fig. 5.5) leads to a decrease of precision for higher temperature measurements.

The sensitivity of CO determination was investigated in CO-CO_2 or CO-CO_2/N_2 gas mixtures at various temperatures. Fig. 6.3 (b) shows a summary of the CO concentration

measurement results at ~1.4 bar. At room temperature, the CO concentration in the CO-CO_2 gas mixture was investigated from 10% down to 2%. For 2% CO in CO_2 atmosphere, the measurements were investigated at 295 K, 773 K and 1073 K. The performance of the measured results is displayed in the inset of Fig. 6.3 (b). From 295 K to 1073 K, this low CO concentration is accurately determined. At 1073 K, a decreasing precision is observed due to the larger convection. In a gas mixture of 39.5% CO_2 and 60% N_2, we could even measure as low as 0.5% CO, despite of the closely lying CARS peaks of CO and N_2.

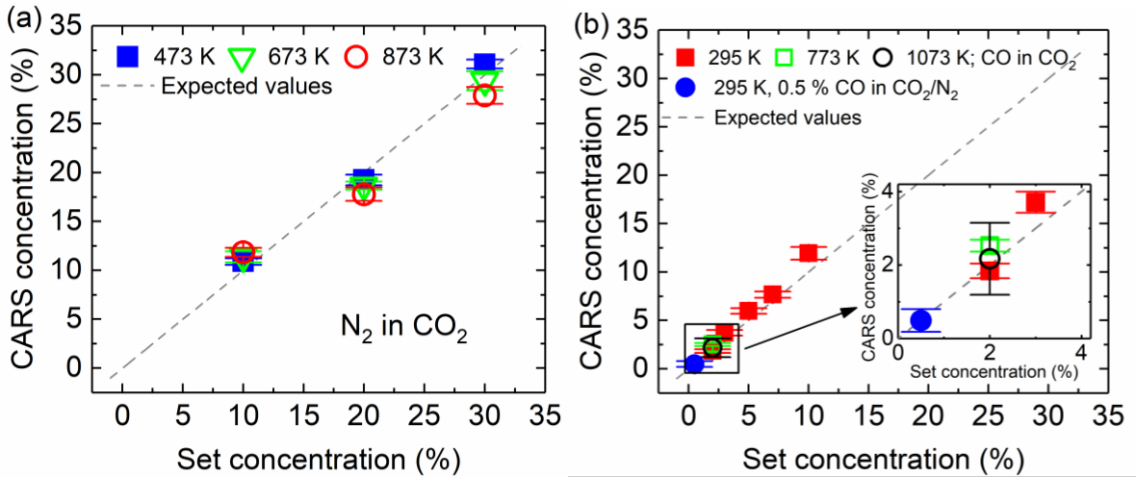

Fig. 6.3 Ultrabroadband fs/ps CARS concentration measurements in (a) CO_2/N_2 gas mixtures with 10%, 20% and 30% N_2 at 473 K, 673 K and 873 K, 1.7 bar. (b) CO in CO_2 or CO in CO_2/N_2 gas mixtures with CO concentration down to 0.5% at temperatures from 295 K to 1073 K, 1.4 bar. The concentration results show the average results of 8 fits with the standard deviations (error bars). The grey dashed line shows the expected concentrations from the set concentrations of the mass flow controllers.

A typical CARS spectrum for the 2% CO in CO_2 atmosphere at ~1.6 ps and a temperature of 773 K is displayed in Fig. 6.4, yielding a measured CO concentration of 2.5%. The red curve shows the experimental spectrum while the best-fit simulated spectrum is shown with black dashed line. The inset displays a clear CO CARS peak despite its low intensity. At 1073 K, the 2% CO concentration is determined to be (2.2±1.0)%. For the lowest investigated CO concentration (0.5% CO) shown in Fig. 6.3 (b), the measured value is determined to be (0.5±0.3)% at 295 K. Note that the uncertainty of the CO concentration from the mass flow controllers is already ±0.2%. More detailed results of interest (from Fig. 6.3) are summarized in Table. 6.1, including the results of different gas compositions at the highest measured temperatures or the results at certain temperatures but with the

lowest CO concentrations.

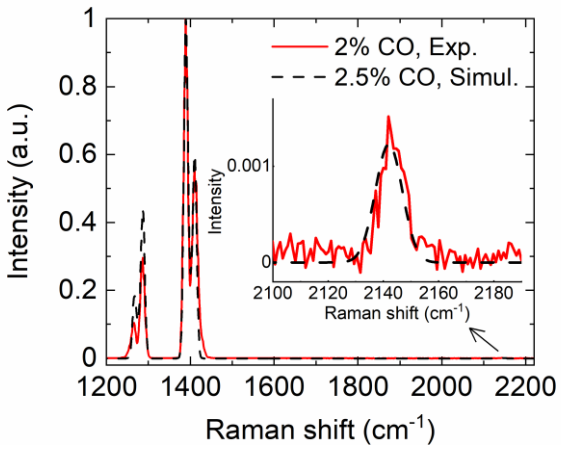

Fig. 6.4 Representative experimental and best-fit simulated CARS spectra at ~1.6 ps probe delay in a 2% CO and 98% CO_2 gas mixture at 773 K and 1.4 bar.

Table. 6.1 Concentration measurements based on two-beam ultrabroadband fs/ps CARS. The accuracies of the set gas concentration are calculated from the accuracies of the mass flow controllers.

Concerned gas in gas mixture(s)	Pressure /bar	Set concerned gas concentration/%	Temperature /K	Determined concentration/%
N_2 in CO_2	1.7	30.0 ± 0.4	873	27.9 ± 0.9
		20.0 ± 0.3		17.8 ± 0.7
		10.0 ± 0.2		11.8 ± 0.5
CO in CO_2	1.4	2.0 ± 0.2	1073	2.2 ± 1.0
			773	2.5 ± 0.2
			295	1.8 ± 0.2
CO in N_2, CO_2		0.5 ± 0.2	295	0.5 ± 0.3

It is difficult to extend the CO detection limit to even lower concentrations (<0.5%). This is because the CO CARS signal is too low due to the dephasing decay at larger probe delays. At higher temperatures, this dephasing decay becomes even more rapidly [Lucht2006]. Fig. 6.5 displays the 2% CO CARS spectra in 98% CO_2 at near zero probe delays measured at 773 K and 1.4 bar. At zero delay, a pronounced nonresonant background is observed. Due to the low CO concentration, the CARS spectrum displays a modulated behavior between

the resonant susceptibility and the nonresonant susceptibility (Section 3.3). As shown in Fig. 6.5, when the detuning from the resonance is positive (at smaller Raman shift), the CARS signal arises above the nonresonant background. For negative detuning, the CARS spectrum subtracts from the nonresonant background. This results in a maximum spectral intensity not at the CO CARS resonance (~2143 cm^{-1}) (see zero delay spectrum in Fig. 6.5). When the probe is delayed at ~1.6 ps, the nonresonant contribution is largely reduced, thus a CO CARS spectrum centered close to ~2143 cm^{-1} is observed (marked with red dashed line in Fig. 6.5).

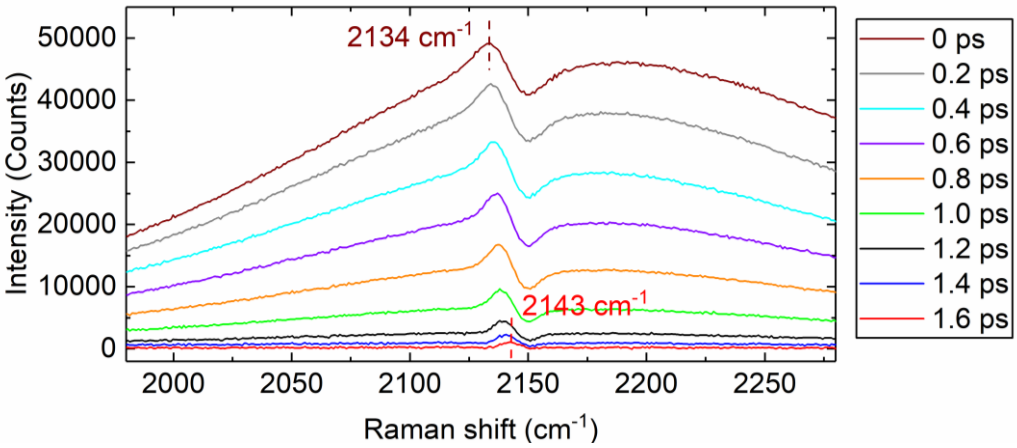

Fig. 6.5 2% CO CARS spectral evolution in 98% CO_2 atmosphere at 773 K and 1.4 bar for different probe delays.

The observed evolution of the CO CARS signal confirms that the presence of the nonresonant background does enhance the overall signal levels for species with minor concentrations. One can anticipate that this 2% CO CARS signal will soon disappear at a probe delay of ≳2 ps. If the CARS spectra at delays, where the nonresonant signal plays a role, can be utilized, the detection limit and concentration measurement limit of our ultrabroadband CARS system may be further extended. Using the CO CARS modulation dips of the nonresonant signal (introduced in Section 3.3), a higher sensitivity will be discussed in Chapter 7 for coal gasification.

6.2 Concentration measurements in CO_2, N_2 and CH_4/H_2 mixtures

In this section, the possibility of concentration measurements for multiple molecules with

large Raman shifts (e.g. CH_4, H_2) is investigated. The excitation efficiency from the ultrabroadband pump/Stokes spectrum can hardly be adjusted to have a similar value for these molecules. Therefore, investigations on how much the spectral change may influence the excitation efficiencies for different molecules are of particular interest, which provides the knowledge for quantitative concentration measurements using ultrabroadband CARS. In narrowband CARS, Farrow et al. [Farrow1985] have recorded the CARS signal and the nonresonant signal simultaneously, and the nonresonant signal was used to normalize the CARS signal for quantitative measurements. The spatial variations of the laser fields and the pulse-to-pulse temporal variations were compensated in this way. For ultrabroadband CARS, Bohlin et al. [Bohlin2014b] have suggested to collect the nonresonant signal simultaneously with the CARS signal in a similar manner. However, this is challenging because even for narrowband CARS with proper polarization control on all the pump, Stokes and probe beams, the elimination or separation of the nonresonant signal will lead to at least a factor of 16 reduction in the CARS signal [Eckbreth1981]. For ultrabroadband CARS with pump and Stokes pairs provided from the same beam, the pump and Stokes polarizations cannot be easily separately controlled. Therefore, the CARS signal may experience a severe reduction. Nevertheless, our pump/Stokes spectrum shows excellent shot-to-shot stability performance (Fig. 4.5 (b)) and high stability over several hours. This allows measuring the nonresonant signal and the resonant CARS independently. Based on this, we determine the excitation efficiencies for different molecules from the measured nonresonant responses in pure argon and then extract concentrations from the ultrabroadband CARS spectra. The measurements focus on ternary gas mixtures with molecules having large Raman shifts (i.e. ~3000-4200 cm^{-1}).

6.2.1 Impact of ultrabroadband spectral referencing from the nonresonant spectrum in Ar

At first, we investigated how different pump/Stokes spectral conditions influence the nonresonant spectra measured in pure argon, and correspondingly, the influence on the concentration measurements for molecules with large Raman shifts. For this purpose, the temporal overlap of the pump and the seed beam of the first NOPA stage in the OPCPA system (Section 4.1) was moderately changed by using a fine-tuning delay stage. This random vary of the temporal overlap resulted in pump/Stokes spectral changes, therefore, the day-to-day realignment of the OPCPA system was simulated.

The measurements were first investigated in a gas mixture with maximum molecular Raman shifts to be ~3000 cm^{-1}. The gas composition was chosen to be CO_2, N_2 and CH_4 at 1.7 bar and 295 K. Prior to CARS measurements with the target gases, the gas oven was filled with pure argon to measure the nonresonant spectra with a specific pump/Stokes spectral condition. Fig. 6.6 (a) shows the pump/Stokes spectrum before and after moderately changing the temporal overlap in the laser system (the resulting change of the pump/Stokes power was controlled to be within 100 mW, meaning an energy change within 5%), which are denoted as measurement 1 (M1) and measurement 2 (M2), respectively. The pump/Stokes spectrum shows a small red shift after the tuning. The corresponding nonresonant spectra measured in pure argon are displayed in Fig. 6.6 (b). The nonresonant spectrum of M2 changes significantly and shows some modulation behavior, which cannot be simply predicted from a pump/Stokes spectral shift. The overall nonresonant signal intensity of M2 is shown to be larger than that of M1, nevertheless, the relative nonresonant intensity at the frequency positions of the target molecules is the major concern for concentration determination.

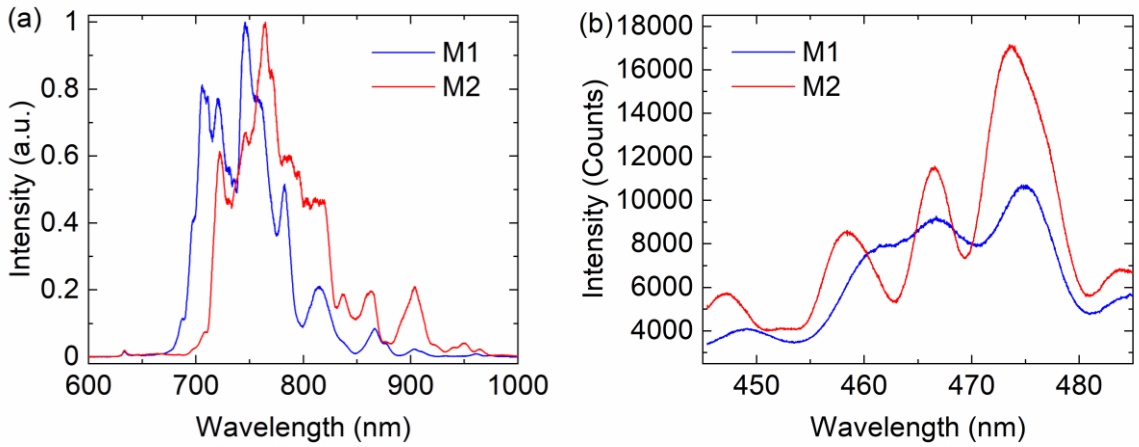

Fig. 6.6 (a) Pump/Stokes spectra before (M1) and after (M2) the random tuning of the temporal overlap in the first NOPA stage in the OPCPA system and the corresponding (b) nonresonant spectra measured in pure argon at 295 K and 1.7 bar in the spectral range of the CO_2, N_2 and CH_4 CARS signals. M1: measurement 1; M2: measurement 2.

After each of the nonresonant spectra recording, the gas oven was refilled with the CO_2-N_2-CH_4 gas mixture (37.5% CO_2, 50.0% N_2, 12.5% CH_4) to 1.7 bar and the CARS spectra were measured. Fig. 6.7 (a) shows the CARS spectra together with the nonresonant spectra for the two measurements. For comparability reason, the nonresonant and the CARS signals are

normalized to the signal strength at the Raman shift of N_2 (~2330 cm^{-1}). The correspondence between the CARS intensity and the nonresonant intensity is visible in Fig. 6.7 (a). At the Raman shifts of CO_2 (~1388 cm^{-1} and ~1285 cm^{-1}), the intensity of the nonresonant signal for M2 is twice as high as for M1. Accordingly, the CO_2 CARS doubles its intensity from M1 to M2. A similar relation is also observed for the signals at the Raman shift of CH_4 (~2917 cm^{-1}). As discussed in Section 3.2, the excitation efficiencies can be retrieved from the nonresonant signal at the frequency positions of the corresponding molecules, which is confirmed by the results shown in Fig. 6.7 (a).

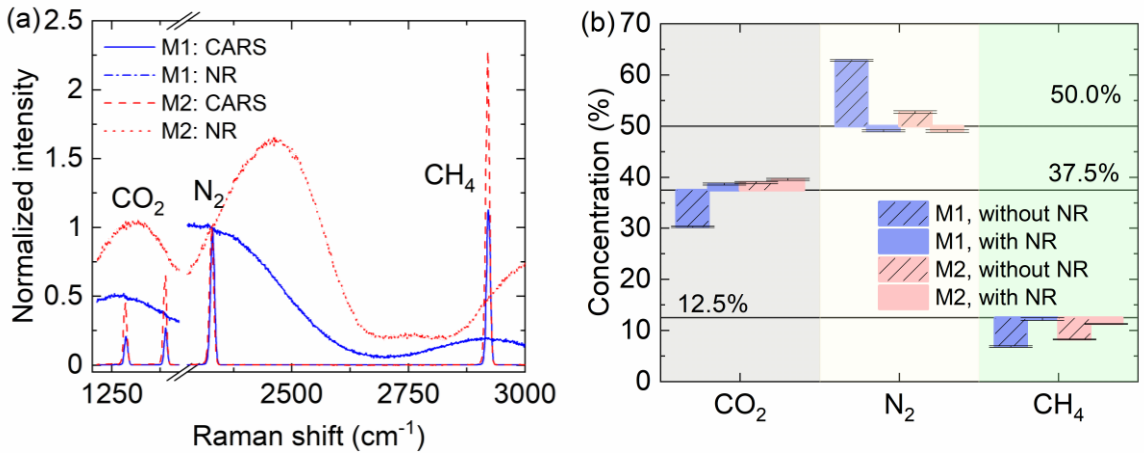

Fig. 6.7 (a) CARS signals in a gas mixture of 37.5% CO_2, 50% N_2, and 12.5% CH_4 at ~2.2 ps delay with the nonresonant spectra measured in pure argon at zero delay at 1.7 bar and room temperature. NR: nonresonant signal; M1: measurement 1; M2: measurement 2. (b) Concentration measurements with and without considering the nonresonant response for M1and M2 for two different pump/Stokes spectra at 1.7 bar and room temperature. The bars show the averaged results from 5 CARS spectra at probe pulse delays of ~1-3 ps. Error bars show the standard deviations. Black lines indicate the concentrations expected from the settings of the mass flow controllers.

Fig. 6.7 (b) gives the comparison of the concentration measurement results with and without considering the nonresonant responses measured in pure argon. The blue bars show the concentrations determined from M1 while the pink bars show the results from M2. The results without considering the nonresonant response are displayed with slashes. For M1, a significant improvement is obtained when the nonresonant response is considered, leading to accuracies within 3% of the set concentrations for all molecules (CO_2, N_2, CH_4). The improvement for CO_2 and N_2 in M2 is not so obvious. This is because the nonresonant responses at the Raman shifts of ~2330 cm^{-1} and ~1388 cm^{-1} for CO_2 and N_2 are quite similar.

In addition, the error bars displaying the standard deviations of the measurements in Fig. 6.7 (b) are small throughout the study, which is attributed to the high stability of the pump/Stokes spectrum.

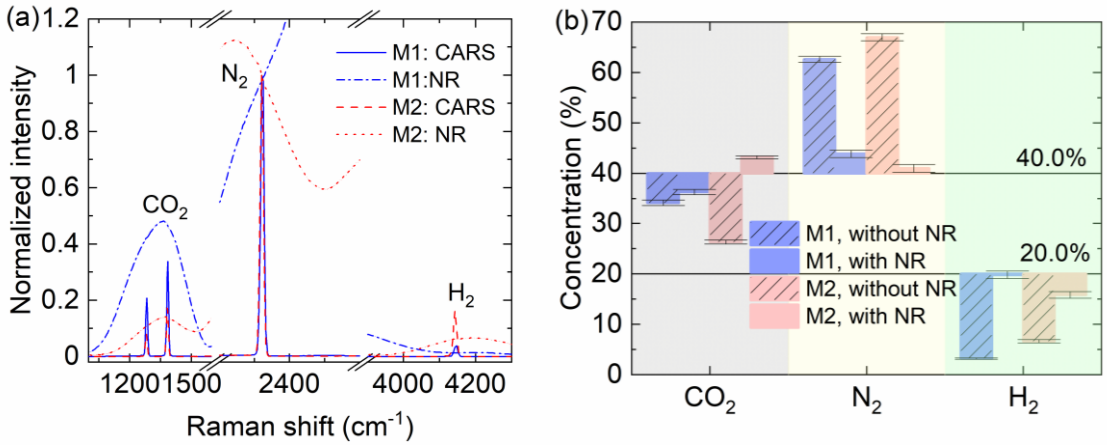

Fig. 6.8 (a) CARS signals in a gas mixture of 40% CO_2, 40% N_2, and 20% H_2 at ~2.1 ps delay with the nonresonant spectra measured in pure argon at zero delay at 1.7 bar and room temperature. For comparability reason, the signals are all normalized to the signal strength at the Raman shift of N_2 (~2330 cm^{-1}). (b) Concentration measurements with and without considering the nonresonant response for M1and M2 for two different pump/Stokes spectra at 1.7 bar and room temperature. The bars show the averaged results from 5 CARS spectra at probe pulse delays of ~1-3 ps.

To study the influence of the nonresonant spectral referencing for molecules with even larger Raman shifts, similar concentration measurements were carried out in gas mixtures of 40% CO_2, 40% N_2 and 20% H_2 at 295 K and 1.7 bar. Fig. 6.8 (a) shows the CARS spectra and the corresponding nonresonant spectra for two different spectral conditions. Similarly, for both M1 and M2, the concentration measurement results are shown and compared in Fig. 6.8 (b). The spectral referencing from the nonresonant responses correct the measurement results largely close to the set values. However, if we compare Fig. 6.8 (b) with Fig. 6.7 (b), it is noticed that the measurement accuracies for CO_2-N_2-H_2 gas mixtures are in general lower than those for the CO_2-N_2-CH_4 mixtures. We attribute the results to the significantly larger Raman shift of H_2 (~4161 cm^{-1}). For this reason, the excitation of H_2 may only be addressed by the contributions from the wings of the pump/Stokes spectrum, thus may be less stable compared to the molecules excited by contributions from the main components of the spectrum. In addition, when H_2 is involved, as shown in Fig. 6.8 (a), it is quite challenging to obtain similar excitation efficiencies for all the molecules and

referencing the excitation efficiency from the nonresonant response becomes essentially necessary. However, for concentration measurements with molecules having Raman shifts below ~2330 cm^{-1} (see M2 in Fig. 6.7 (a)), the pump/Stokes spectrum may be adjusted to a condition, where similar excitation efficiencies are obtained for the probing species.

6.2.2 High-pressure concentration measurements

Here, we further explore concentration measurements under higher pressures. In the previous section we have seen that the nonresonant signal recorded in pure argon is sensitive to the pump/Stokes spectrum. Therefore, one can anticipate that the high-pressure induced spectral change at the probe volume may also be detectable and, thus, can be taken into account for quantitative measurements. To check the pressure effects on the excitation efficiencies, the nonresonant responses for different pressures were studied.

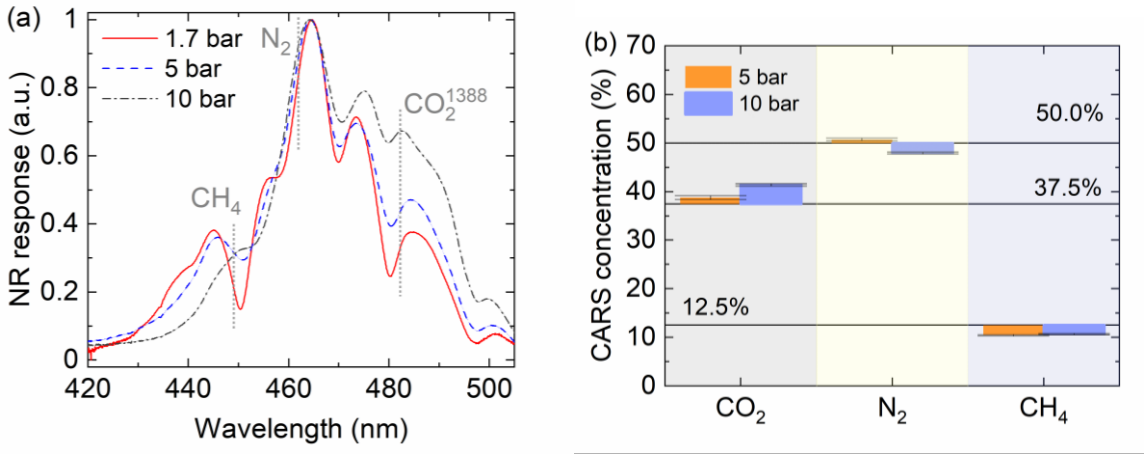

Fig. 6.9 (a) Nonresonant responses in argon at zero delay measured at 1.7 bar, 5 bar, and 10 bar at room temperature. The light grey dotted lines indicate the positions of the Raman shifts for CH_4, N_2 and the peak at 1388 cm^{-1} of the first Fermi polyad of CO_2. (b) Concentration measurement results in a gas mixture of 37.5% CO_2, 50% N_2, and 12.5% CH_4 at 5 bar and 10 bar and at a temperature of 295 K. The data points show the averaged results from 5 CARS spectra at 1-3 ps delay. Error bars show the standard deviations. Black lines indicate the concentrations expected from the settings of the mass flow controllers.

Fig. 6.9 (a) shows one example of the nonresonant responses in pure argon at 1.7 bar, 5 bar and 10 bar. The spectral broadening effects can be observed at the peak centered at around 464 nm, indicating that the pump/Stokes pulse is presumably subject to SPM [Gu2019]. In addition, more significant changes for the strength of the nonresonant response occur in the

region close to the CO_2 vibrational frequencies (marked as CO_2^{1388}). Smaller changes occur at the relevant regions for N_2 and CH_4 CARS. Nevertheless, the overall change of the nonresonant profile will give rise to different excitation efficiencies for the target molecules. Considering the excitation efficiencies estimated from the nonresonant argon signals, the concentration measurements at 5 bar and 10 bar were also studied in a gas mixture of CO_2, N_2, and CH_4. Fig. 6.9 (b) shows the concentration results determined by CARS. Comparing with the 1.7 bar results (with NR) shown in Fig. 6.7 (b), a larger degradation of the accuracy for CO_2 is observed compared to N_2 and CH_4 as the pressure increases to 10 bar. This may be explained by the pressure-dependent nonresonant response behavior discussed in Fig. 6.9 (a). The nonresonant response change at the frequency of CO_2 is more pronounced compared to that of CH_4 or N_2. Note that the estimation of the excitation efficiencies is implemented in pure argon which does not have the same optical properties as the target gas. Therefore, the error caused by changing the gas from the actual composition (CO_2, N_2, CH_4) to argon may be larger for CO_2.

In-situ spectral referencing of the nonresonant response from the target gas mixtures would be required to address the above-mentioned issues. However, this is currently challenging for ultrabroadband CARS. As discussed in the beginning of this section, in-situ spectral referencing that has been implemented in ns-CARS are based on different polarization properties of the resonant and the nonresonant signals [Farrow1985]. However, the resonant CARS signal or the nonresonant background signal usually experience considerable loss accompanying the polarization techniques [Eckbreth1981]. For this reason, it was claimed that this technique is not feasible for broadband implementations [Farrow1985]. Another challenge is to ensure the same alignment for both the resonant and the nonresonant signals into the detection systems. In addition, for applications in closed reaction chamber, polarization-sensitive technique may fail due to the pressure-induced birefringence in the optical window [Roy2002, Roy2010a]. Therefore, current fs-laser-based CARS techniques mainly rely on a separate spectral referencing in a Raman inactive medium, e.g. argon. Further investigations are needed for ultrabroadband techniques in order to achieve efficient and reliable in-situ spectral referencing.

7 Coal gasification measurements

The previous measurements implemented in the gas oven with controlled temperature and gas flows were performed in order to determine the accuracy and precision of the two-beam ultrabroadband CARS technique under different probing conditions. This provides the preconditions for the study of practical dynamic processes. In this Chapter, the focus of the investigations is on coal gasification processes. Based on the two-beam ultrabroadband CARS technique, the temperature as well as the CO concentration evolution during the coal conversion process are investigated. In Section 7.1, the experimental preparation for the coal gasification investigations is discussed. The concentration determination of minor CO is studied. In Section 7.2, the in-situ investigation of the coal gasification process is performed using ultrabroadband CARS. Results at different pressures are analyzed and compared, in addition, the measurements for a single coal particle are shown.

7.1 Preparation for coal gasification investigations using ultrabroadband CARS

7.1.1 Preparation for Boudouard reaction

As introduced in Section 2.7, the products of coal gasification highly depend on the gas composition. Multiple reactions involving oxygen, hydrogen, water, carbon monoxide, and carbon dioxide may occur (see Equations (2.24)-(2.27)). As our focus is the Boudouard reaction (Equation (2.27)), to ensure a pure CO_2 atmosphere, the oven was evacuated with a vacuum pump for a few hours to remove air and humidity. This is crucial because the humidity and oxygen in air may enable different reaction paths (see Equation (2.24) and (2.26)) at temperatures below the reaction temperatures for the Boudouard reaction. In order to ensure the absence of water and oxygen, the oven was then filled with pure 200 ml/min N_2 to 1.4 bar and heated up to ~1300 K. The position of the laser beams were adjusted

aforehand according to Fig. 4.7, and the crucible was filled with the lignite coke powder (see Section 4.3). Under this inert atmosphere no reaction should take place. During the entire heating process, the CARS spectrum was monitored. As shown in Fig. 7.1, up to ~1268 K, there is no CO detected from the CARS spectrum, meaning coal was not reacting with oxygen or water left in the atmosphere. Then the pure N_2 gas flow was changed to a gas mixture of 100 ml/min N_2 and 100 ml/min CO_2. After about 15 minutes the CO_2 concentration was high enough for the formation of CO as confirmed by the additional peak in the CARS spectrum at ~2143 cm^{-1}. Despite the fact that the atmosphere in the oven was still dominated by N_2 (compare the CARS signals of N_2 and CO_2 in Fig. 7.1), the Boudouard reaction and therefore the coal gasification towards CO formation can be confirmed. The aforementioned procedure to remove oxygen (from air) and water was proved to be sufficient. As the next step we performed the same experiment mainly under a pure CO_2 atmosphere, i.e. without N_2 to have the maximum CO_2 concentration for maximum gasification.

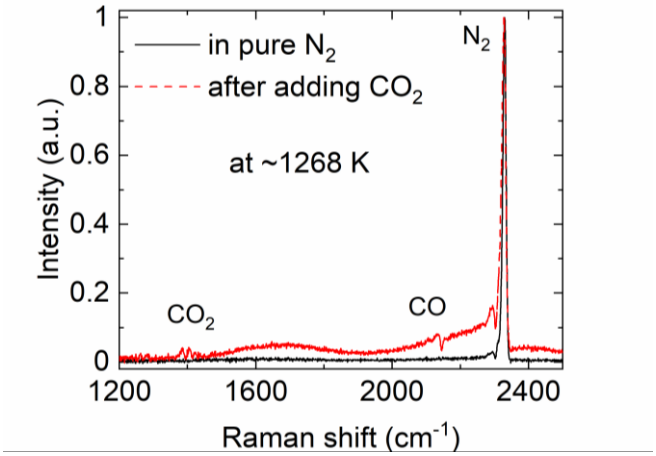

Fig. 7.1 Comparison between the CARS spectrum measured in a pure 200 ml/min N_2 flow and the one measured after changing the gas mixture to 100 ml/min N_2 and 100 ml/min CO_2 for 15 minutes at ~1268 K and 1.4 bar.

The coal gasification in general starts at a relatively high temperature of ~1000 K, and the most extensive conversion is expected above ~1300 K [Irfan2011, Küster2017]. To achieve the highest possible carbon conversion, the gas oven thus needs to be heated up to ~1300 K. As discussed in Section 4.3 and Fig. 4.8, 1.4 bar is mainly considered for coal gasification measurements in this thesis, because a compromise between the heating ability of the oven and a sufficient CO_2 density is required. Nevertheless, coal gasification at 2.8 bar (Section

7.2.1) was also implemented to compare the results under different conditions.

Fig. 7.2 shows the measured CARS spectra during the gasification process for the lignite coke powder at 1.4 bar and under 300 ml/min pure CO_2 flow. The recorded CO CARS peak starts to appear at a temperature of ~1023 K, although with a modulated spectral shape. To monitor the generated CO concentration at the lowest possible temperature, it should be noted that it is better to focus on the CARS spectra at probe delays where the nonresonant signal is still present (Fig. 6.5). In addition, the coal powder volume is much smaller compared to the volume of the gas oven, and the measurement is implemented within a continuous supply of CO_2. Therefore, the converted CO density is much smaller compared to the CO_2 density in the probing environment [Küster2017]. This is confirmed in Fig. 7.2, where the CO signal at 1323 K is still quite small compared to the CO_2 signal intensity. In addition, the dephasing decay of the CO CARS signal leads to a merging into the background if a relatively long probe delay is applied. For coal gasification at the early stage (low temperatures <1100 K), the evolution of the CO content will thus be hard to be detectable at the probe delays, where the nonresonant signal is fully eliminated. Therefore, for the investigation of the coal gasification process, we have to use short probe delays and to consider the modulation dip corresponding to the nonresonant background for minor species concentration measurement (Section 3.3). The details will be explained and illustrated in the following section.

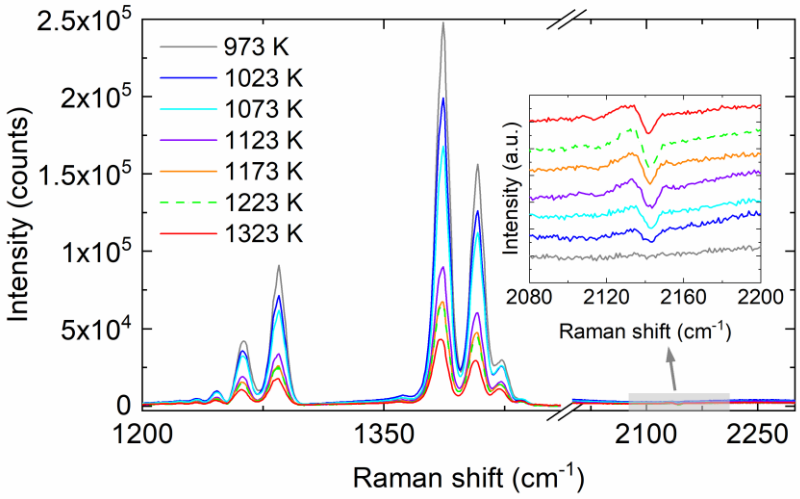

Fig. 7.2 Ultrabroadband CARS spectra measured at ~1.6 ps probe delay during the coke powder gasification process at temperatures from 973 K to 1323 K and a pressure of ~1.4 bar. The CO CARS signals are enlarged in the inset, which are shifted vertically for better visibility.

7.1.2 Minor CO determination in CO_2 atmosphere

This section intends to investigate minor CO determination for monitoring the Boudouard reaction as discussed in the previous section. Using the modulation dips of the nonresonant background (Section 3.3), Hahn et al. [Hahn1993] have proved the validity of the minor species determination in an argon atmosphere. They then extended this method to the CO concentration determination in a CH_4/air premixed flame. It was reported that the modulation dip to the nonresonant background is unique to each experimental condition and can change depending on various parameters including the laser bandwidth and the slit function of the detection system. As visible from Equations (3.21) and (3.22), also the error of the linewidth adds uncertainties to the modulation dip. Therefore, targeting on minor CO determination during gasification processes, we calibrated this method for our ultrabroadband CARS setup by introducing an additional scaling factor M for Equation (3.21). The value of M was determined by fitting the calculated modulation dips as a function of the CO concentration with the experimental results. The measurements were performed at 295 K in a CO_2 abundant atmosphere with CO concentration varied from 1% down to 0.1%. As the CARS signal exhibits its maximum intensity at a probe delay of ~1.5 ps (see Fig. 6.1), we focus on this delay for the minor concentration analysis. The experimental CARS spectra close to the CO resonance are normalized to the nonresonant signal measured in pure CO_2 at a similar delay to retrieve the modulated CARS spectra. One example of the measured CARS spectrum for 0.25% CO in CO_2 is shown in Fig. 7.3 (a). The nonresonant background measured in pure CO_2 in the same spectral range is displayed in Fig. 7.3 (b).

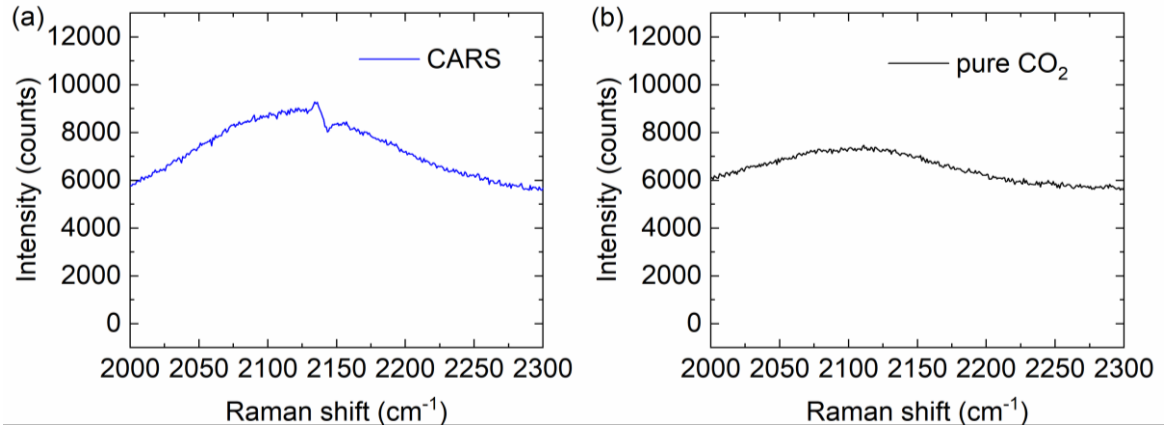

Fig. 7.3 (a) Ultrabroadband CARS signal of 0.25% CO in CO_2 at ~1.5 ps probe delay and at a temperature of 295 K and a pressure of 1.4 bar. (b) Nonresonant background measured in pure CO_2 at ~1.5 ps, 295 K and 1.4 bar.

The CO CARS spectra normalized by the nonresonant spectra from pure CO_2 are shown in Fig. 7.4 (a), where the CO concentration varies from 1% down to 0.1%. Taking small fluctuations of the background intensity into account, the CARS spectra are all normalized at ~2120 cm^{-1}. Based on this, the modulation dip (denoted as I_M) divided by the background intensity (I_B is taken from the average value at the Raman shifts of ~2120 cm^{-1} and ~2160 cm^{-1}) of the CARS spectrum is calculated. The results of I_M/I_B from Fig. 7.4 (a) are shown with red circles in Fig. 7.4 (b). By applying the least square fitting, the best-fit calculated modulation dips are obtained and the curve is shown in Fig. 7.4 (b). In this way, the unique scaling factor *M* as well as the relation between the CARS modulation dips with the minor CO concentration using our ultrabroadband CARS setup are calibrated.

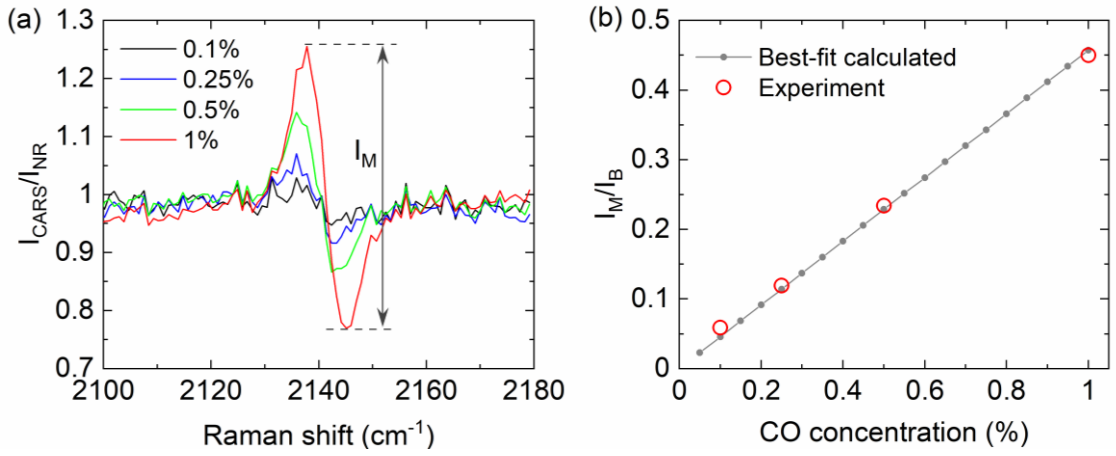

Fig. 7.4 (a) Normalized CO CARS spectra for CO concentrations from 1% to 0.1% at a probe delay of ~1.5 ps, 295 K, 1.4 bar. I_M denotes the modulation dip for the CO CARS spectrum with 1% concentration. (b) Best-fit calculated modulation dips to the nonresonant background with the experimental results at 295 K and 1.4 bar.

Based on this, the modulation dips to the nonresonant background at higher temperatures are calculated. Fig. 7.5 (a) shows the results of 0-5% CO in CO_2 atmosphere at 1000-1300 K, which is the most interesting temperature range in coal gasification. At a fixed temperature, the CO modulation dip increases almost linearly with the CO concentration, but at a much smaller slope compared to the room temperature results (Fig. 7.4(b)). For a fixed CO concentration, the modulation dip decreases as the temperature increases. Overall, the modulation dip is shown to be sensitive to both temperature and concentration. To retrieve the CO concentration easily from its modulation dip of the nonresonant background, one may need to obtain a general expression for the CO determination [Hahn1993]. In this

regard, numerical calculations of the modulation dip as a function of the temperature for different CO concentrations are performed and shown in Fig. 7.5 (b). The results at temperatures of 300-1500 K for CO concentrations from 0.2% to 5.0% are displayed (data points), showing similar trends as reported by Hahn et al. [Hahn1993]. At a fixed CO concentration, the modulation dip decreases exponentially with increasing temperature. These calculated results can also be fit with third-order exponential functions. The solid lines give the results after least square fitting of these data with a function in the form of

$$\frac{I_M}{I_B} = exp\left(p_3 T^3 + p_2 T^2 + p_1 T + p_0\right). \tag{7.1}$$

The values of the fitting coefficients $p_{0,1,2,3}$ are shown in Table. 7.1. It is observed that $p_{1,2,3}$ are linearly related to the CO concentration σ while p_0 is found to have a cubic relation to σ. By fitting the values of the $p_{0,1,2,3}$ coefficients given in Table. 7.1 at different CO concentrations, the expressions for $p_{0,1,2,3}$ with regard to the CO concentration are obtained and shown in Equations (7.2) - (7.5).

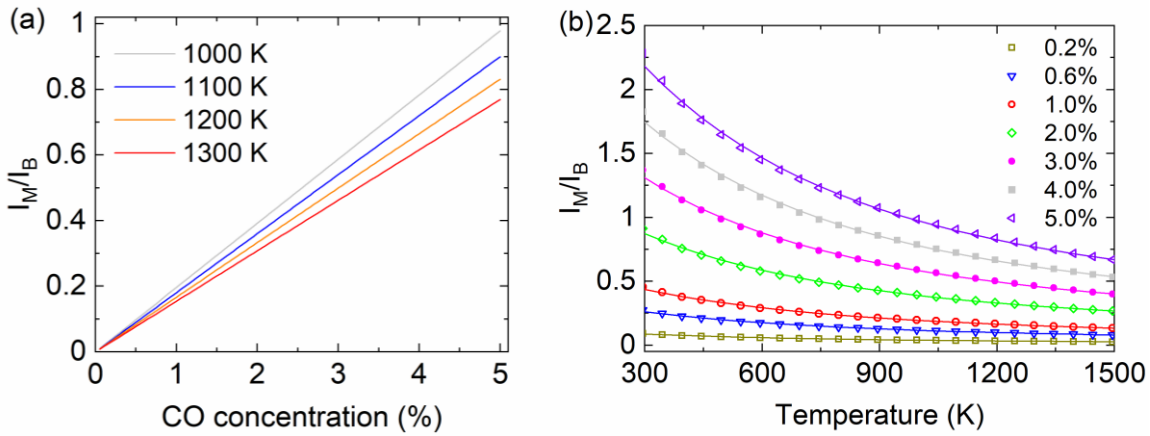

Fig. 7.5 (a) Calculated modulation dip as a function of the CO concentration in CO_2 at 1000 K, 1100 K, 1200 K and 1300 K, 1.4 bar. (b) Calculated modulation dip (data points) to the nonresonant background as a function of temperature for different CO concentrations in CO_2. The solid lines show the results of the best-fit curves from the least square fitting.

The deduced Equations (7.1)-(7.5) are then used for the low CO concentration analysis for coal gasification investigations which will be discussed in the following section.

Table. 7.1 Fitting coefficients for the calculated CO modulation dip in the CO_2 atmosphere as a function of temperature for different CO concentrations.

CO concentration/%	p_3 $(\times 10^{-11})$	p_2 $(\times 10^{-7})$	p_1 $(\times 10^{-3})$	p_0
0.2	-9.75970	6.11073	-1.81302	-1.94731
0.6	-9.75974	6.11076	-1.81303	-0.84870
1.0	-9.75978	6.11079	-1.81304	-0.33788
2.0	-9.75988	6.11087	-1.81306	0.35524
3.0	-9.75998	6.11094	-1.81309	0.76069
4.0	-9.76007	6.11102	-1.81311	1.04836
5.0	-9.76017	6.11109	-1.81313	1.27148

$$p_3 = -9.706539 \times 10^{-14}\sigma - 9.759685 \times 10^{-11} \tag{7.2}$$

$$p_2 = 7.495269 \times 10^{-10}\sigma + 6.110717 \times 10^{-7} \tag{7.3}$$

$$p_1 = -2.333385 \times 10^{-6}\sigma - 1.813018 \times 10^{-3} \tag{7.4}$$

$$p_0 = 54811.11\sigma^3 - 5732.575\sigma^2 + 218.9019\sigma - 2.103675 \tag{7.5}$$

7.2 In-situ temperature and concentration measurements

7.2.1 Coal powder gasification

The coal gasification processes were first performed using the lignite coke powder with 300 ml/min CO_2 flow at 1.4 bar. The oven temperature was set to ~1400 K and the temperature started to increase with a heating rate of ~10 K/min as shown in Fig. 4.8. Afterwards, the CARS spectra at ~5 different probe delays in the range of ~1-4 ps were recorded when the oven temperature reached a certain value (from ~973 K up to ~1323 K). At each delay, 20 acquisitions were accumulated with an acquisition time of 50 ms, resulting in a total acquisition time of 1 s for each CARS spectrum. The time interval between the successive recordings at different delays was typically ~30 s. Thus, the acquisition time for all CARS spectra recorded at each temperature span over ~2 minutes. Accordingly, the oven

temperature as well as the measured CARS temperature have an uncertainty of ~20 K according to the heating rate of the oven (~10 K/min).

The investigations of the temperature and the CO concentration at the probe volume were performed using the following procedures: (1) Since the temperature information is needed for the determination of low concentrations as described in the previous section, it was first determined from 5 background corrected CO_2 CARS spectra at probe delays of ~1-4 ps. (2) The background corrected CO CARS spectra at ~1.5 ps were normalized by the nonresonant background spectra at the same delay measured in pure CO_2 when the reaction has not started (e.g. at room temperature). (3) The modulation dips of the CO CARS signals were extracted from the normalized spectra and they were then used for the CO concentration determination.

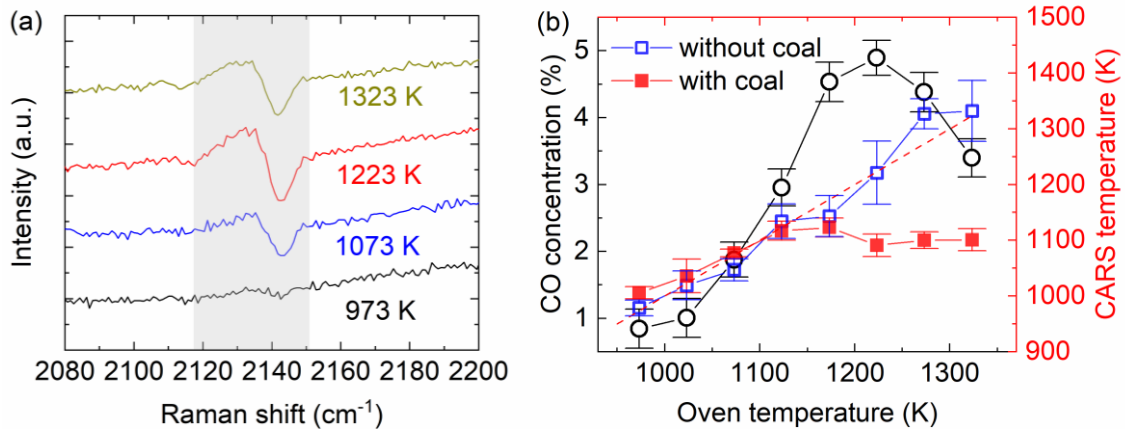

Fig. 7.6 (a) CO CARS spectra measured during the heating of the lignite coke powder coal gasification process at 1.4 bar. The spectra are shifted vertically for better visibility. The spectral region, where the CO signal is supposed to appear, is marked in grey. (b) Measured temperatures and CO concentrations as a function of the oven temperatures. The heating rate is controlled to be ~10 K/min. The CO concentrations determined from the modulation dips of the nonresonant background are calculated based on temperatures determined from the CARS measurements (red data points). The red dashed line shows a reference of the oven temperatures measured with the thermocouple. The results of the reference temperature measurements without coal inside the crucible are displayed in blue.

Fig. 7.6 (a) shows the CO CARS signals at different oven temperatures during the heating process. The temperature and concentration measurement results are shown in Fig. 7.6 (b). The red data points show the average of the temperatures determined from 5 CO_2 CARS spectra as a function of the oven temperatures, with the error bars displaying the standard

deviations. CO concentrations are extracted based on Equations (7.1)-(7.5) from the modulation dips of the nonresonant background using the measured CARS temperatures (red). The error bars for the CO concentrations (black) are derived from the spectral signal to noise ratio. The determined CO concentrations show that the carbon conversion starts after the oven temperature reaches ~1000 K. On the other hand, the measured temperatures are in very good agreement and increase linearly with the set oven temperatures up to ~1123 K. At around 1200 K the temperature determined from the CO_2 CARS signals does not seem to follow the set temperature of the oven and reaches a plateau. Clearly, the coal conversion has fully started and CO is generated at a maximum rate. The temperature plateau is considered due to the endothermic nature of the Boudouard reaction, which becomes predominant in the probing region. A similar temperature decrease close to the coal in a level of ~300 K was reported in an entrained flow coal gasifier [Watanabe2006]. For comparison, temperature measurements with the coal crucible inside the oven but without coal powders were performed. The corresponding temperatures determined from CARS are displayed in blue in Fig. 7.6 (b). There, the measured temperature follows the increase of the oven temperature over the entire range, which confirms that the temperature plateau is induced by coal gasification.

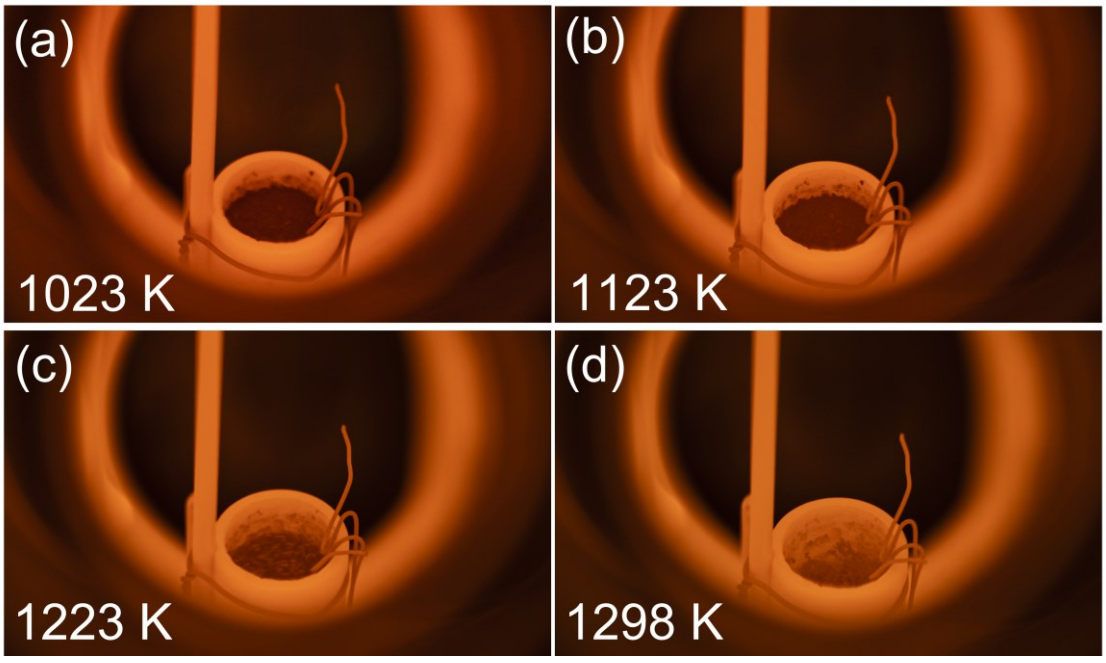

Fig. 7.7 Images taken during the lignite coke powder gasification process at (a) 1023 K, (b) 1123 K, (c) 1223 K, and (d) 1298 K at 1.4 bar.

After the CO concentration reaches its maximum value at ~1223 K, the CO concentration

starts to decrease. This is also confirmed by the CO CARS spectrum at 1323 K shown in Fig. 7.6 (a). The measured CO concentration evolution is in accordance with the optically observed amount of coal powder in the crucible that has been recorded by a camera (Sony Alpha 7III) using a 135 mm lens (Samyang F/2.0) with a macro extension tube. The camera was placed in front of the upper oven window to ensure a good visibility for the coal powder during the gasification process.

Fig. 7.7 shows several recorded representative images of the coal powder states at 1023 K, 1123 K, 1223 K and 1298 K. At 1023 K, a small modulation dip close to ~2143 cm^{-1} in the CARS spectrum appears (see Fig. 7.6), indicating the start of the gasification process. By comparing the images at 1023 K and 1123 K, no obvious carbon consumption is observed although there is an increase of the modulation dip (Fig. 7.6 (b)). After the temperature is further increased to ~1223 K, a clear difference of the coal powder between Fig. 7.7 (b) and (c) is observed. Correspondingly, a significant increase of the CO CARS modulation dip is measured (Fig. 7.6), showing evidence that the Boudouard reaction is fully activated. The measured CO concentration around this temperature (see Fig. 7.6 (b)) is maximal and the temperature determined by CARS starts to stay almost unchanged at this point. The significant powder reduction visible in Fig. 7.7 (c) may be the explanation for this. Afterwards, Fig. 7.7 (d) shows the state of the coal powder when the temperature has further increased to ~1298 K. The upper layer of the coal powder is mostly consumed while the distance between the detection point and the residual reactive powder is increasing. The CO concentration is sensitive to the distance with regard to the coal reactive center and decreases as the distance increases [An2021]. This observation is directly reflected by the decreasing trend of the CO concentration determined by CARS at temperatures beyond ~1250 K.

For comparison, the coal gasification for lignite coke powder was also investigated at an elevated pressure of 2.8 bar with highly reduced heating rate at ~1000-1200 K (see Fig. 4.8). Fig. 7.8 (a) shows the CO CARS spectra measured in pure CO_2 at 973 K, 1073 K, 1173 K and 1238 K. As with the measurements implemented at 1.4 bar, the temperatures were first determined from 5 CO_2 CARS spectra at probe delays of ~1-4 ps. The CO concentrations were then determined from the CO CARS modulation dip of the nonresonant background. The results as a function of the oven temperatures are shown in Fig. 7.8 (b).

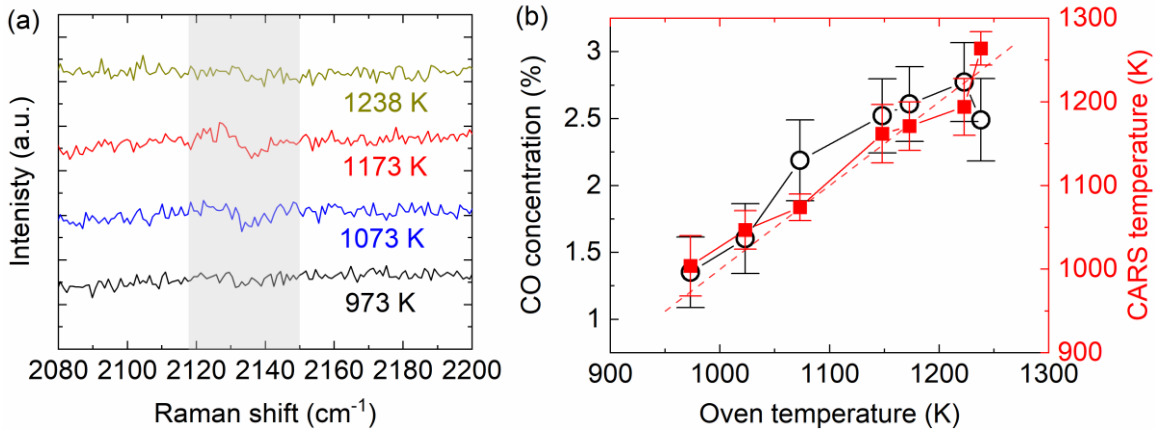

Fig. 7.8 (a) CO CARS spectra measured in pure CO_2 at 2.8 bar. The spectra are shifted vertically for better visibility. The spectral region, where the CO signal is supposed to appear, is marked in grey. (b) Temperatures and CO concentrations determined by CARS signals during the heating process of the oven in the coal gasification measurements at 2.8 bar. The red dashed line shows a reference of the oven temperatures measured from the thermocouple.

The CO signal barely starts to appear at ~1073 K (Fig. 7.8 (a)) but only with a very small SNR. At ~1200 K, the CO CARS signal maximizes. Afterwards, a moderate decreasing trend is shown. Over the entire temperature range (973-1238 K), the measured CO concentration (~2.7% at the maximum) remains below the level that is measured at 1.4 bar (~4.9% at the maximum). The measured temperatures, in contrast to the coal gasification measurements at 1.4 bar, follow the oven temperature and do not show a clear plateau at a certain oven temperature. Note that the highest temperature achieved at 2.8 bar is ~150 K lower than that at 1.4 bar. The heating rate at 2.8 bar that is given in Fig. 4.8 (b) shows a significant drop beyond 1000 K already. This may disturb the gasification process and hinder it from full activation, which could be an explanation for the small CO signal. In addition, as for the measured temperature, the doubled CO_2 density at 2.8 bar doubles the heat capacity compared to the 1.4 bar case, which reduces influences on the temperature from the (not-fully-started) coal gasification reaction.

Besides, after the gasification process and the cooling of the oven, the coal holder was taken out to check the coal powder state, as shown in Fig. 7.9. Apart from the upper layer that has been consumed and left with only the solid ash layers, there was still an unreacted layer of coal powders (black powder) left at the bottom of the coal holder, which also proved that the gasification process at 2.8 bar was not fully activated and was limited by the heating ability and presumably also the heating rate.

Fig. 7.9 The coal powder state after the gasification measurements implemented at 2.8 bar.

7.2.2 Single coal particle gasification

As introduced in Section 2.7, industrial gasifiers are typically fed with coal particles [Küster2017]. Therefore, the coal gasification and the measurement ability were also investigated using lignite coke particles. To make sure that the coal particles have sufficient reaction surface and placed at a similar height with respect to the laser beams, a spiral wire structure (see Fig. 7.10 (a)) was built for hanging the coal particles close to the top of the ceramic coal crucible. The coal particles typically have a size of ~2-3 mm in diameter. In the following, we show the results when a single lignite coke particle was placed in the coal crucible for the gasification investigations.

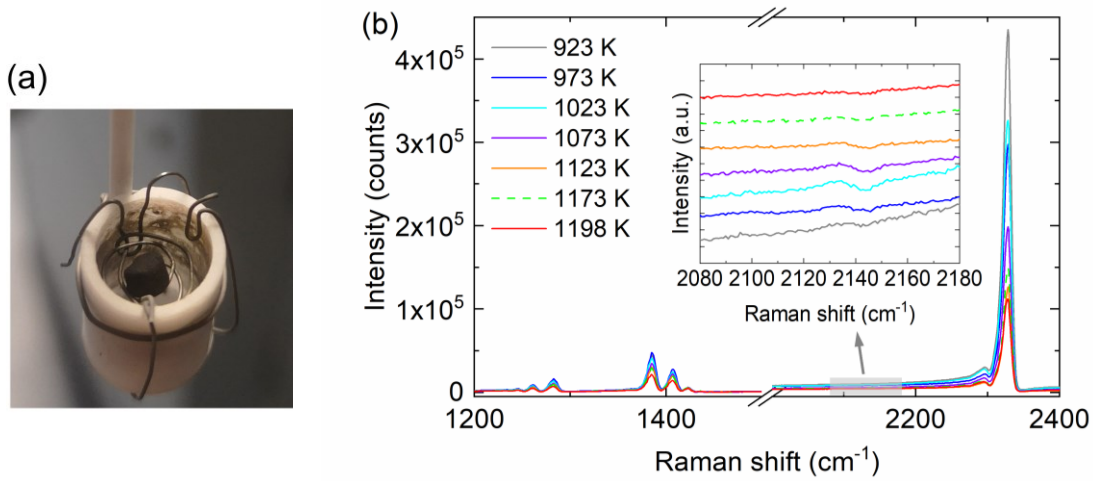

Fig. 7.10 (a) Spiral wire structure for hanging the coal particles for gasification measurements. (b) CARS spectra at ~1.5 ps probe delay measured during the heating of the gasification process using a single lignite coke particle at 1.4 bar. The inset shows the spectra close to the CO resonance, which are shifted vertically for better visibility. The legends indicates the oven temperatures measured with the thermocouple.

The measurements were performed at 1.4 bar with a constant flow of 300 ml/min CO_2 and 300 ml/N_2. The calculated nonresonant susceptibility is 10.07×10^{-18} cm^3/(erg·amagat) for this atmosphere, while the nonresonant susceptibilities of CO_2 and N_2 are 12.02×10^{-18} cm^3/(erg·amagat) and 8.11×10^{-18} cm^3/(erg·amagat), respectively [Hahn1995]. Following the same procedure as explained in Section 7.1.2 to deduce the fitting coefficients for Equation (7.1), we can extract the CO concentration in the current gas flow. Fig. 7.10 (b) shows the measured CARS spectra during the heating process of the oven with an inset enlarging the spectral region of ~2080-2180 cm^{-1}. A clear evolution of the generated CO CARS signals is visible for the single coal particle.

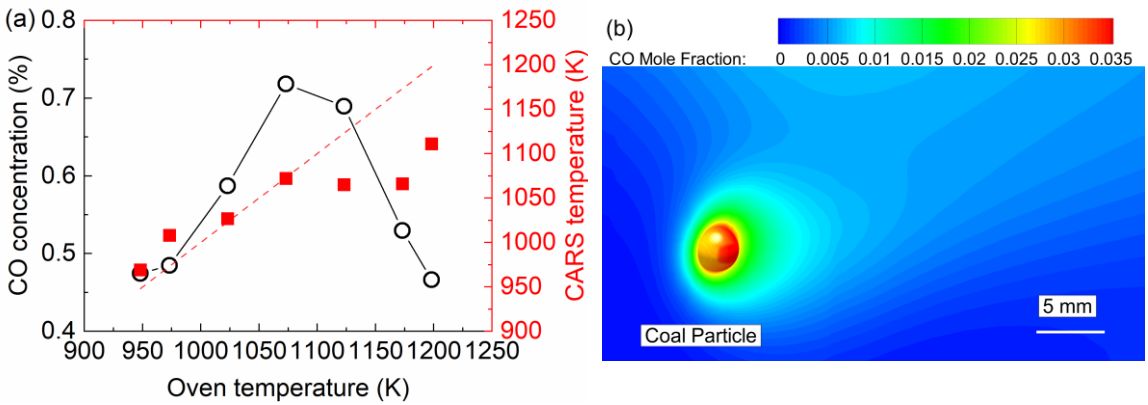

Fig. 7.11 (a) Temperature and CO concentration measurements for the in-situ single coal particle gasification investigation at 1.4 bar. (b) Simulated CO concentration distribution around a coal particle with a diameter of 3 mm at ~1100 K and 1.2 bar in a CO_2 atmosphere [An2021] (with permission from the authors).

To reduce temperature errors from the heating process, CARS spectra at only two probe delays were recorded at each temperature. The one at ~2.3 ps was used for the temperature determination and the one at ~1.5 ps was utilized to extract the CO concentration. The measured temperatures as well as the CO concentrations from the modulation dip of the nonresonant background during the oven heating process for a single coal particle are shown in Fig. 7.11 (a). Similar to the 1.4 bar measurements in lignite coke powder (Fig. 7.6), the measured temperature also reaches a plateau when the oven temperature is beyond 1100 K. Similarly, the carbon conversion rate is shown to peak between 1050 K and 1150 K. At higher temperatures, the CO concentration drops again, because the coal particle is consumed. At ~1200 K, nearly the entire coal particle is converted (see Fig. 7.12 (d)) and correspondingly an increasing of the temperature is observed. For comparison, Fig. 7.11 (b)

shows a simulated CO distribution surrounding a coal particle during the gasification process at ~1100 K, 1.2 bar. The particle considered for the simulation has a similar size (3 mm in diameter) as used here. More details of this figure are discussed in [An2021]. Notably, the CO concentration level at ~2 mm above the coal particle is comparable to the measured CO concentration as displayed in Fig. 7.11 (a).

The lignite coke particle in the crucible was also examined by a camera, and Fig. 7.12 shows the images of 4 coal particles during the heating process of the oven. Like the images of the coal powder (see Fig. 7.7), no obvious reaction can be observed from the coal state when the oven temperature is below 1000 K. After the oven is heated beyond this level, the reaction and the changes of the coal particles are clearly captured (see Fig. 7.12 (b) and (c)). The measured CO concentration from a single coal particle (Fig. 7.11) is also shown to reach its maximum level around this temperature. At ~1200 K, the solid ash layer of the coal particles is clearly observed (Fig. 7.12 (d)), indicating a complete consumption of the particle. This is also in accordance with the decrease of the CO concentration and the increase of the temperature after it reaches a plateau as shown in Fig. 7.11 (a).

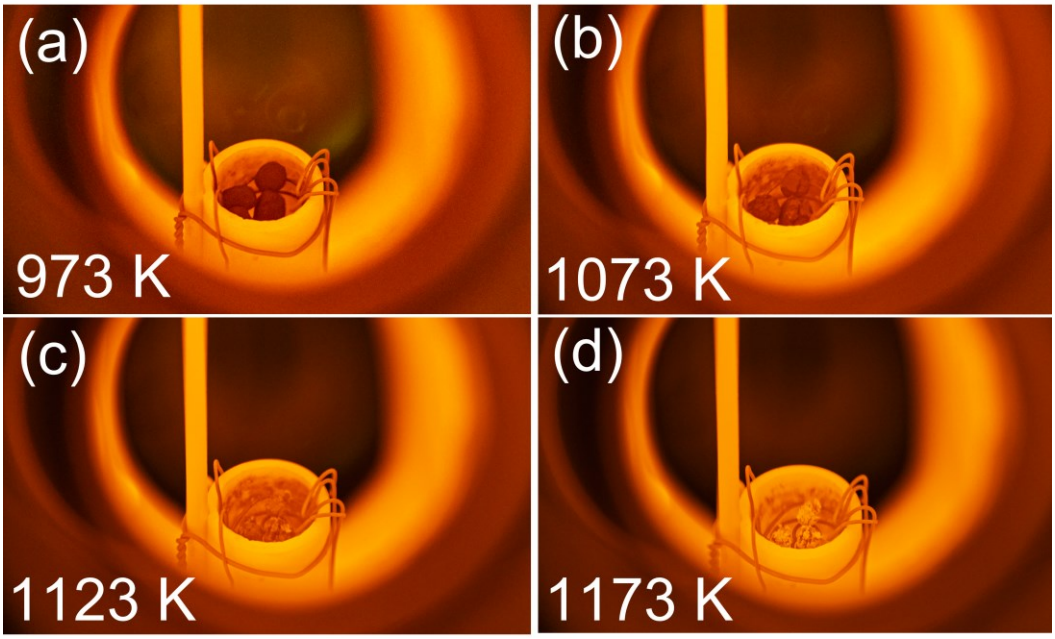

Fig. 7.12 Images taken during the gasification process of four lignite coke particles at (a) 973 K, (b) 1073 K, (c) 1123 K, and (d) 1173 K at 1.4 bar.

For all coal gasification measurements shown above, the lowest measurable CO concentration seems to be ~0.7% at ~1100 K in the single coal particle gasification measurements, indicating the detection limit of this technique. With sufficiently high

heating abilities, these results prove the capability of the in-situ coal gasification measurements, even for a single coal particle using the ultrabroadband CARS technique.

8 Conclusions and outlook

The aim of this work was to investigate and extend the capability of the ultrabroadband CARS technique for temperature and concentration measurements for multiple species and a wide range of practical applications, especially for gasification diagnostics. Practical gasification or combustion devices mainly work under high pressures. Therefore, a sufficiently short probe pulse (~2 ps) was utilized for collision-free measurements. In order to simultaneously excite multiple gas species with Raman shifts up to ~4200 cm^{-1}, a ~7 fs pump/Stokes beam was used. Both beams are generated by a 200 kHz BBO-based OPCPA system. Based on this configuration, the experimental methods and the theoretical framework for temperature and concentration determination were developed. The accuracy and precision of this technique was at first determined in a gas oven with controlled temperatures and gas flows. In this way, temperature measurements at temperatures from 295 K up to ~1300 K were performed with excellent accuracies within ~4%. The CO detection limit in CO_2 atmosphere was extended to 0.5% at room temperature and 2% at 1073 K at a pressure of 1.4 bar. Temperature and concentration measurements were further extended to 20 bar and 10 bar, respectively. The influence of the ultrabroadband spectrum on the excitation efficiencies was investigated in detail. Subsequently, ultrabroadband CARS technique was applied for the first time for coal gasification investigations. Successful CARS analytical results were obtained even for the gasification process of a single coal particle.

The capability of temperature and concentration determination from multiple species was also proved and studied in detail using the ultrabroadband CARS technique in this thesis. Thermometry was successfully implemented using multiple species. Depending on the molecular properties, temperature information was extracted either from a single CARS spectrum (e.g. CO_2 and H_2) or from the decay of the time-resolved CARS signals (e.g. N_2). Special attention has been paid on CO_2 using its first two Fermi polyads for the spectral fitting. The performance of temperature measurements using difference probing species has

been compared in the perspective of accuracy and temporal resolution. The temperature measurements were not only carried out at a pressure below 2 bar but also performed up to ~20 bar with good accuracies, proving that our ultrabroadband CARS technique is collision-free up to this pressure level. These results demonstrate the feasibility of implementing this technique for practical applications under high pressures.

Covering the most relevant gasification or combustion species, concentration measurements were investigated in different binary or ternary gas mixtures. CO concentration in CO_2/N_2 was determined down to 0.5% at 295 K and to 2% at 1073 K. The quantified influence of the spectral referencing measured from pure argon was investigated in detail especially for $CO_2/N_2/CH_4(H_2)$ gas mixtures. In addition, the concentration measurements were also extended up to ~10 bar. The pressure induced change on the excitation efficiencies for various molecules were found to be different, therefore affecting the accuracies of the determined concentrations. Improving the accuracy of high-pressure concentration measurements further would require the in-situ spectral referencing from the same gas mixture, which is currently quite challenging for the ultrabroadband CARS technique.

Based on the temperature and concentration measurements under controlled gas flows, this technique was applied for the first time for the in-situ investigation of the coal gasification processes. Using the modulation dips of the nonresonant background, we calibrated the minor CO concentration determination using our system. Based on this, the detection limit of CO in CO_2 was further extended to 0.1% at 295 K. The coal gasification using lignite coke powders and a single coal particle was then investigated. The measured temperature and concentration results captured the energy conversion process as well as the endothermic phenomenon. The CO detection limit was further extended to ~0.7% at ~1100 K during the gasification measurements of a single coal particle.

In the future, we are planning to adapt a spatial light modulator [Oron2002b, Vacano2008] in the beam path of the sub-10 fs pump/Stokes pulses to study in detail the spectral phase influence on the CARS signal for different species. It is anticipated to achieve a certain level of coherent control of the CARS spectrum for different applications. In addition, we are planning to extend this technique to a remote sensing scale by using filamentation [Zhao2020], which is of particular interest for industrial applications. Coal gasification measurements with different gas composition (Section 2.7) and sources are also of great interest for the further investigations.

Bibliography

[Aldén1986] M. Aldén, P.-E. Bengtsson, and H. Edner, "Rotational CARS generation through a multiple four-color interaction," Applied Optics **25**, 4493 (1986).

[Allan2001] M. Allan, "Selectivity in the excitation of fermi-coupled vibrations in CO_2 by impact of slow electrons," Physical Review Letters **87**, 033201 (2001).

[An2021] F. An, F. Küster, R. Ackermann, S. Guhl, and A. Richter, "Heat and mass transfer analysis of a high-pressure TGA with defined gas flow for single-particle studies," Chemical Engineering Journal **411**, 128503 (2021).

[Ariunbold2016a] G. O. Ariunbold, and N. Altangerel, "Coherent anti-Stokes Raman spectroscopy: Understanding the essentials," Coherent Optical Phenomena **3**, 6 (2016a).

[Ariunbold2016b] G. O. Ariunbold, and N. Altangerel, "Quantitative interpretation of time-resolved coherent anti-Stokes Raman spectroscopy with all Gaussian pulses," Journal of Raman Spectroscopy **48**, 104 (2016b).

[Atkins2006] P. Atkins, and J. d. Paula, *Physical Chemistry* (Oxford University Press, 2006).

[Bekerom2018] D. C. M. v. d. Bekerom, J. M. P. Linares, E. M. v. Veldhuizen, S. Nijdam, M. C. M. v. d. Sanden, and G. J. v. Rooij, "How the alternating degeneracy in rotational Raman spectra of CO_2 and C_2H_2 reveals the vibrational temperature," Applied Optics **57**, 5694 (2018).

[Bell2011] D. A. Bell, B. F. Towler, and M. Fan, *Coal Gasification and its Applications* (Elsevier, 2011).

[Böhle2014] F. Böhle, M. Kretschmar, A. Jullien, M. Kovacs, M. Miranda, R. Romero, H. Crespo, U. Morgner, P. Simon, R. Lopez-Martens, and T. Nagy, "Compression of CEP-stable multi-mJ laser pulses down to 4 fs in long hollow fibers," Laser Physics Letters **11**, 095401 (2014).

[Bohlin2013] A. Bohlin, and C. J. Kliewer, "Communication: two-dimensional gas-phase coherent anti-Stokes Raman spectroscopy (2D-CARS): simultaneous planar imaging and multiplex spectroscopy in a single laser shot," Journal of Chemical Physics **138**, 221101 (2013).

[Bohlin2014a] A. Bohlin, and C. J. Kliewer, "Single-shot hyperspectral coherent Raman planar imaging in the range 0–4200 cm^{-1}," Applied Physics Letters **105**, 161111 (2014a).

[Bohlin2014b] A. Bohlin, and C. J. Kliewer, "Two-beam ultrabroadband coherent anti-Stokes Raman spectroscopy for high resolution gas-phase multiplex imaging," Applied Physics Letters **104**, 031107 (2014b).

[Bohlin2017] A. Bohlin, C. Jainski, B. D. Patterson, A. Dreizler, and C. J. Kliewer, "Multiparameter spatio-thermochemical probing of flame–wall interactions advanced with coherent Raman imaging," Proceedings of the Combustion Institute **36**, 4557 (2017).

[Boyd2008] R. W. Boyd, *Nonlinear optics* (Elsevier Acad. Press, 2008).

[Brackmann2002] C. Brackmann, J. Bood, P.-E. Bengtsson, T. Seeger, M. Schenk, and A. Leipertz, "Simultaneous vibrational and pure rotational coherent anti-Stokes Raman spectroscopy for temperature and multispecies concentration measurements demonstrated in sooting flames," Applied Optics **41**, 564 (2002).

[Chedin1979] A. Chedin, "The carbon dioxide molecule: Potential, spectroscopic, and molecular constants from its infrared spectrum," Journal of Molecular Spectroscopy **76**, 430 (1979).

[Courtney2017] T. L. Courtney, A. Bohlin, B. D. Patterson, and C. J. Kliewer, "Pure-rotational H_2 thermometry by ultrabroadband coherent anti-Stokes Raman spectroscopy," J. Chem. Phys. **146**, 224202 (2017).

[DeKock1989] R. L. DeKock, and H. B. Gray, *Chemical Structure and Bonding* (University Science Books, 1989).

[Demtröder2006] W. Demtröder, *Atoms, Molecules and Photons* (Springer, 2006).

[Dennis2016] C. N. Dennis, C. D. Slabaugh, I. G. Boxx, W. Meier, and R. P. Lucht, "5 kHz thermometry in a swirl-stabilized gas turbine model combustor using chirped probe pulse femtosecond CARS. Part 1: Temporally resolved swirl-flame thermometry," Combustion and Flame **173**, 441 (2016).

[Dudovich2002] N. Dudovich, D. Oron, and Y. Silberberg, "Single-pulse coherently controlled nonlinear Raman spectroscopy and microscopy," Nature **418**, 512 (2002).

[Eckbreth1978] A. C. Eckbreth, "BOXCARS: Crossed-beam phase-matched CARS generation in gases," Applied Physics Letters **32**, 421 (1978).

[Eckbreth1981] A. C. Eckbreth, and R. J. Hall, "CARS Concentration Sensitivity With and Without Nonresonant Background Suppression," Combustion Science and Technology **25**, 175 (1981).

[Eckbreth1985] A. C. Eckbreth, and T. J. Anderson, "Dual broadband CARS for simultaneous, multiple species measurements," Applied Optics **24**, 2731 (1985).

[Eckbreth1996] A. C. Eckbreth, *Laser diagnostics for combustion temperature and species* (Gordon & Breach, 1996).

[Ewart1985] P. Ewart, "A modeless, variable bandwidth, tunable laser," Optics Communications **55**, 124 (1985).

[Farrow1985] R. L. Farrow, R. P. Lucht, G. L. Clark, and R. E. Palmer, "Species concentration measurements using CARS with nonresonant susceptibility normalization," Applied Optics **24**, 2241 (1985).

[Femtometer2008] *User's manual for Dispersion Minimized Autocorrelator*, Femtolasers productions GmbH (2008).

[Fermi1931] E. Fermi, "Über den Ramaneffekt des Kohlendioxyds," Zeitschrift für Physik **71**, 250 (1931).

[Finsterhölzl1982] H. Finsterhölzl, "Raman Spectra of Carbon Dioxide and Its Isotopic Variants in the Fermi Resonance Region: Part III. Analysis of Rovibrational Intensities for $^{12}C1^{6}O_2$, $^{13}C^{16}O_2$, $^{12}C^{18}O_2$ and $^{12}C^{16}O^{18}O$," Berichte der Bunsengesellschaft für physikalische Chemie **86**, 797 (1982).

[Fischer2003] J. Fischer, R. R. Gamache, A. Goldman, L. S. Rothman, and A. Perrin, "Total internal partition sums for molecular species in the 2000 edition of the HITRAN database," Journal of Quantitative Spectroscopy and Radiative Transfer **82**, 401 (2003).

[Gallmann2006] L. Gallmann, T. Pfeifer, P. M. Nagel, M. J. Abel, D. M. Neumark, and S. R. Leone, "Comparison of the filamentation and the hollow-core fiber characteristics for pulse compression into the few-cycle regime," Applied Physics B **86**, 561 (2006).

[Gamache1990] R. R. Gamache, R. L. Hawkins, and L. S. Rothman, "Total internal partition sums in the temperature range 70–3000 K: Atmospheric linear molecules," Journal of Molecular Spectroscopy **142**, 205 (1990).

[Gamache2017] R. R. Gamache, C. Roller, E. Lopes, I. E. Gordon, L. S. Rothman, O. L. Polyansky, N. F. Zobov, A. A. Kyuberis, J. Tennyson, S. N. Yurchenko, A. G. Császár, T. Furtenbacher, X. Huang, D. W. Schwenke, T. J. Lee, B. J. Drouin, S. A. Tashkun, V. I. Perevalov, and R. V. Kochanov, "Total internal partition sums for 166 isotopologues of 51 molecules important in planetary atmospheres: Application to HITRAN2016 and beyond," Journal of Quantitative Spectroscopy and Radiative Transfer **203**, 70 (2017).

[Greenhalgh1985] D. A. Greenhalgh, and S. T. Whittley, "Mode noise in broadband CARS spectroscopy," Applied Optics **24**, 907 (1985).

[Gu2019] M. Gu, A. Satija, and R. P. Lucht, "Effects of self-phase modulation (SPM) on femtosecond coherent anti-Stokes Raman scattering spectroscopy," Optics Express **27** (2019).

[Gu2020] M. Gu, A. Satija, and R. P. Lucht, "CO_2 chirped-probe-pulse femtosecond CARS thermometry," Proceedings of the Combustion Institute (2020).

[Hahn1993] J. W. Hahn, S. N. Park, E. S. Lee, C. Rhee, K. T. Kang, S. H. Chung, C. Y. Choi, and Y. D. Huh, "Measuring the Concentration of Minor Species from the Modulation Dip of the Nonresonant Background of Broad-Band CARS Spectra," Applied Spectroscopy **47**, 710 (1993).

[Hahn1995] J. W. Hahn, and E. S. Lee, "Measurement of nonresonant third-order susceptibilities of various gases by the nonlinear interferometric technique," Journal of the Optical Society of America B **12**, 1021 (1995).

[Hahn1997] J. W. Hahn, C. W. Park, and S. N. Park, "Broadband coherent anti-Stokes Raman spectroscopy with a modeless dye laser," Applied Optics **36**, 6722 (1997).

[Hall1980] R. J. Hall, J. F. Verdieck, and A. C. Eckbreth, "Pressure-induced narrowing of the cars spectrum of N_2," Optics Communications **35**, 69 (1980).

[Hancock1997] R. D. Hancock, K. E. Bertagnolli, and R. P. Lucht, "Nitrogen and hydrogen CARS temperature measurements in a hydrogen/air flame using a near-adiabatic flat-flame burner," Combustion and Flame **109**, 323 (1997).

[Herman1996]I. P. Herman, *Optical Diagnostics for Thin Film Processing* (Elsevier Inc. , 1996).

[Hertel2015] I. V. Hertel, and C.-P. Schulz, *Atoms, Molecules and Optical Physics 2* (Springer, 2015).

[Herzberg1945] G. Herzberg, *Molecular spectra and molecular structure. Vol.2: Infrared and Raman spectra of polyatomic molecules* (Princeton: D Van Nostrand, 1945).

[Herzberg1950] G. Herzberg, *Molecular spectra and molecular structure. Vol.1: Spectra of diatomic molecules* (1950).

[Higman2014]C. Higman, and S. Tam, "Advances in coal gasification, hydrogenation, and gas treating for the production of chemicals and fuels," Chemical Reviews **114**, 1673 (2014).

[Hunt2013] J. Hunt, A. Ferrari, A. Lita, M. Crosswhite, B. Ashley, and A. E. Stiegman, "Microwave-Specific Enhancement of the Carbon–Carbon Dioxide (Boudouard) Reaction," The Journal of Physical Chemistry C **117**, 26871 (2013).

[Irfan2011] M. F. Irfan, M. R. Usman, and K. Kusakabe, "Coal gasification in CO_2 atmosphere and its kinetics since 1948: A brief review," Energy **36**, 12 (2011).

[Joly1999] V. Joly, and A. Roblin, "Vibrational relaxation of CO_2 (m, nl, p) in a CO_2-N_2 mixture. Part 1: Survey of available data," Aerospace Science and Technology **3**,

229 (1999).

[Jourdanneau2005] E. Jourdanneau, F. Chaussard, R. Saint-Loup, T. Gabard, and H. Berger, "The methane Raman spectrum from 1200 to 5500cm^{-1}: A first step toward temperature diagnostic using methane as a probe molecule in combustion systems," Journal of Molecular Spectroscopy **233**, 219 (2005).

[Kajitani2002]S. Kajitani, S. Hara, and H. Matsuda, "Gasification rate analysis of coal char with a pressurized drop tube furnace," Fuel **81**, 539 (2002).

[Kamga1980] F. M. Kamga, and M. G. Sceats, "Pulse-sequenced coherent anti-Stokes Raman scattering spectroscopy: a method for suppression of the nonresonant background," Optics Letters **5**, 126 (1980).

[Kearney2013] S. P. Kearney, D. J. Scoglietti, and C. J. Kliewer, "Hybrid femtosecond/picosecond rotational coherent anti-Stokes Raman scattering temperature and concentration measurements using two different picosecond-duration probes," Optics Express **21**, 12327 (2013).

[Kearney2015] S. P. Kearney, and P. M. Danehy, "Pressure measurements using hybrid femtosecond/picosecond rotational coherent anti-Stokes Raman scattering," Optics Letters **40**, 4082 (2015).

[Kerstan2017] M. Kerstan, I. Makos, S. Nolte, A. Tünnermann, and R. Ackermann, "Two-beam femtosecond coherent anti-Stokes Raman scattering for thermometry on CO_2," Applied Physics Letters **110**, 021116 (2017).

[Kliewer2011]C. J. Kliewer, Y. Gao, T. Seeger, J. Kiefer, B. D. Patterson, and T. B. Settersten, "Picosecond time-resolved pure-rotational coherent anti-Stokes Raman spectroscopy in sooting flames," Proceedings of the Combustion Institute **33**, 831 (2011).

[Kliewer2012]C. J. Kliewer, A. Bohlin, E. Nordström, B. D. Patterson, P. E. Bengtsson, and T. B. Settersten, "Time-domain measurements of S-branch N_2–N_2 Raman linewidths using picosecond pure rotational coherent anti-Stokes Raman spectroscopy," Applied Physics B **108**, 419 (2012).

[Knopp2002] G. Knopp, P. Beaud, P. Radi, M. Tulej, B. Bougie, D. Cannavo, and T. Gerber, "Pressure-dependent N_2 Q-branch fs-CARS measurements," Journal of Raman Spectroscopy **33**, 861 (2002).

[Kozlov1979] D. N. Kozlov, A. M. Prokhorov, and V. V. Smirnov, "The methane ν1(a1) vibrational state rotational structure obtained from high-resolution CARS-spectra of the Q-branch," Journal of Molecular Spectroscopy **77**, 21 (1979).

[Krupenie1966] P. H. Krupenie, "The Band Spectrum of Carbon Monoxide," N. S. R. D. Series, ed. (1966).

[Kuehner2003] J. P. Kuehner, M. A. Woodmansee, R. P. Lucht, and J. C. Dutton, "High-resolution broadband N_2 coherent anti-Stokes Raman spectroscopy: comparison of measurements for conventional and modeless broadband dye lasers," Applied Optics **42**, 6757 (2003).

[Kulatilaka2010] W. D. Kulatilaka, J. R. Gord, and S. Roy, "Effects of O_2–CO_2 polarization beating on femtosecond coherent anti-Stokes Raman scattering (fs-CARS) spectroscopy of O_2," Applied Physics B **102**, 141 (2010).

[Küster2017] F. Küster, P. Nikrityuk, M. Junghanns, S. Nolte, A. Tünnermann, R. Ackermann, A. Richter, S. Guhl, and B. Meyer, "In-situ investigation of single particle gasification in a defined gas flow applying TGA with optical measurements," Fuel **194**, 544 (2017).

[Laher1991] R. R. Laher, and F. R. Gilmore, "Improved Fits for the Vibrational and Rotational Constants of Many States of Nitrogen and Oxygen," Journal of Physical and Chemical Reference Data **20**, 685 (1991).

[Lahijani2015] P. Lahijani, Z. A. Zainal, M. Mohammadi, and A. R. Mohamed, "Conversion of the greenhouse gas CO_2 to the fuel gas CO via the Boudouard reaction: A review," Renewable and Sustainable Energy Reviews **41**, 615 (2015).

[Lang1999] T. Lang, K.-L. Kompa, and M. Motzkus, "Femtosecond CARS on H_2," Chemical Physics Letters **310**, 65 (1999).

[Lang2002] T. Lang, and M. Motzkus, "Single-shot femtosecond coherent anti-Stokes Raman-scattering thermometry," Journal of the Optical Society of America B **19**, 340 (2002).

[Laurendeau1988] N. M. Laurendeau, "Temperature measurements by light-scattering methods," Progress in Energy and Combustion Science **14**, 147 (1988).

[Long2002] D. A. Long, *The Raman Effect: A Unified Treatment of the Theory* (John Wiley & Sons, Ltd, 2002).

[Lucht1987] R. P. Lucht, "Three-laser coherent anti-Stokes Raman scattering measurements of two species," Optics Letters **12**, 78 (1987).

[Lucht2006] R. P. Lucht, S. Roy, T. R. Meyer, and J. R. Gord, "Femtosecond coherent anti-Stokes Raman scattering measurement of gas temperatures from frequency-spread dephasing of the Raman coherence," Applied Physics Letters **89**, 251112 (2006).

[Lucht2007] R. P. Lucht, "Femtosecond Lasers for Molecular Measurements," Science **316**, 207 (2007).

[Marrocco2009a] M. Marrocco, "Comparative analysis of Herman-Wallis factors for uses in coherent anti-Stokes Raman spectra of light molecules," Journal of Raman Spectroscopy **40**, 741 (2009a).

[Marrocco2009b] M. Marrocco, "Herman–Wallis factor to improve thermometric accuracy of vibrational coherent anti-Stokes Raman spectra of H_2," Proceedings of the Combustion Institute **32**, 863 (2009b).

[Marrocco2011] M. Marrocco, "Herman-Wallis correction in vibrational CARS of oxygen," Journal of Raman Spectroscopy **42**, 1836 (2011).

[Mellqvist1996] J. Mellqvist, and A. Rosén, "DOAS for flue gas monitoring—I. Temperature effects in the U.V./visible absorption spectra of NO, NO_2, SO_2 and NH_3," Journal of Quantitative Spectroscopy and Radiative Transfer **56**, 187 (1996).

[Meshulach1999] D. Meshulach, and Y. Silberberg, "Coherent quantum control of multiphoton transitions by shaped ultrashort optical pulses," Physical Review A **60**, 1287 (1999).

[Meyer2007] T. R. Meyer, S. Roy, and J. R. Gord, "Improving Signal-to-Interference Ratio in Rich Hydrocarbon–Air Flames Using Picosecond Coherent Anti-Stokes Raman Scattering," Applied Spectroscopy **61**, 1135 (2007).

[Miller2010] J. D. Miller, M. N. Slipchenko, T. R. Meyer, H. U. Stauffer, and J. R. Gord, "Hybrid femtosecond/picosecond coherent anti-Stokes Raman scattering for high-speed gas-phase thermometry," Optics Letters **35**, 2430 (2010).

[Miller2011a] J. D. Miller, M. N. Slipchenko, and T. R. Meyer, "Probe-pulse optimization for nonresonant suppression in hybrid fs/ps coherent anti-Stokes Raman scattering at high temperature," Optics Express **19**, 13326 (2011a).

[Miller2011b] J. D. Miller, S. Roy, M. N. Slipchenko, J. R. Gord, and T. R. Meyer, "Single-shot gas-phase thermometry using pure-rotational hybrid femtosecond/picosecond coherent anti-Stokes Raman scattering," Optics Express **19**, 15627 (2011b).

[Miller2012] J. D. Miller, C. E. Dedic, S. Roy, J. R. Gord, and T. R. Meyer, "Interference-free gas-phase thermometry at elevated pressure using hybrid femtosecond/picosecond rotational coherent anti-Stokes Raman scattering," Optics Express **20**, 5003 (2012).

[Moya1975] F. Moya, S. A. J. Druet, and J. P. E. Taran, "Gas spectroscopy and temperature measurement by coherent Raman anti-stokes scattering," Optics Communications **13**, 169 (1975).

[Nibler1979] J. W. Nibler, and G. V. Knighten, *Coherent Anti-Stokes Raman Spectroscopy* (Springer, Berlin, Heidelberg, 1979).

[Nisoli1996] M. Nisoli, S. De Silvestri, and O. Svelto, "Generation of high energy 10 fs pulses by a new pulse compression technique," Applied Physics Letters **68**, 2793 (1996).

[Nordström2015] E. Nordström, A. Hosseinnia, C. Brackmann, J. Bood, and P.-E. Bengtsson, "Raman linewidth measurements using time-resolved hybrid picosecond/nanosecond rotational CARS," Optics Letters **40**, 5718 (2015).

[Oron2002a] D. Oron, N. Dudovich, D. Yelin, and Y. Silberberg, "Narrow-band coherent anti-stokes Raman signals from broad-band pulses," Physical Review Letters **88**, 063004 (2002a).

[Oron2002b] D. Oron, N. Dudovich, D. Yelin, and Y. Silberberg, "Quantum control of coherent anti-Stokes Raman processes," Physical Review A **65** (2002b).

[Pealat1985] M. Pealat, P. Bouchardy, M. Lefebvre, and J.-P. Taran, "Precision of multiplex CARS temperature measurements," Applied Optics **24**, 1012 (1985).

[Penney1972] C. M. Penney, L. M. Goldman, and M. Lapp, "Raman Scattering Cross Sections," Nature Physical Science **235**, 110 (1972).

[Pestov2007] D. Pestov, R. K. Murawski, G. O. Ariunbold, X. Wang, M. C. Zhi, A. V. Sokolov, V. A. Sautenkov, Y. V. Rostovtsev, A. Dogariu, Y. Huang, and M. O. Scully, "Optimizing the laser-pulse configuration for coherent Raman spectroscopy," Science **316**, 265 (2007).

[Pestov2008a] D. Pestov, W. Xi, D. Cristancho, K. R. Hall, A. V. Sokolov, and M. O. Scully, "Real-time sensing of gas phase mixtures via coherent Raman spectroscopy," in *Conference on Lasers and Electro-Optics and Conference on Quantum Electronics and Laser Science*(2008a), pp. 1-2.

[Pestov2008b] D. Pestov, X. Wang, G. O. Ariunbold, R. K. Murawski, V. A. Sautenkov, A. Dogariu, A. V. Sokolov, and M. O. Scully, "Single-shot detection of bacterial endospores via coherent Raman spectroscopy," PNAS **105**, 2 (2008b).

[Polack2005] T. Polack, D. Oron, and Y. Silberberg, "Control and measurement of a non-resonant Raman wavepacket using a single ultrashort pulse," Chemical Physics **318**, 163 (2005).

[Prince2006] B. D. Prince, A. Chakraborty, B. M. Prince, and H. U. Stauffer, "Development of simultaneous frequency- and time-resolved coherent anti-Stokes Raman scattering for ultrafast detection of molecular Raman spectra," Journal of Chemical Physics **125**, 44502 (2006).

[Rahn1979] L. A. Rahn, L. J. Zych, and P. L. Mattern, "Background-free cars studies of carbon monoxide in a flame," Optics Communications **30**, 249 (1979).

[Regnier1974] P. R. Regnier, F. Moya, and J. P. E. Taran, "Gas Concentration Measurement by Coherent Raman Anti-Stokes Scattering," AIAA Journal **12**, 826 (1974).

[Richardson2011] D. R. Richardson, R. P. Lucht, W. D. Kulatilaka, S. Roy, and J. R. Gord, "Theoretical modeling of single-laser-shot, chirped-probe-pulse femtosecond coherent anti-Stokes Raman scattering thermometry," Applied Physics B **104**, 699 (2011).

[Richardson2013] D. R. Richardson, R. P. Lucht, W. D. Kulatilaka, S. Roy, and J. R. Gord, "Chirped-probe-pulse femtosecond coherent anti-Stokes Raman scattering concentration measurements," Journal of the Optical Society of America B **30**, 188 (2013).

[Richardson2017] D. R. Richardson, H. U. Stauffer, S. Roy, and J. R. Gord, "Comparison of chirped-probe-pulse and hybrid femtosecond/picosecond coherent anti-Stokes Raman scattering for combustion thermometry," Applied Optics **56**, E37 (2017).

[Richet1977] P. Richet, Y. Battinga, and M. Javay, "A review of hydrogen, carbon, nitrogen, oxgen, sulphur, and chlorine stable isotope fractionation among gaseous molecules," Annual Review of Earth and Planetary Sciences **5**, 65 (1977).

[Roh1976] W. B. Roh, P. W. Schreiber, and J. P. E. Taran, "Single-pulse coherent anti-Stokes Raman scattering," Applied Physics Letters **29**, 174 (1976).

[Rosasco1989] G. J. Rosasco, L. A. Rahn, W. S. Hurst, R. E. Palmer, and S. M. Dohne, "Measurement and prediction of Raman Q-branch line self-broadening coefficients for CO from 400 to 1500 K," The Journal of Chemical Physics **90**, 4059 (1989).

[Rothman1992] L. S. Rothman, R. L. Hawkins, R. B. Wattson, and R. R. Gamache, "Energy levels, intensities, and linewidths of atmospheric carbon dioxide bands," Journal of Quantitative Spectroscopy and Radiative Transfer **48**, 537 (1992).

[Roy2002] S. Roy, R. P. Lucht, and A. McIlroy, "Mid-infrared polarization spectroscopy of carbon dioxide," Applied Physics B: Lasers and Optics **75**, 875 (2002).

[Roy2003] S. Roy, T. R. Meyer, M. S. Brown, V. N. Velur, R. P. Lucht, and J. R. Gord, "Triple-pump coherent anti-Stokes Raman scattering (CARS): temperature and multiple-species concentration measurements in reacting flows," Optics Communications **224**, 131 (2003).

[Roy2004] S. Roy, T. R. Meyer, R. P. Lucht, M. Afzelius, P.-E. Bengtsson, and J. R. Gord, "Dual-pump dual-broadband coherent anti-Stokes Raman scattering in reacting flows," Optics Letters **29**, 1843 (2004).

[Roy2008] S. Roy, P. J. Kinnius, R. P. Lucht, and J. R. Gord, "Temperature measurements in reacting flows by time-resolved femtosecond coherent anti-Stokes Raman scattering (fs-CARS) spectroscopy," Optics Communications **281**, 319 (2008).

[Roy2009a] S. Roy, W. D. Kulatilaka, D. R. Richardson, R. P. Lucht, and J. R. Gord, "Gas-phase single-shot thermometry at 1 kHz using fs-CARS spectroscopy," Optics Letters **34**, 3857 (2009a).

[Roy2009b] S. Roy, P. Wrzesinski, D. Pestov, T. Gunaratne, M. Dantus, and J. R. Gord, "Single-beam coherent anti-Stokes Raman scattering spectroscopy of N_2 using a shaped 7 fs laser pulse," Applied Physics Letters **95**, 074102 (2009b).

[Roy2010a] S. Roy, J. R. Gord, and A. K. Patnaik, "Recent advances in coherent anti-Stokes Raman scattering spectroscopy: Fundamental developments and applications in reacting flows," Progress in Energy and Combustion Science **36**, 280 (2010a).

[Roy2010b] S. Roy, P. J. Wrzesinski, D. Pestov, M. Dantus, and J. R. Gord, "Single-beam coherent anti-Stokes Raman scattering (CARS) spectroscopy of gas-phase CO_2 via phase and polarization shaping of a broadband continuum," Journal of Raman Spectroscopy **41**, 1194 (2010b).

[Santagata2019] R. Santagata, M. Scherman, M. Toubeix, M. Nafa, B. Tretout, and A. Bresson, "Ultrafast background-free ro-vibrational fs/ps-CARS thermometry using an Yb:YAG crystal-fiber amplified probe," Optics Express **27**, 32924 (2019).

[Scherman2016] M. Scherman, M. Nafa, T. Schmid, A. Godard, A. Bresson, B. Attal-Tretout, and P. Joubert, "Rovibrational hybrid fs/ps CARS using a volume Bragg grating for N_2 thermometry," Optics Letters **41**, 488 (2016).

[Seeger2009] T. Seeger, J. Kiefer, A. Leipertz, B. D. Patterson, C. J. Kliewer, and T. B. Settersten, "Picosecond time-resolved pure-rotational coherent anti-Stokes Raman

spectroscopy for N_2 thermometry," Optics Letters **34**, 3755 (2009).

[Seeger2010] T. Seeger, J. Kiefer, Y. Gao, B. D. Patterson, C. J. Kliewer, and T. B. Settersten, "Suppression of Raman-resonant interferences in rotational coherent anti-Stokes Raman spectroscopy using time-delayed picosecond probe pulses," Optics Letters **35**, 2040 (2010).

[Slabaugh2016] C. D. Slabaugh, C. N. Dennis, I. Boxx, W. Meier, and R. P. Lucht, "5 kHz thermometry in a swirl-stabilized gas turbine model combustor using chirped probe pulse femtosecond CARS. Part 2. Analysis of swirl flame dynamics," Combustion and Flame **173**, 454 (2016).

[Snowdon1991] P. Snowdon, S. M. Skippon, and P. Ewart, "Improved precision of single-shot temperature measurements by broadband CARS by use of a modeless laser," Applied Optics **30**, 1008 (1991).

[Stauffer2018]H. U. Stauffer, K. A. Rahman, M. N. Slipchenko, S. Roy, J. R. Gord, and T. R. Meyer, "Interference-free hybrid fs/ps vibrational CARS thermometry in high-pressure flames," Optics Letters **43**, 4911 (2018).

[Struve1989] W. S. Struve, *Fundamentals of molecular spectroscopy* (John Wiley & Sons, Inc., 1989).

[Taamallah2015] S. Taamallah, K. Vogiatzaki, F. M. Alzahrani, E. M. A. Mokheimer, M. A. Habib, and A. F. Ghoniem, "Fuel flexibility, stability and emissions in premixed hydrogen-rich gas turbine combustion: Technology, fundamentals, and numerical simulations," Applied Energy **154**, 1020 (2015).

[Tejeda1995] G. Tejeda, B. Maté, and S. Montero, "Overtone Raman spectrum and molecular polarizability surface of CO_2," Journal of Chemical Physics **103**, 568 (1995).

[Vacano2008] B. v. Vacano, and M. Motzkus, "Time-resolving molecular vibration for microanalytics: single laser beam nonlinear Raman spectroscopy in simulation and experiment," Physical Chemistry Chemical Physics **10**, 681 (2008).

[Vestin2007a] F. Vestin, M. Afzelius, and P.-E. Bengtsson, "Development of rotational CARS for combustion diagnostics using a polarization approach," Proceedings of the Combustion Institute **31**, 833 (2007a).

[Vestin2007b] F. Vestin, M. Afzelius, H. Berger, F. Chaussard, R. Saint-Loup, and P. E. Bengtsson, "Rotational CARS thermometry at high temperature (1800 K) and high pressure (0.1–1.55 MPa)," Journal of Raman Spectroscopy **38**, 963 (2007b).

[Watanabe2006] H. Watanabe, and M. Otaka, "Numerical simulation of coal gasification in entrained flow coal gasifier," Fuel **85**, 1935 (2006).

[Weichert2016] S. Weichert, "Spectral Broadening of 25 fs Laser Pulses via Self-Phase Modulation in a Neon filled Hollow Core Fibre," (University of Hamburg, 2016).

[Wilson1935] E. B. Wilson, "The Statistical Weights of the Rotational Levels of Polyatomic Molecules, Including Methane, Ammonia, Benzene, Cyclopropane and Ethylene," The Journal of Chemical Physics **3**, 276 (1935).

[Woodmansee2002] M. A. Woodmansee, R. P. Lucht, and J. C. Dutton, "Stark Broadening and Stimulated Raman Pumping in High-Resolution N_2 Coherent Anti-Stokes Raman Scattering Spectra," AIAA Journal **40**, 1078 (2002).

[Wrzesinski2013] P. J. Wrzesinski, H. U. Stauffer, W. D. Kulatilaka, J. R. Gord, and S. Roy, "Time-resolved femtosecond CARS from 10 to 50 Bar: collisional sensitivity," Journal of Raman Spectroscopy **44**, 1344 (2013).

[Yagi2008] K. Yagi, S. Hirata, and K. Hirao, "Vibrational quasi-degenerate perturbation theory: applications to fermi resonance in CO_2, H_2CO, and C_6H_6," Physical Chemistry Chemical Physics **10**, 1781 (2008).

[Yip1992] B. Yip, P. M. Danehy, and R. K. Hanson, "Degenerate four-wave mixing temperature measurements in a flame," Optics Letters **17**, 751 (1992).

[Yu2007] Y. Yu, K. Lin, X. Zhou, H. Wang, S. Liu, and X. Ma, "Precise measurement of the depolarization ratio from photoacoustic Raman spectroscopy," Journal of Raman Spectroscopy **38**, 1206 (2007).

[Yuratich1977] M. A. Yuratich, and D. C. Hanna, "Coherent anti-Stokes Raman spectroscopy (CARS)," Molecular Physics **33**, 671 (1977).

[Zhao2020] X. Zhao, S. Nolte, and R. Ackermann, "Lasing of N_2^+ induced by filamentation in air as a probe for femtosecond coherent anti-Stokes Raman scattering," Optics Letters **45**, 3661 (2020).

[Zinth1980] W. Zinth, "Transient coherent Raman scattering in the time and frequency domain," Optics Communications **34**, 479 (1980).

[Zolin1998] A. Zolin, A. Jensen, L. S. Pedersen, K. Dam-Johansen, and P. Tørslev, "A Comparison of Coal Char Reactivity Determined from Thermogravimetric and Laminar Flow Reactor Experiments," Energy & Fuels **12**, 268 (1998).

Zusammenfassung

Ziel dieser Arbeit war es, die Ultrabreitband-CARS-Technik für Temperatur- und Konzentrationsmessungen in Gasen zu untersuchen und für praktische Anwendungen, insbesondere für die Vergasungsdiagnostik, zu evaluieren. Industrielle Vergasungs- oder Verbrennungsanlagen arbeiten hauptsächlich bei hohen Drücken. Daher wurde ein ausreichend kurzer Probepuls (~2 ps) für Messungen verwendet, die in diesem Zeitintervall frei von störenden Einflüssen von Molekülstößen sind. Um mehrere Gasspezies mit Raman-Verschiebungen bis zu ~4200 cm^{-1} gleichzeitig anzuregen, wurde ein ~7 fs Pump/Stokes-Strahl verwendet. Beide Strahlen wurden von einem 200 kHz BBO-basierten OPCPA-System erzeugt. Basierend auf dieser Konfiguration wurden die experimentellen Methoden und der theoretische Rahmen für die Temperatur- und Konzentrationsbestimmung entwickelt. Die Genauigkeit und Präzision dieser Technik wurde zunächst in einem Gasofen mit kontrollierten Temperaturen und Gasflüssen ermittelt. Auf diese Weise wurden Temperaturmessungen bei Temperaturen von 295 K bis ~1300 K mit ausgezeichneten Genauigkeiten innerhalb von ~4% durchgeführt. Die CO-Nachweisgrenze in CO_2-Atmosphäre wurde auf 0,5% bei Raumtemperatur und 2% bei 1073 K bei einem Druck von 1,4 bar verbessert. Die Temperatur- und Konzentrationsmessungen wurden bis auf 20 bar bzw. 10 bar erweitert. Der Einfluss des Ultrabreitbandspektrums auf die Anregungseffizienzen wurde im Detail untersucht. Anschließend wurde die Ultrabreitband-CARS-Technik zum ersten Mal für Untersuchungen zur Kohlevergasung eingesetzt. Erfolgreiche CARS-Analysen wurden darüber hinaus für den Vergasungsprozess eines einzelnen Kohlepartikels erzielt.

Für die Zukunft ist geplant, einen Pulsformer [Oron2002b, Vacano2008] im Strahlengang des sub-10 fs Pump/Stokes-Pulse zu implementieren, um den Einfluss der spektralen Phase auf das CARS-Signal für verschiedene Spezies im Detail zu untersuchen. Z.B. soll auf bestimmte Ramanübergänge im Pump/Stokes Spektrum optimiert werden, um das CARS Signal zu maximieren. Darüber hinaus planen wir, diese Technik mittels Filamentierung

[Zhao2020] auf größere räumliche Skalen zu erweitern, was insbesondere für industrielle Anwendungen interessant ist. Kohlevergasungsmessungen mit unterschiedlicher Gaszusammensetzung (Abschnitt 2.7) sowie die Erweiterung auf Reststoffe und Recyclingprodukte sind ebenfalls von großem Interesse für die weiteren Untersuchungen.

Acknowledgments

The study in Jena is a unique experience compared with any periods I have ever spent. Without the help and support from many people, this work could hardly come to success.

First of all, I would like to express my sincere gratitude to my supervisor Prof. Dr. Stefan Nolte for the opportunity to work in the Ultrafast Optics group and for the valuable guidance, insightful comments and constant help in my research and life.

I would like to express my deep gratitude to my supervisor Dr. Roland Ackermann for all the valuable discussions, suggestions and great support throughout my entire doctoral study. With generosity and patience, he never hesitates to answer my numerous questions and kindly leads me to the mysterious world of CARS!

I would like to thank Prof. Andreas Tünnermann for the opportunity of working at IAP.

I am very grateful to my 'spectroscopy' group, especially Dr. André Boden, Xiaodong Zhao, Dr. Thomas Gabler, Marcus Junghanns, Dr. Marita Kerstan, and Dr. Robert Kammel. Their generous support, patience and assistance help me through the way. It is my pleasure to work with you!

I would also like to thank all the other members in our Ultrafast Optics group, in particular Helena Kämmer, Dr. Daniel Richter, Thorsten Goebel, Dr. Qingfeng Li, Dr. Alessandro Alberucci, Christian Matzdorf and many more. The enjoyable working atmosphere, kind help and relaxing discussions in the coffee room or the lunch lounge are unforgettable.

I would like to thank all my friends both in Jena and far away. Thanks them for always listening to me, being behind me. They help me ease up the stress over the years and lead a healthy life.

I would like to thank my husband Chenhao Yang (杨晨昊), for supporting and understanding me all the way, for lifting me up when I was down and always reminding me what life is about.

I am grateful to my parents Hongbo Liu and Qixue Ran. Many thanks to them for supporting every decision I made and encouraging me to travel across the seas for studying and experiencing a different life.

我想感谢我的父母: 刘洪波和冉启学。谢谢他们支持我的每一个决定，鼓励我飘洋过海来学习和体会不一样的生活。

List of publications

Peer-reviewed journals

1. Y. Ran, M. Junghanns, A. Boden, S. Nolte, A. Tünnermann, and R. Ackermann, "Temperature and gas concentration measurements with vibrational ultra-broadband two-beam femtosecond/picosecond coherent anti-Stokes Raman scattering and spontaneous Raman scattering," Journal of Raman Spectroscopy **50**, 1268-1275 (2019).
2. Y. Ran, A. Boden, A. Richter, S. Guhl, S. Nolte, and R. Ackermann, "Nonresonant signal assisted high-pressure multi-species gas concentration measurements using ultrabroadband CARS," OSA Continuum **3**, 2036-2043 (2020).

Conference contributions

1. Y. Ran, M. Junghanns, M. Kerstan, S. Nolte, A. Tunnermann, and R. Ackermann, "Temperature and Gas Concentration Measurements with Two-beam Femtosecond Coherent Anti-Stokes Raman Scattering (fs-CARS) and Spontaneous Raman Scattering," ECONOS (2018).
2. Y. Ran, M. Kerstan, A. Tunnermann, S. Nolte, and R. Ackermann, "Femtosecond coherent anti-Stokes Raman scattering (fs-CARS) for temperature and concentration measurements on combustion species using a dual output OPCPA," EPJ Web of Conferences 205 (2019).
3. Y. Ran, S. Nolte, A. Tünnermann, and R. Ackermann, "Femtosecond Coherent Anti-Stokes Raman Scattering Measurement of Gas Temperature Simultaneously from H_2, N_2 and CO_2," in 2019 Conference on Lasers and Electro-Optics Europe & European Quantum Electronics Conference (CLEO/Europe-EQEC) (2019), pp. 1-1.
4. Y. Ran, S. Nolte, A. Tunnermann, and R. Ackermann, "Collision-free two-beam

ultrabroadband coherent anti-Stokes Raman scattering spectroscopy for high pressure thermometry," ECONOS (2019).

5. Y. Ran, S. Nolte, A. Tünnermann, and R. Ackermann, "Two-beam Ultrabroadband Coherent Anti-Stokes Raman Scattering Spectroscopy for Temperature and Concentration Measurements Using a Dual-output OPCPA," "714. WE-Heraeus-Seminar," (2020).
6. Y. Ran, S. Nolte, A. Tünnermann, and R. Ackermann, "Gas Concentration Measurements Based on Ultrabroadband Coherent Anti-Stokes Raman Scattering Using the Non-resonant Signal," presented at the Conference on Lasers and Electro-Optics, OSA Technical Digest (Optical Society of America) (2020).

Ehrenwörtliche Erklärung

Ich erkläre hiermit ehrenwörtlich, dass ich die vorliegende Arbeit selbständig und ohne unzulässige Hilfe Dritter sowie ohne Benutzung anderer als der angegebenen Hilfsmittel und Literatur angefertigt habe. Aus anderen Quellen direkt oder indirekt übernommene Daten, Bilder und Konzepte sind unter Angabe der Quellen eindeutig gekennzeichnet.

Bei der Auswahl und Auswertung folgenden Materials haben mir die nachstehend aufgeführten Personen in der jeweils beschriebenen Weise unentgeltlich geholfen:

1. André Boden: Kohlevergasungsexperimente, Shot-to-Shot Pump/Stokes-Spektrum-Messungen

Weitere Personen waren an der inhaltlich-materiellen Erstellung der vorliegenden Arbeit nicht beteiligt. Insbesondere habe ich hierfür nicht die entgeltliche Hilfe von Vermittlungs- bzw. Beratungsdiensten (Promotionsberater oder andere Personen) in Anspruch genommen.

Niemand hat von mir unmittelbar oder mittelbar geldwerte Leistungen für Arbeiten erhalten, die im Zusammenhang mit dem Inhalt der vorgelegten Dissertation stehen.

Die Arbeit wurde bisher weder im in- noch im Ausland in gleicher oder ähnlicher Form einer anderen Prüfungsbehörde vorgelegt.

Die geltende Promotionsordnung der Physikalisch-Astronomischen Fakultät ist mir bekannt.

Ich versichere ehrenwörtlich, dass ich nach bestem Wissen die reine Wahrheit gesagt und nichts verschwiegen habe.

Jena, 15. April 2021 Yang Ran